Atomic-scale structure of crystalline InP, amorphous InP and crystalline $Ga_{1-x}In_xP$ alloys

Claudia Sarah Schnohr

A thesis submitted for the degree of

Doctor of Philosophy

of

The Australian National University

June 2009

This thesis does not incorporate any material previously submitted for a degree or diploma at any university and to the best of my knowledge does not contain any material published or written by any other person except where due reference is made in the text.

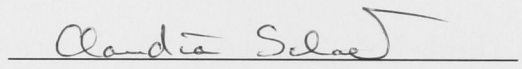

Claudia Sarah Schnohr, June 2009

Acknowledgements

Most of all, I would like to thank Dr. Mark Ridgway, Dr. Patrick Kluth and Dr. Aidan Byrne for their excellent supervision. Their effort to facilitate all experimental work, their guidance and expert advise on technical and scientific matters and the opportunity to present the results of this work at national and international conferences have been invaluable.

I have deeply enjoyed working with Dr. Leandro Araujo, Raquel Giulian, David Sprouster, Zohair Hussain, Bernt Johannessen and David Llewellyn and I am very thankful for their help and support with sample preparation, measurement and analysis.

Further thanks are to the staff from the Department of Electronic Materials Engineering, the Department of Nuclear Physics and the Electronics Unit who look after all the equipment and keep it running year after year. Many experiments would not have taken place without their quick and competent action whenever problems arose and things broke down. Thanks also to the beamline scientists at the Photon Factory, Japan.

Working at the Research School of Physics and Engineering has been great and I am thankful to all people who contributed to my time here.

Additionally, I would like to thank my parents, Dr. med Sabine Schnohr and Ditmar Schnohr, for putting up with the long hours on the plane to visit us in the land down under, for supporting the German and Australian Post by sending lots of packages and for being there even from so far away.

Big thanks also go to my husband, Sven Paufler, for moving half around the world because of me. His interest in this work, his encouragement and his support during all stages of the project are greatly appreciated.

Publications

Candidate's journal publications that have originated during the PhD. Articles directly related to this thesis are highlighted.

EXAFS study of the amorphous phase of InP after swift heavy ion irradiation
C. S. Schnohr, P. Kluth, A. P. Byrne, G. J. Foran, and M. C. Ridgway, Nucl. Instr. Meth. B **257**, 293 (2007).

Ion irradiation effects on metallic nanocrystals
P. Kluth, B. Johannessen, R. Giulian, C. S. Schnohr, G. J. Foran, D. J. Cookson, A. P. Byrne, and M. C. Ridgway, Rad. Eff. Def. Sol. **162**, 501 (2007).

Comparison of the atomic structure of InP amorphized by electronic or nuclear ion energy-loss processes
C. S. Schnohr, P. Kluth, A. P. Byrne, G. J. Foran, and M. C. Ridgway, Phys. Rev. B **77**, 073204 (2008).

Measurement of latent tracks in amorphous SiO_2 using small angle x-ray scattering
P. Kluth, C. S. Schnohr, D. J. Sprouster, A. P. Byrne, D. J. Cookson, and M. C. Ridgway, Nucl. Instr. Meth. B **266**, 2994 (2008).

Atomic-scale structure of $Ga_{1-x}In_xP$ alloys measured with extended x-ray absorption fine structure spectroscopy
C. S. Schnohr, L. L. Araujo, P. Kluth, D. J. Sprouster, G. J. Foran, and M. C. Ridgway, Phys. Rev. B **78**, 115201 (2008).

Size-dependent characterization of embedded Ge nanocrystals: Structural and thermal properties
L. L. Araujo, R. Giulian, D. J. Sprouster, C. S. Schnohr, D. J. Llewellyn, P. Kluth, D. J. Cookson, G. J. Foran, and M. C. Ridgway, Phys. Rev. B **78**, 094112 (2008).

Fine structure in swift heavy ion tracks in amorphous SiO_2
P. Kluth, C. S. Schnohr, O. H. Pakarinen, F. Djurabekova, D. J. Sprouster, R. Giulian, M. C. Ridgway, A. P. Byrne, C. Trautmann, D. J. Cookson, K. Nordlund, and M. Toulemonde, Phys. Rev. Lett. **101**, 175503 (2008).

Rapid ion-implantation-induced amorphisation of $In_xGa_{1-x}As$ relative to InAs and GaAs
Z. S. Hussain, E. Wendler, W. Wesch, G. J. Foran, C. S. Schnohr, D. J. Llewellyn, and M. C. Ridgway, Phys. Rev. B **79**, 085202 (2009).

Changes in metal nanoparticle shape and size induced by swift heavy-ion irradiation
M. C. Ridgway, P. Kluth, R. Giulian, D. J. Sprouster, L. L. Araujo, C. S. Schnohr, D. J. Llewellyn, A. P. Byrne, G. J. Foran, and D. J. Cookson, Nucl. Instr. Meth. B **267**, 931 (2009).

The influence of annealing conditions on the growth and structure of embedded Pt nanocrystals
R. Giulian, L. L. Araujo, P. Kluth, D. J. Sprouster, C. S. Schnohr, B. Johannessen, G. J. Foran, and M. C. Ridgway, J. Appl. Phys. **105**, 044303 (2009).

Energy dependent saturation width of swift heavy ion shaped embedded Au nanoparticles
P. Kluth, R. Giulian, D. J. Sprouster, C. S. Schnohr, A. P. Byrne, D. J. Cookson, and M. C. Ridgway, Appl. Phys. Lett. **94**, 113107 (2009).

Temperature-dependent EXAFS analysis of embedded Pt nanocrystals
R. Giulian, L. L. Araujo, P. Kluth, D. J. Sprouster, C. S. Schnohr, G. J. Foran, and M. C. Ridgway, J. Phys.: Condens. Matter **21**, 155302 (2009).

Structural modification of swift heavy ion irradiated amorphous Ge layers
W. Wesch, C. S. Schnohr, P. Kluth, Z. S. Hussain, L. L. Araujo, R. Giulian, D. J. Sprouster, A. P. Byrne, and M. C. Ridgway, J. Phys. D: Appl. Phys. **42**, 115402 (2009).

Anisotropic vibrations in crystalline and amorphous InP
C. S. Schnohr, P. Kluth, L. L. Araujo, D. J. Sprouster, A. P. Byrne, G. J. Foran, and M. C. Ridgway, Phys. Rev. B **79**, 195203 (2009).

A FCC-to-HCP phase transformation in Co nanoparticles induced by swift heavy ion irradiation
D. J. Sprouster, R. Giulian, C. S. Schnohr, L. L. Araujo, P. Kluth, A. P. Byrne, G. J. Foran, B. Johannessen, and M. C. Ridgway, submitted.

Swift heavy ion induced damage formation in III-V binary and ternary semiconductors
C. S. Schnohr, P. Kluth, R. Giulian, D. J. Llewellyn, A. P. Byrne, and M. C. Ridgway, submitted.

Abstract

III-V binary and ternary semiconductors have numerous electronic and optoelectronic applications such as high frequency transistors, light emitting diodes and lasers, photodetectors, optical amplifiers and high efficiency solar cells. Ion irradiation is a powerful technique for semiconductor modification. A detailed knowledge of the atomic-scale structure is an important part of understanding and tailoring the properties of the material. In this thesis, extended x-ray absorption fine structure (EXAFS) spectroscopy was used to study different structural aspects of III-V semiconductors.

InP, InAs, GaP, GaAs and the related ternary alloys $Ga_{0.50}In_{0.50}P$ and $Ga_{0.47}In_{0.53}As$ were irradiated at room temperature with 185 MeV Au ions. At this ion energy, inelastic collisions with target electrons (electronic stopping) dominate the energy transfer from the ion to the target and elastic collisions with target atoms (nuclear stopping) are negligible. Damage formation was studied using transmission electron microscopy and Rutherford backscattering spectroscopy in channeling configuration. Despite the nearly identical energy loss values, the materials respond very differently. InP and $Ga_{0.50}In_{0.50}P$ are readily amorphized while GaP and GaAs remain almost undamaged. InAs and $Ga_{0.47}In_{0.53}As$ exhibit an intermediate behavior. A material-dependent combination of irradiation induced damage formation and annealing is proposed to describe the strikingly different response of the III-V materials to high electronic excitation.

InP was also amorphized using Se ions with energies ranging from 80 keV to 7 MeV, where the energy transfer is dominated by nuclear stopping. EXAFS was used to determine the structural parameters of the amorphous phase produced in both energy regimes for as-irradiated and thermally relaxed samples. Despite

the fundamentally different energy transfer mechanism, no significant difference in the atomic-scale structure is observed and a common process, namely a quench from the melt, is considered responsible for amorphization in both regimes.

Vibrational properties of crystalline and amorphous InP were studied with EXAFS as a function of measurement temperature, ranging from 20 to 295 K. For crystalline InP, a strong vibrational anisotropy is observed where relative vibrations between first nearest neighbor atoms are much smaller parallel to the bond direction than perpendicular to it. This corresponds to a strong in-phase motion of the atoms along the bond and mostly uncorrelated vibrations perpendicular to it, consistent with the well-known behavior of III-V semiconductors where bond bending is energetically favored over bond stretching. Amorphous InP is characterized by strongly increased structural disorder but very similar thermal disorder when compared to the crystalline phase.

EXAFS was also used to study the interatomic distance distributions of the first three nearest neighbor shells around Ga and In atoms in $Ga_{1-x}In_xP$ alloys. Experimental results agree well with model calculations. The first nearest neighbor shell has a composition-dependent bimodal distance distribution with values much closer to that of the corresponding binaries than those of the virtual crystal approximation. The second nearest neighbor shell still shows different interatomic distances, corresponding to the three different cation-cation pairs, but the values are very close to those expected from the lattice constant. Like in $Ga_{1-x}In_xAs$, lattice mismatch in $Ga_{1-x}In_xP$ is thus accommodated by both bond length and bond angle relaxation though primarily via the latter.

Contents

Chapter 1

Introduction

Extended x-ray absorption fine structure spectroscopy

Extended x-ray absorption fine structure (EXAFS) spectroscopy is a powerful technique for the structural analysis of solids. Over the past decades it has been applied to a large number of systems from biology, chemistry, geology, environmental science and materials science [1, 2]. EXAFS measures the fine structure of the x-ray absorption coefficient at energies above a particular absorption edge and provides structural information about the atomic environment of the absorbing element. In particular, EXAFS is sensitive to coordination number, interatomic distance and structural and thermal disorder. In contrast to x-ray diffraction (XRD), EXAFS is a short-range probe that samples the atomic neighborhood of the absorbing species up to some tens of angstroms [2]. As no long-range order is required, EXAFS can be applied to the study of both crystalline and disordered or amorphous systems. Given the short time scale of the x-ray absorption process, EXAFS measures the average over all instantaneous configurations. It therefore contains information complementary to that obtained with XRD which measures the average configuration of the system. These characteristics of being element-specific and applicable to a wide range of ordered and disordered materials make EXAFS a versatile and powerful tool for structural analysis. Basic principle, theoretical and experimental aspects as well as data analysis are discussed in Chapter 2.

III-V compound semiconductors

In the field of materials science, the interest in III-V binary and ternary semiconductors is driven by their numerous electronic and optoelectronic applications. Many of the III-V compounds display a direct band gap with energies ranging from 0.17 eV for InSb [3, 4] to over 2 eV for some stoichiometries of $Ga_{1-x}In_xP$ [4]. In such ternary alloys, both band gap energy and lattice constant vary with composition between the values of the binary end members. The wide range of direct band gap energies thus available and the possibility to lattice match different III-V materials allow the fabrication of heterojunctions crucial for the design of high performance optoelectronic devices [5]. III-V based laser diodes, modulators and semiconductor amplifiers are key elements of optical fiber communications [5]. High frequency transistors operating above 1 GHz are particularly important for mobile phones [6]. Other major applications include infrared emission and detection, light emitting diodes and high efficiency solar cells [5, 7, 8]. Superior thermal properties also make the III-V materials promising candidates for high-temperature electronic devices operating at several hundred degrees Celsius [9].

Ion irradiation and implantation is a powerful technique for modifying semiconductor properties and has multiple applications in device fabrication. Most importantly, ion implantation is often used for doping the material with impurity atoms thereby changing its electrical properties. The advantage of using ion implantation is that virtually every element can be introduced into the matrix with a high degree of control over the amount of impurities and their depth distribution. Inherent with this process is the formation of crystal damage due to the energy transfer from the ions to the target. Depending on the material and the irradiation conditions, this damage can range from point defects and defect clusters to complete amorphization.

For all applications, a detailed knowledge of the structure of a material, including the presence of damage and disorder, is an important part of understanding and modifying its properties of interest. Rutherford backscattering

spectroscopy (RBS) and transmission electron microscopy (TEM) were used to investigate the damage formation in III-V semiconductors due to highly energetic ion irradiation. The results are presented in Chapter 3. EXAFS was applied to study three different structural aspects of III-V semiconductors:

(i) the atomic-scale structure of InP amorphized by ion irradiation,

(ii) the vibrational anisotropy in crystalline and amorphous InP, and

(iii) the composition-dependent structure of $Ga_{1-x}In_xP$ alloys.

The results are presented in Chapter 4, Chapter 5 and Chapter 6, respectively. The remainder of this introduction will briefly describe the motivation for each of the four topics. More detailed background information is then presented at the beginning of the corresponding chapters.

Swift heavy ion irradiation of III-V semiconductors

Depending on the ion energy, different interaction processes dominate the energy transfer from the projectile to the target. In the keV to low MeV region, the ions deposit their energy predominantly via ballistic collisions with target atoms (nuclear stopping). In contrast, swift heavy ions (SHIs) of a few hundred MeV primarily interact with target electrons (electronic stopping). Amorphization of III-V semiconductors due to nuclear stopping has been extensively studied for several decades [10,11] whereas damage formation due to SHI irradiation is still not fully understood. Under irradiation with 593 MeV Au ions, for example, GaP remains almost undamaged while InP is readily amorphized [12]. Given this strikingly different behavior, the question arises of how $Ga_{1-x}In_xP$ ternary alloys respond to similar irradiation conditions.

The effects of high electronic stopping in semiconductors are of technological and scientific interest. The fabrication of three-dimensional device structures using ion irradiation requires deep implants with increased ion energies thus inevitably increasing the electronic stopping contribution. Furthermore, the amount of defects created by the impact of highly energetic particles is important for the stability of electronic devices intended for space applications. From

a scientific point of view, the interactions following the passage of SHIs through matter are still under debate with several different models proposed [13–15]. Further systematic studies are therefore necessary to better understand the physical processes operative in III-V semiconductors under SHI irradiation.

Structure of InP amorphized by ion irradiation

Amorphous semiconductors have a number of technological applications, for example in flat-panel displays and sensors. The structure of amorphous materials is characterized by significantly increased structural disorder compared to the crystalline phase. Furthermore, amorphous compound semiconductors may contain chemical disorder in the form of homopolar bonds that do not exist in crystalline material [16, 17]. Such "wrong" bonds are particularly interesting given they introduce donor and acceptor states within the band gap and thus influence the electronic properties of the material [18]. Different preparation techniques can yield different amorphous phase structures and, consequently, materials that might have different properties. As mentioned above, the energy loss of the projectile can be dominated by either nuclear or electronic stopping depending on the ion energy. Elastic collisions with target atoms (nuclear stopping) result in atomic displacements if sufficient energy is transferred. Inelastic collisions with target electrons (electronic stopping) lead to excitation and ionization of the electronic system. Given these fundamentally different energy transfer mechanisms, the question arises of whether the resulting amorphous phase structures are different. EXAFS has been applied successfully to the study of amorphous compound semiconductors demonstrating the capability to detect subtle differences that characterize different amorphous phase structures [16, 17, 19–22]. This technique is therefore well suited for the comparison of the atomic-scale structure of InP amorphized by ion irradiation with dominant electronic or nuclear energy loss, thus providing information about the amorphization mechanism operative in both regimes.

Vibrational anisotropy in crystalline and amorphous InP

The temperature dependence of atomic motion in a solid contains information about vibrational and thermal properties such as Einstein or Debye temperatures. In contrast to XRD, EXAFS is sensitive to the correlated motion of neighboring atoms and thus yields valuable insight into the phase relation of these vibrations. By comparing XRD and EXAFS measurements one can distinguish between vibrations parallel or perpendicular to the bond direction. Such knowledge provides an experimental test for phonon eigenvectors obtained from dynamical models or *ab initio* calculations [23, 24]. For Cu, relative vibrations between neighboring atoms are isotropic and the first four nearest neighbor (NN) shells are characterized by a very similar thermal behavior [23]. In contrast, relative vibrations between first NN atoms in Ge, CdSe and AgI are much more pronounced perpendicular to the bond direction than parallel to it [24–26]. Furthermore, relative vibrations parallel to the line connecting the absorber-backscatterer pair in Ge, GaAs and AgI are more pronounced for higher NN shells than for the first NN shell, in contrast to observations for Cu [23, 27–29]. InP is a scientifically interesting material for the study of thermal and vibrational properties. While it has the same crystal structure as GaAs, the two atomic constituents differ considerably relative to the materials mentioned above: Indium has almost four times the mass of Phosphorus and approximately one and a half times the radius. Studying thermal vibrations in InP thus complements the existing literature and can contribute to a better understanding of the mechanisms that lead to the vibrational anisotropy.

Composition-dependent structure of $Ga_{1-x}In_xP$ alloys

As mentioned above, the interest in the ternary alloys $A_{1-x}B_xC$ stems from the fact that many material properties such as band gap energy and lattice constant can be tuned between the values of the corresponding binaries by adjusting the ternary composition. The dilute limit is also of interest since many device applications rely on the properties of impurity atoms. Given that mate-

rial characteristics are often directly dependent on the atomic-scale structure, one important question is how the two different binary lattice constants are accommodated in the ternary alloy. Both bond length and bond angle relaxation have been proposed. Experimentally, a combination of the two is usually observed. Extensive calculations for $Ga_{1-x}In_xP$ alloys predict the interatomic distance distributions of the first and second NN shells as well as the bond angle distributions [30]. Experimentally, similarities to other III-V compounds have been observed for the first NN shell [31], however, there are no experimental data available on the higher shells despite the technological importance of $Ga_{1-x}In_xP$ alloys. The direct band gap with its high energy makes this system an important component of high efficiency multijunction solar cells [7,8]. As demonstrated as early as 1983 for $Ga_{1-x}In_xAs$ alloys, EXAFS is well suited to study the interatomic distances of different atomic pairs given the element-specific nature of the method [32]. A detailed investigation of the distance distributions of the first three NN shells around Ga and In atoms in $Ga_{1-x}In_xP$ enables the comparison with a number of structural models and the evaluation of bond length and bond angle relaxation. Such knowledge will be beneficial to a more comprehensive understanding of this technologically important ternary material.

CHAPTER 2

Extended x-ray absorption fine structure spectroscopy

2.1 Basic principle

X-ray absorption fine structure (XAFS) spectroscopy measures the energy-dependent fine structure of the x-ray absorption coefficient near the absorption edge of a particular element. A detailed discussion of both theoretical and experimental aspects of XAFS is given in [1].

2.1.1 X-ray absorption

If x-rays of intensity I_0 are incident on a sample, as shown schematically in Fig. 2.1, the extent of absorption depends on the photon energy E and sample thickness t. According to Beer's Law, the transmitted intensity I_t is

$$I_\mathrm{t}(t) = I_0 \mathrm{e}^{-\mu(E)t} \tag{2.1}$$

where $\mu(E)$ is the energy-dependent x-ray absorption coefficient [2, 33]. Over large energy regions $\mu(E)$ is a smooth function of the photon energy, varying approximately as $\mu(E) \sim \rho Z^4/mE^3$ [33]. Here ρ denotes the target density while Z and m are the atomic number and mass, respectively. Thus, $\mu(E)$ decreases with increasing photon energy. If the latter equals or exceeds the binding energy of a core electron, however, a new absorption channel is available in which the photon is annihilated thereby creating a free photoelectron and a core-hole. This

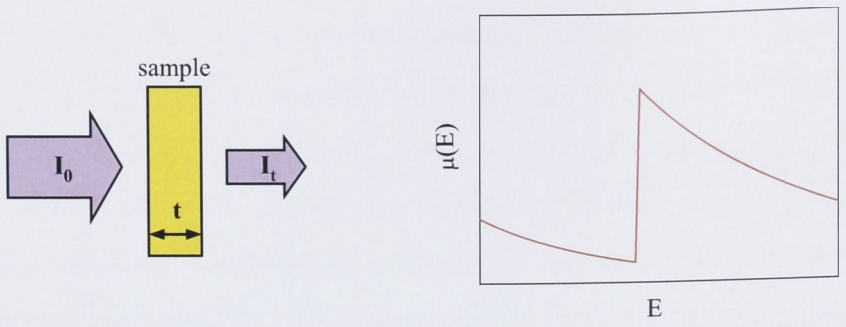

Figure 2.1: Schematic of incident and transmitted x-ray beam and absorption coefficient $\mu(E)$ versus photon energy E around an absorption edge.

leads to a sharp increase in absorption coefficient as shown in Fig. 2.1. Above the absorption edge, the difference between the photon energy and the binding energy is converted into kinetic energy of the photoelectron and $\mu(E)$ continues to decrease with increasing photon energy.

2.1.2 Absorption fine structure

The photoelectron wave created in the absorption process propagates outwards and is scattered at neighboring atoms [1, 2, 34]. The situation is shown schematically in Fig. 2.2. The outgoing and scattered waves interfere in a manner that depends on the geometry of the absorber environment and on the photo-

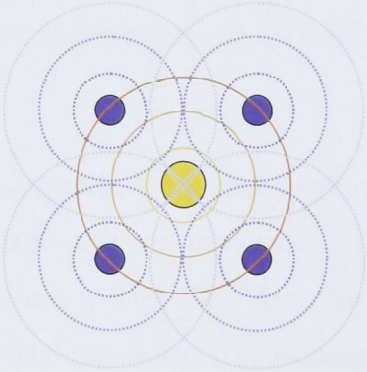

Figure 2.2: Schematic showing the absorbing atom (yellow) and its first NNs (blue). An interference pattern is created by the outgoing (solid orange lines) and reflected (dashed blue lines) photoelectron waves.

electron wavelength. The latter is inversely proportional to the photoelectron momentum and therefore changes with photon energy. $\mu(E)$ is proportional to the magnitude of the wave function of the final state at the site of the absorber atom. Constructive or destructive interference of outgoing and scattered waves thus increases or decreases the absorption probability, creating an energy-dependent fine structure of the absorption coefficient.

Figure 2.3 schematically shows the $\mu(E)$ fine structure as a function of photon energy. Two regions are commonly distinguished, the x-ray absorption near edge structure (XANES) and the extended x-ray absorption fine structure (EXAFS) [1, 33, 34]. The different absorption processes leading to XANES and EXAFS are also shown schematically in Fig. 2.3.

XANES

In the region very close to the absorption edge, the core electron is promoted to unoccupied bound states. XANES is therefore sensitive to the chemical bonding, exhibiting for example characteristic features for different oxidation states of the absorbing atom. XANES also depends on the geometry of the crystal structure thus providing a means of distinguishing between different crystal phases. Theoretical calculations of the fine structure in this region are complex and the accuracy of such simulations is still limited. Therefore, analysis typically compares the measured spectra to those of known standards and quantifies the ratios by which these standards are present in the sample using linear combination fitting.

EXAFS

For photon energies higher than $\sim 30\,\mathrm{eV}$ above the edge [34], the photoelectron receives sufficient kinetic energy to be in a truly free or continuum state. EXAFS is thus independent of chemical bonding and depends on the atomic arrangement around the absorber as discussed above. It contains information about the coordination number, interatomic distances and structural and

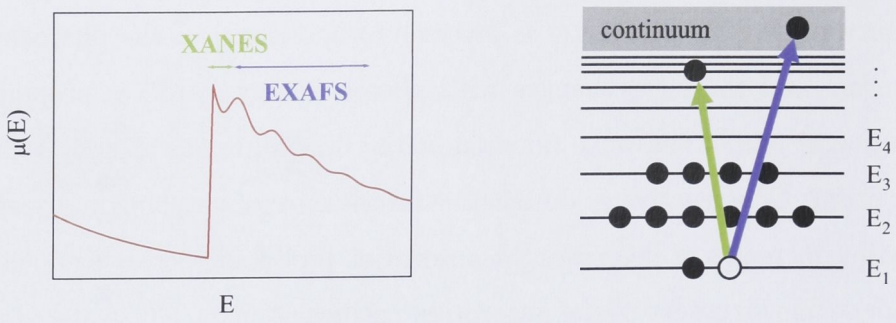

Figure 2.3: Absorption coefficient $\mu(E)$ versus photon energy E including the fine structure above the edge and schematic of the absorption processes leading to XANES and EXAFS.

thermal disorder around a particular atomic species. EXAFS does not require long-range order and is applicable to a wide range of ordered and disordered materials therefore providing a powerful tool for structural analysis. Theoretical calculations of the fine structure in the EXAFS region have improved enormously during the last two decades and simulations with sufficient accuracy are now available. Nevertheless, the measurement of suitable standards still constitutes an important part of the experimental procedure.

In this work, only the EXAFS region of the measured spectra was studied to gain structural information about the systems under investigation. Sections 2.2 and 2.4 therefore focus on the theory of EXAFS and the procedure used for EXAFS analysis, respectively [1, 2, 33].

2.2 EXAFS theory

2.2.1 The EXAFS equation

The fine structure contribution to the absorption coefficient is defined as $\chi(E) = (\mu(E) - \mu_0(E))/\Delta\mu_0$ where $\mu_0(E)$ denotes the smooth absorption background that would be observed in the absence of interference from waves scattered at neighboring atoms [2]. $\Delta\mu_0$ is a normalization factor which, in practice,

is often approximated by the height of the absorption edge. Instead of using $\chi(E)$, the fine structure is usually expressed as a function of the photoelectron wave number k, with $k = \sqrt{2m_e(E - E_0)/\hbar^2}$. Here, m_e stands for the electron mass, E_0 denotes the edge energy and $\hbar$ is Planck's constant divided by 2π. The relation between $\chi(k)$ and the structural parameters of the absorber environment is given by the standard EXAFS equation

$$\chi(k) = \sum_j S_0^2 N_j \frac{|f_j(k)|}{kR_j^2} e^{-2R_j/\lambda(k)} e^{-2\sigma_j^2 k^2} \sin\left[2kR_j + 2\delta_c(k) + \delta_j(k)\right]. \qquad (2.2)$$

The structural parameters are given by N_j, R_j and σ_j^2 denoting the coordination number, distance and standard deviation of all NN atoms of the same type in a particular coordination shell. $f_j(k) = |f_j(k)|e^{i\delta_j(k)}$ represents the complex scattering amplitude while $\delta_c(k)$ stands for the phase shift experienced by the photoelectron wave in the potential of the absorbing atom. $\lambda(k)$ and S_0^2 denote the energy-dependent mean free path of the electron and the amplitude reduction factor, respectively.

Except for the factor S_0^2, Eq. (2.2) was first derived by Sayers *et al.* using the plane-wave approximation [35]. It assumes that the distance between absorber-backscatter pair is sufficiently large to treat the outgoing spherical wave as a plane wave once it reaches the backscattering atom. For accurate calculations of the EXAFS, curved-wave effects have to be taken into account [2]. Nevertheless, Eq. (2.2) contains all the key elements needed to correctly describe the EXAFS phenomenon for systems in which the distance distribution of the atoms in a given coordination shell can be approximated by a Gaussian function. In this case, Eq. (2.2) provides a convenient parametrization of the absorber environment in terms of coordination numbers, distances and standard deviations. Therefore, $\chi(k)$ is still expressed by Eq. (2.2) while the improvements of modern theory have provided successive refinements of the various terms. The key elements in Eq. (2.2) are [2]:

(i) As described above, the interference pattern depends on electron energy and backscatter distance, both accounted for by the $\sin[2kR_j]$ term.

(ii) The strength of the scattering and thus the magnitude of the EXAFS depends on the number and type of scattering atoms, represented by coordination number N_j and scattering amplitude $|f_j(k)|$, respectively.

(iii) The potential of the absorbing or scattering atom leads to a phase shift of the electron wave represented by δ_c and δ_j, respectively. The absorber potential acts twice on the electron wave, once on the way out and once on the way back. The resulting term $2\delta_c(k) + \delta_j(k)$ appears in the sine function of Eq. (2.2).

(iv) The atoms in a particular coordination shell do not have exactly the same distance from the absorber. Differences are caused either by thermal vibrations (*thermal disorder*) or by structural variations in the interatomic distances (*static disorder*) and smear out the oscillations with k. The phase difference in scattered waves due to a given difference in R_j increases with increasing k. This yields increased damping of the EXAFS at high wave numbers. In systems where the distance distributions exhibit only small asymmetry, Gaussian distributions with standard deviations σ_j^2 can be assumed. The term $e^{-2\sigma_j^2 k^2}$ in Eq. (2.2) then accounts for the k-dependent damping of the EXAFS oscillations. In analogy to XRD, σ_j^2 is called the EXAFS Debye-Waller factor.

(v) The range that is probed by EXAFS is usually of the order of tens of angstroms and is limited by the finite lifetime of the final state. The decay is due to inelastic interactions of the photoelectron with the surrounding material such as inelastic scattering and electron or plasmon excitation (*extrinsic losses*) and due to filling of the core-hole with an electron from a higher shell thereby emitting a fluorescence x-ray or an Auger electron (*intrinsic losses*). The mean free path $\lambda(k)$ comprises both extrinsic and intrinsic losses and the term $e^{-2R_j/\lambda(k)}$ accounts for the increasing decay of the wave with increasing distance R_j.

(vi) Relaxation of the system in response to the creation of the core-hole is accounted for by the amplitude reduction factor S_0^2.

A major improvement in modern EXAFS theory is the inclusion of curved-wave effects by keeping the EXAFS equation, Eq. (2.2), but replacing the plane-wave scattering amplitude $f(k)$ by a curved-wave effective scattering amplitude $f_{\text{eff}}(k, R)$. The computer code FEFF [36] calculates not only effective scattering amplitudes for a given absorber environment but also the other k-dependent parameters ($\delta_c(k)$, $\delta_j(k)$ and $\lambda(k)$) thus enabling a refinement of the structural parameters by comparing theoretical and experimental spectra (see Section 2.4.2). Another major improvement is the inclusion of multiple scattering (MS) contributions. These take into account the effects of scattering of the photoelectron at more than one atom which can become significant for certain geometries [2]. Such MS effects have long evaded accurate treatment but can now be included in the calculation of EXAFS by using Eq. (2.2) and appropriate MS amplitudes and phase shifts, calculated for example with the FEFF code [36].

A simple derivation of Eq. (2.2) can be found in [1]. Aspects of the modern EXAFS theory including curved-wave effects and MS are discussed in [2].

2.2.2 Fourier transformation

Fourier transformation (FT) of the EXAFS provides a means to visualize different scattering contributions and is often used during analysis. The benefit of such a procedure was first shown by Sayers *et al.* [35]. Here, a brief example is given to illustrate the effect of Fourier transforming EXAFS spectra. Applying a k-weight of n, a single term of the sum in Eq. (2.2) becomes

$$k^n \chi_j(k) = S_0^2 N_j \frac{|f_j(k)|}{R_j^2} k^{n-1} \mathrm{e}^{-2R_j/\lambda(k)} \mathrm{e}^{-2\sigma_j^2 k^2} \sin\left[2kR_j + \delta_j'(k)\right] \tag{2.3}$$

with $\delta_j'(k) = 2\delta_c(k) + \delta_j(k)$. Assuming that $n = 1$, that $\lambda(k) = \lambda$ and $|f_j(k)| = f_j$ are independent of k and that $\delta_j'(k) = \delta_j^{(0)} + k\delta_j^{(1)}$ is a linear function of k, Eq. (2.3) can be written as

$$\begin{aligned} k\chi_j(k) &= \frac{S_0^2 N_j f_j}{R_j^2} \mathrm{e}^{-2R_j/\lambda} \mathrm{e}^{-2\sigma_j^2 k^2} \sin\left[2kR_j + \delta_j^{(0)} + k\delta_j^{(1)}\right] \\ &= \mathrm{Re}\left[ik\tilde{\chi}_j(k)\right] \end{aligned} \tag{2.4}$$

with

$$k\tilde{\chi}_j(k) = A_j \mathrm{e}^{-2\sigma_j^2 k^2} \mathrm{e}^{-i[2kR_j + \delta_j^{(0)} + k\delta_j^{(1)}]}, \qquad A_j = \frac{S_0^2 N_j f_j}{R_j^2} \mathrm{e}^{-2R_j/\lambda}. \tag{2.5}$$

Performing a FT of $k\tilde{\chi}_j(k)$ gives

$$\begin{aligned} \mathrm{FT} &= \sqrt{\frac{2}{\pi}} \int_0^\infty k\tilde{\chi}_j(k) \mathrm{e}^{2ikR} \mathrm{d}k \\ &= \sqrt{\frac{2}{\pi}} A_j \mathrm{e}^{-i\delta_j^{(0)}} \int_0^\infty \mathrm{e}^{-2\sigma_j^2 k^2 + 2ik(R - R_j - \delta_j^{(1)}/2)} \mathrm{d}k \\ &= \sqrt{\frac{2}{\pi}} A_j \mathrm{e}^{-i\delta_j^{(0)}} \mathrm{e}^{\frac{(R - R_j - \delta_j^{(1)}/2)^2}{2\sigma_j^2}} \int_0^\infty \mathrm{e}^{-2\sigma_j^2 k'^2} \mathrm{d}k' \\ &= \frac{A_j}{2\sigma_j} \mathrm{e}^{-i\delta_j^{(0)}} \mathrm{e}^{\frac{(R - R_j - \delta_j^{(1)}/2)^2}{2\sigma_j^2}}. \end{aligned} \tag{2.6}$$

The magnitude of this FT is a Gaussian function centered at $R_j + \delta_j^{(1)}/2$

$$|\mathrm{FT}| = \frac{S_0^2 N_j f_j}{2\sigma_j R_j^2} \mathrm{e}^{-2R_j/\lambda} \mathrm{e}^{\frac{(R - R_j - \delta_j^{(1)}/2)^2}{2\sigma_j^2}}. \tag{2.7}$$

Different scattering contributions with a large difference in R_j and small values for σ_j^2 thus produce well separated peaks with amplitudes proportional to N_j/σ_j when Fourier transformed. In reality $\lambda(k)$, $|f_j(k)|$ and $\delta_j'(k)$ are complicated functions of k and the FT of the EXAFS cannot be expressed in a simple analytical form [1]. Furthermore, different k-weights such as $n = 2$ or $n = 3$ might be used and a window function is usually applied to account for the finite data range. Modern EXAFS analysis therefore often assumes a model structure and refines the parameters by minimizing the difference between measured and calculated spectra. Usually, this fitting is performed in R-space after experimental and theoretical $\chi(k)$ have been Fourier transformed using suitable numerical procedures (see Section 2.4). EXAFS results are typically presented as the magnitude of the FT due to the illustrative character of such a plot.

2.2.3 Cumulant expansion

The description of the EXAFS presented so far has assumed a Gaussian distance distribution with a mean value R_j and a standard deviation σ_j^2. For

systems with significant asymmetry a Gaussian function may no longer be an adequate approximation for the distance distribution and higher moments must be considered. EXAFS analysis based on a cumulant expansion was first proposed by Bunker in 1983 [37]. An arbitrary distance distribution, given by a function $\rho(R)$ with $\int_0^\infty \rho(R)\mathrm{d}R = 1$, can be characterized defining either *raw moments* p_n or *central moments* P_n

$$p_n = \langle R^n \rangle = \int_0^\infty R^n \rho(R)\mathrm{d}R \tag{2.8}$$

$$P_n = \langle (R - p_1)^n \rangle = \int_0^\infty (R - p_1)^n \rho(R)\mathrm{d}R. \tag{2.9}$$

For any given function, $P_1 = 0$ and, for normalized functions, $p_0 = P_0 = 1$.

For a single atom at distance R, Eq. (2.2) becomes

$$\chi(k) = S_0^2 \frac{|f(k)|}{kR^2} \mathrm{e}^{-2R/\lambda(k)} \sin\left[2kR + \delta'(k)\right] \tag{2.10}$$

where $\delta'(k) = 2\delta_\mathrm{c}(k) + \delta_j(k)$ and the indices j were omitted for clarity. Scattering from a coordination shell with a distance distribution $\rho(R)$ thus yields

$$\begin{aligned} \chi(k) &= S_0^2 N \frac{|f(k)|}{k} \int_0^\infty \frac{\mathrm{e}^{-2R/\lambda(k)}}{R^2} \sin\left[2kR + \delta'(k)\right] \rho(R)\mathrm{d}R \\ &= \mathrm{Re}\left[\frac{1}{i} S_0^2 N \frac{|f(k)|}{k} \mathrm{e}^{i\delta'(k)} \int_0^\infty \frac{\mathrm{e}^{-2R/\lambda(k)}}{R^2} \mathrm{e}^{2ikR} \rho(R)\mathrm{d}R\right]. \end{aligned} \tag{2.11}$$

Assuming a narrow distribution, the integral can be approximated by

$$\int_0^\infty \frac{\mathrm{e}^{-2R/\lambda(k)}}{R^2} \mathrm{e}^{2ikR} \rho(R)\mathrm{d}R \sim \frac{\mathrm{e}^{-2p_1/\lambda(k)}}{p_1^2} \int_0^\infty \mathrm{e}^{2ikR} \rho(R)\mathrm{d}R. \tag{2.12}$$

The integral $\int_0^\infty \mathrm{e}^{2ikR} \rho(R)\mathrm{d}R$ corresponds to a FT of the distance distribution and is called the *characteristic function*. It can be expressed in terms of the raw moments by

$$\int_0^\infty \mathrm{e}^{2ikR} \rho(R)\mathrm{d}R = \sum_{n=0}^\infty \frac{(2ik)^n}{n!} p_n. \tag{2.13}$$

Unfortunately, this series is slow to converge [1, 37]. In contrast, the cumulant expansion

$$\int_0^\infty \mathrm{e}^{2ikR} \rho(R)\mathrm{d}R = \exp\left[\sum_{n=0}^\infty \frac{(2ik)^n}{n!} C_n\right] \tag{2.14}$$

with C_n being the n-th cumulant of $\rho(R)$ converges much more rapidly [37]. Typically, the first two, three or four C_n are considered. The cumulants are connected to the moments by [37]

$$\begin{aligned}
C_0 &= \ln p_0 = \ln P_0 = 0 \\
C_1 &= p_1 = \langle R \rangle \equiv R_{\mathrm{EXAFS}} \\
C_2 &= p_2 - p_1^2 = P_2 = \left\langle (R - R_{\mathrm{EXAFS}})^2 \right\rangle \equiv \sigma^2_{\mathrm{EXAFS}} \\
C_3 &= p_3 - 3p_2p_1 + 2p_1^3 = P_3 = \left\langle (R - R_{\mathrm{EXAFS}})^3 \right\rangle \\
C_4 &= p_4 - 4p_3p_1 - 3p_2^2 + 12p_2p_1^2 - 6p_1^4 = P_4 - 3P_2^2 \\
&= \left\langle (R - R_{\mathrm{EXAFS}})^4 \right\rangle - 3(\sigma^2_{\mathrm{EXAFS}})^2.
\end{aligned} \tag{2.15}$$

Developing the sum in Eq. (2.14) gives

$$\begin{aligned}
\exp\left[\sum_{n=0}^{\infty} \frac{(2ik)^n}{n!} C_n\right] = \exp\Big[&C_0 + 2ikC_1 - 2k^2C_2 - \frac{4}{3}ik^3C_3 \\
&+ \frac{2}{3}k^4C_4 + \ldots\Big].
\end{aligned} \tag{2.16}$$

Inserting Eqs (2.12), (2.14) and (2.16) into Eq. (2.11) thus yields

$$\begin{aligned}
\chi(k) &= \mathrm{Re}\left[\frac{1}{i} S_0^2 N \frac{|f(k)|}{k} \mathrm{e}^{i\delta'(k)} \frac{\mathrm{e}^{-2p_1/\lambda(k)}}{p_1^2} \mathrm{e}^{(C_0 - 2k^2C_2 + \frac{2}{3}k^4C_4 + \ldots)} \right. \\
&\qquad \left. \times \mathrm{e}^{i(2kC_1 - \frac{4}{3}k^3C_3 + \ldots)}\right] \\
&= S_0^2 N \frac{|f(k)|}{k} \frac{\mathrm{e}^{-2p_1/\lambda(k)}}{p_1^2} \mathrm{e}^{(C_0 - 2k^2C_2 + \frac{2}{3}k^4C_4 + \ldots)} \\
&\qquad \times \sin\left[2kC_1 - \frac{4}{3}k^3C_3 + \ldots + \delta'(k)\right].
\end{aligned} \tag{2.17}$$

Neglecting cumulants higher than the fourth and using the terminology defined in Eq. (2.15), the cumulant expansion of the EXAFS can be written as

$$\begin{aligned}
\chi(k) = S_0^2 N \frac{|f(k)|}{k} &\frac{\mathrm{e}^{-2R_{\mathrm{EXAFS}}/\lambda(k)}}{R^2_{\mathrm{EXAFS}}} \mathrm{e}^{(-2k^2\sigma^2_{\mathrm{EXAFS}} + \frac{2}{3}k^4C_4)} \\
&\times \sin\left[2kR_{\mathrm{EXAFS}} - \frac{4}{3}k^3C_3 + \delta'(k)\right].
\end{aligned} \tag{2.18}$$

This expression now allows the EXAFS to be analyzed in terms of the cumulants of the interatomic distance distribution: the first cumulant R_{EXAFS} corresponding to the mean value, the second cumulant or Debye-Waller factor $\sigma^2_{\mathrm{EXAFS}}$ representing the standard deviation and the third and fourth cumulants, C_3 and C_4, denoting asymmetric and symmetric deviations from a Gaussian profile, respectively. For very small or Gaussian disorder, only the first two cumulants have to be considered and Eq. (2.18) corresponds to Eq. (2.2) with $R_j = R_{\mathrm{EXAFS}}$ and $\sigma_j^2 = \sigma^2_{\mathrm{EXAFS}}$.

EXAFS samples the one-dimensional distance distribution $\rho(R)$ that is connected to the three-dimensional distribution $\rho(\mathbf{R})$ by $\rho(R) = \int \rho(\mathbf{R}) R^2 \mathrm{d}\Omega$ where the integral over $\mathrm{d}\Omega$ corresponds to an angular average. Therefore, care has to be taken when comparing the cumulants of $\rho(R)$ with the three-dimensional motion of the atoms or with structural parameters determined by other techniques such as XRD. Relations between these different properties are derived and discussed in detail in Section 5.1.1.

2.3 Experimental aspects

2.3.1 Synchrotron radiation

Most XAFS experiments are performed at synchrotron sources due to the need of high x-ray intensities and a continuous energy spectrum. Figure 2.4 shows the basic design of a modern synchrotron. The electrons are first accelerated in a linear accelerator before their energy is further increased in the booster ring. From here they are transferred to the storage ring where they circulate over a million times each second, creating intensive electro-magnetic radiation. Beamlines "process" and deliver the radiation to a number of end stations where it can be used for a variety of experimental techniques.

When a charged particle traverses a magnetic field it is forced to change the direction of its motion thereby emitting electro-magnetic radiation. In a synchrotron, the electrons are forced around the storage ring by a series of bending

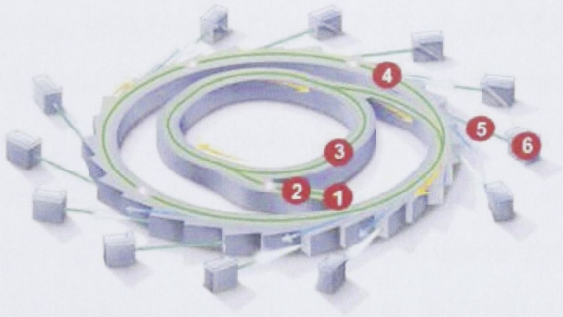

(1) Electron source
(2) Linear accelerator
(3) Booster ring
(4) Storage ring
(5) Beamline
(6) Experiment

Figure 2.4: Design of a modern synchrotron facility (taken from [38]).

magnets. The radiation thus created is characterized by a continuous energy spectrum over a wide range of wavelengths (from infrared to hard x-rays), high intensity, strong polarization and a pulsed nature. Modern synchrotron facilities also have additional elements, so-called insertion devices, placed at the straight section between the bending magnets. These devices constitute a series of alternating magnetic fields that force the electron beam to perform either strong (Wiggler) or gentle (Undulator) oscillations. The Wiggler emits a broad beam of incoherent radiation characterized by increased intensity and a continuous energy spectrum extending to much higher x-ray energies compared to a bending magnet. The Undulator emits a narrow beam of coherent radiation the intensity of which is amplified up to 10,000 times but only at certain frequencies. Based on these characteristics, the device best suited for a particular experimental technique can be chosen. Schematics for the three devices are shown in Fig. 2.5.

Each beamline is tailored to meet the requirements of a particular experimental technique. Figure 2.6 depicts the various components of a typical modern

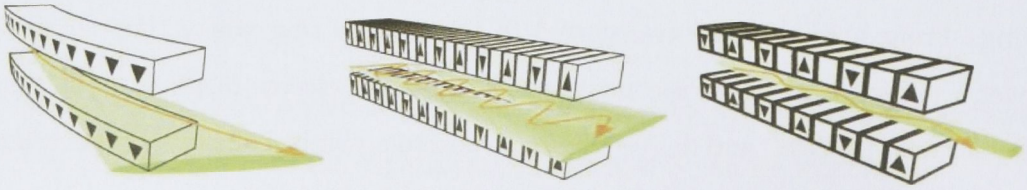

(a) Bending magnet (b) Wiggler (c) Undulator

Figure 2.5: Three different devices where the electron beam is forced to change direction in a magnet field thereby emitting synchrotron radiation (taken from [38]).

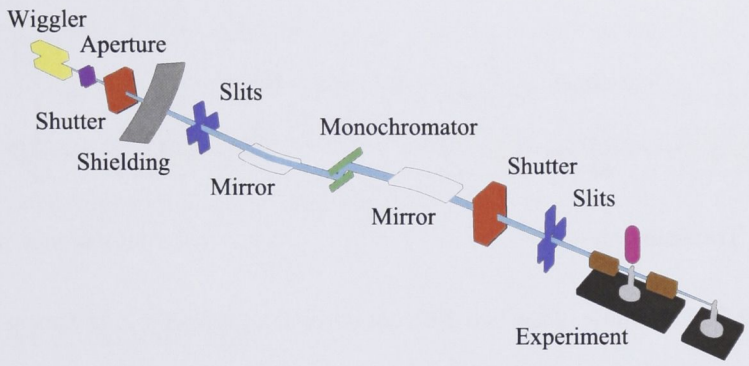

Figure 2.6: Typical components of a modern XAFS beamline (taken from [39]).

XAFS beamline. Mirrors are used to collimate and focus the beam while apertures and adjustable slits define its size. A double crystal monochromator is used to isolate x-rays of a very narrow energy band using the criterion for Bragg diffraction, $n\lambda = 2d \sin\theta$. Here, n is an integer, λ denotes the x-ray wavelength, d stands for the lattice spacing of the diffracting crystal and θ represents the angle under which the beam is incident on the crystal. Energies that satisfy the Bragg condition with $n \geq 2$ are called "harmonics" and have to be removed from the beam. This can be achieved by either slightly detuning the monochromator (which decreases the transmission of harmonics significantly more than that of the primary energy) or by using a special x-ray mirror that only reflects energies below a critical value. With such an experimental arrangement, the absorption coefficient can be measured as a function of x-ray energy.

2.3.2 Detection modes

In general, there are two possibilities to measure the absorption coefficient, *transmission mode* and *fluorescence mode*. The experimental setup for both cases is shown schematically in Fig. 2.7 [1, 33].

Transmission mode

In transmission mode both the incoming and the transmitted beam (I_0 and I_t, respectively) are measured by ion chambers and the absorption coefficient can be obtained according to Eq. (2.1). Detecting voltage or current pulses gen-

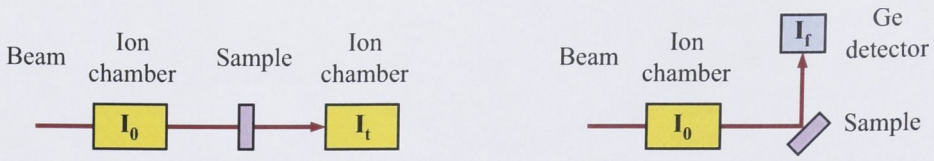

(a) Transmission mode (b) Fluorescence mode

Figure 2.7: Schematic of the two different detection modes for XAFS measurements.

erated in the ion chamber counting chain is inherently simpler than detecting single photons with a solid state detector often used for fluorescence measurements (see below). Using the same type of detector for I_0 and I_t also has the advantage of having a common energy dependence. However, transmission measurements require concentrated samples such that the difference between I_0 and I_t is significantly larger than the variation due to counting statistics. Furthermore, samples must be highly homogeneous, of constant thickness and free of pinholes. One means to prepare a sample that satisfies these requirements is to crush up a suitable amount of material and mix it with boron nitride. Once a fine, homogeneous powder is obtained, it is compacted into the small hole of a sample holder and sealed on both sides with Kapton tape to achieve uniform thickness. All samples in this work have been measured in transmission mode.

Fluorescence mode

Instead of measuring the intensity of the transmitted beam one can also detect the characteristic x-rays that are emitted when the core-hole is filled with an electron from a higher energy level. The intensity of this fluorescence line is proportional to the absorption caused by the element under investigation, however, the relation is more complicated than for transmission measurements and the possible absorption of the fluorescent x-ray while exiting the sample must be taken into account. Detecting the fluorescence signal is also more complicated since it must be isolated from other x-rays, most prominently the elastically scattered beam itself. Usually a multiple-element solid-state Ge detector is chosen.

The big advantage of this method is the ability to measure highly dilute and non-homogeneous samples. Instead of detecting the fluorescent x-rays, one can also measure the electrons emitted from the sample such as the photoelectrons themselves, secondary electrons and Auger electrons.

2.4 Data analysis

2.4.1 Processing

The first stage of the data reduction is to isolate the fine structure from the absorption background, that is to obtain $\chi(E) = (\mu(E) - \mu_0(E))/\Delta\mu_0$. To this end, the region below the edge is first fitted to a smooth pre-edge function which accounts for absorption from other edges and instrumental background. This pre-edge function is then extrapolated to the whole energy range and subtracted from the data. The next step is to approximate the absorption background $\mu_0(E)$ (absorption that would be observed in the absence of interference from waves scattered at neighboring atoms) by a spline function that approaches a smooth post-edge function at high energies. In the third step the data are normalized with respect to the height of the absorption edge to remove effects of sample thickness and concentration. Different samples thus become directly comparable. Figure 2.8 (a) shows the raw $\mu(E)$ data obtained for c-InP (see Chapter 4 for details) together with the pre-edge, post-edge and background contributions.

To obtain $\chi(k)$ the energy scale is converted to a k-scale where the photoelectron wave number is defined as $k = \sqrt{2m_e(E - E_0)/\hbar^2}$. Experimentally, the threshold energy E_0 is typically taken as the maximum of the derivative of $\mu(E)$ with respect to E. Nevertheless, this choice is somewhat arbitrary and may not correspond to the theoretically calculated E_0 value (see Section 2.4.2). Figure 2.8 (b) plots $\chi(k)$ isolated from the data shown in panel (a) and weighted with k^3 to emphasize the data at higher k. Depending on the sample and the absorber-backscatterer pair under study, different k-weights might be chosen.

The next step is to Fourier transform the data into R-space. Usually a

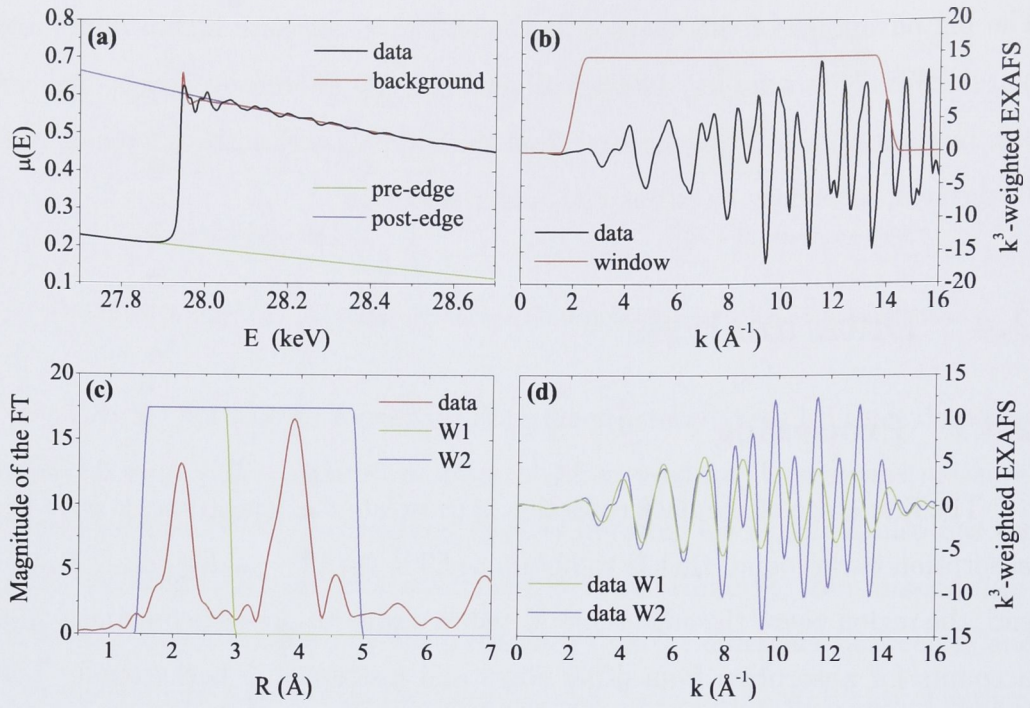

Figure 2.8: Different stages of EXAFS data processing. (a) Raw $\mu(E)$ data together with the fitted pre-edge and post-edge functions and the absorption background $\mu_0(E)$. (b) $\chi(k)$ obtained after background removal and conversion from energy scale to photoelectron wave number k-scale. (c) Magnitude of the FT obtained from $\chi(k)$ using the smooth Hanning window plotted in panel (b). (d) Back-transformed data for two different FT windows (see panel (c)) selecting different scattering contributions.

smooth window function is applied to minimize truncation effects. Figure 2.8 (b) shows the "Hanning" window used in this work and Fig. 2.8 (c) plots the magnitude of the resulting FT. While this is the most common way to display data in R-space, it should be noted that the FT is a complex function and both magnitude and phase (or alternatively, real and imaginary part) have to be considered for the full information content.

A back-transformation can be used to isolate different scattering contributions if their signals are well separated in R-space. This methodology has been extensively used for the analysis of first NN scattering, however, it usually fails for higher NN shells due to the overlap of different scattering contributions. Figure 2.8 (c) shows two different Hanning windows selecting only the first shell

peak (W1) or first and higher shell contributions (W2). The resulting back-transformed k-spectra are plotted in Fig. 2.8 (d).

In this work, data processing was performed with the IFEFFIT code [40] and the corresponding user interface ATHENA [41].

2.4.2 Fitting

A number of different methods have been applied to obtain structural parameters from measured EXAFS spectra. In this work, the data have been analyzed using the IFEFFIT code [40] and the corresponding user interface ARTEMIS [41]. This methodology is a model-dependent approach based on the cumulant expansion (see Section 2.2.3) and requires some pre-existing knowledge about the system under investigation, a requirement satisfied for all systems studied herein.

The analysis starts with a model structure that specifies the absorbing atom and the position and type of the surrounding atoms that are to be considered in the fitting procedure. The FEFF code [36] then calculates effective scattering amplitudes and phase shifts for the various single and multiple scattering paths with atoms of the same type and at the same distance grouped into the same path. The calculations are based on a curved-wave MS theory including polarization dependence, core-hole effects and many-body interactions [42]. Paths are sorted with respect to their effective distance R_{eff} and their importance given by the scattering amplitude is listed. This enables a selection of the relevant paths to be included in the fitting procedure. The selection may vary depending on the system studied, the quality of the data and the aim of the investigation. Figure 2.9 (a) and (b) show the calculated scattering paths that were selected for the analysis of c-InP and $Ga_{0.50}In_{0.50}P$, respectively (see Chapter 5 and 6). The complex Fourier transformed paths can add up constructively or destructively depending on their phases. As an example, the peak at $R \sim 4\,\text{Å}$ in Fig. 2.9 (a) is smaller for the sum of all paths than for the second NN In path, highlighting the importance of considering the full information content of the FTs.

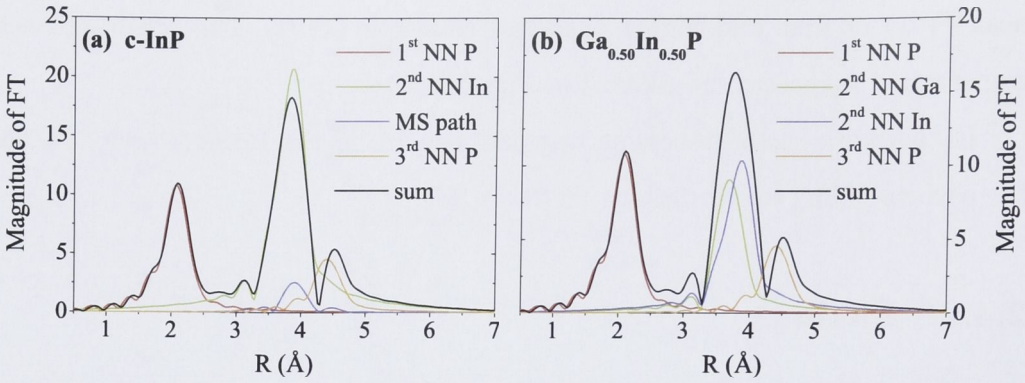

Figure 2.9: Theoretical scattering paths selected for the fitting procedure of (a) c-InP and (b) $Ga_{0.50}In_{0.50}P$. The magnitude of the FT is plotted as a function of R for the different paths and their complex sum.

The structural parameters of the selected paths are then refined in a least-squares fit to the processed experimental data. The first four cumulants ($R_{\mathrm{EXAFS}} = R_{\mathrm{eff}} + \Delta R$, $\sigma^2_{\mathrm{EXAFS}}$, C_3 and C_4) can be fixed, restrained or varied freely depending on the system studied, the quality of the data and the aim of the investigation. Fitting is often performed with multiple k-weights to minimize the correlation between the different parameters (see Eq. (2.18) in Section 2.2.3). As mentioned in Section 2.4.1, the E_0 value chosen during data processing might not correspond to the theoretically calculated threshold energy. Therefore, E_0 is usually treated as a fitting parameter and is determined from a suitable standard that was measured together with the samples of interest. Similarly, the amplitude reduction factor S_0^2 is determined from a measured standard thus accounting for intrinsic losses *and* experimental factors such as data normalization. Details of the fitting procedures chosen for the different systems studied herein can be found in the "Analysis" section of the corresponding chapters (see Sections 4.3, 5.4 and 6.4).

Chapter 3

Swift heavy ion irradiation of III-V semiconductors

InP, InAs, GaP, GaAs and the related ternary alloys $Ga_{0.50}In_{0.50}P$ and $Ga_{0.47}In_{0.53}As$ were irradiated with 185 MeV Au ions. The resulting damage formation was studied with Rutherford backscattering spectroscopy in channeling configuration. A material-dependent combination of irradiation induced damage production and annealing is proposed to explain the results.

3.1 Ion-solid interactions

3.1.1 Energy loss mechanisms

When an ion (or cluster) traverses matter it loses energy in either *elastic* or *inelastic* collisions with the target material. The projectile thus gradually slows down until it finally comes to rest at a certain depth inside the sample.

The two main components of energy loss are the *nuclear* and *electronic* stopping, $S_n = (dE/ds)_n$ and $S_e = (dE/ds)_e$, respectively, where E denotes the projectile energy and s stands for the path length. In the case of nuclear stopping, the ion loses its energy in elastic collisions with target atoms. If sufficient energy is transferred the atom is displaced and may now itself interact with other target atoms leading to so-called collision cascades. In the case of electronic stopping, the ion undergoes inelastic collisions with target electrons

resulting in excitation and ionization of the electronic system. In principle, elastic collisions with target electrons and inelastic collisions with target atoms may also take place. The latter involve nuclear excitation and/or reaction and the emission of bremsstrahlung radiation. For the projectile-energy combinations used herein, however, these processes are negligible.

Figure 3.1 (a) plots the electronic and nuclear energy loss, S_e and S_n, respectively, as a function of ion energy E for Au irradiation of InP. Clearly, the two contributions show a very different dependence on the projectile energy. In the keV to low MeV region, nuclear stopping dominates while for ions above $\sim 50\,\mathrm{MeV}$ the energy loss is predominantly electronic. In the following, these two regions will be denoted as Low Energy Ion (LEI) and Swift Heavy Ion (SHI) regimes, respectively. As already mentioned, the ion gradually slows down as it travels through the target material. Therefore, the rate of electronic and nuclear energy loss changes with depth z as shown in Fig. 3.1 (b) for InP irradiated with 185 MeV Au ions. For the first few micrometers, the energy transfer is clearly dominated by electronic interactions. In contrast, at depths larger than $\sim 10\,\mu\mathrm{m}$ the ions have lost sufficient kinetic energy for nuclear stopping to become significant. The Au ions with an initial energy of 185 MeV finally come to rest $\sim 17\,\mu\mathrm{m}$ below the surface.

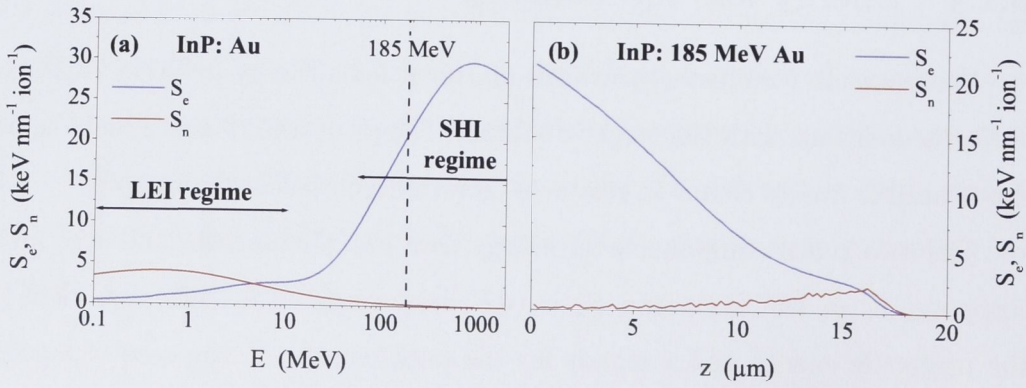

Figure 3.1: (a) Electronic and nuclear energy loss, S_e and S_n, respectively, as a function of ion energy E for Au irradiation of InP. (b) S_e and S_n versus depth z for InP irradiated with 185 MeV Au under normal incidence. Values were calculated using the SRIM2003 code [43].

3.1.2 Damage formation in crystalline materials

Depending on the material and the irradiation conditions, the energy transfer from the projectile to the target can lead to damage formation, damage annihilation or a combination of both. The damage created can range from point defects and defect clusters to complete amorphization. Given the fundamentally different energy transfer mechanisms for LEI and SHI regime, different models have been proposed to describe irradiation induced damage formation in crystalline materials.

LEI regime

In the LEI regime the energy is transferred directly to target atoms leading to atomic displacements and collision cascades. The size and density of these cascades depends on the ion-target combination and the projectile energy. Two general amorphization mechanisms have been proposed:

(i) *Heterogeneous nucleation.* Amorphous material is produced within a single ion impact. With continued irradiation these amorphous clusters accumulate to form an extended amorphous layer [44].

(ii) *Homogeneous nucleation.* Irradiation leads to the formation of defects which accumulate until a critical defect density is reached and the material collapses to the amorphous phase [45].

Heterogeneous nucleation is usually associated with high density cascades that can be described as a local volume in which either all atoms have a kinetic energy larger than the heat of melting (*Thermal Spike*) or the defect density exceeds the value that the crystal lattice can accommodate (*Displacement Spike*) [46]. An example of the latter is the vacancy-outdiffusion model by Morehead and Crowder which assumes that the size of the resulting amorphous cluster is determined by the diffusion kinetics of the vacancies produced within the cascade [44]. Gibbons overlap model accounts for both homogeneous and heterogeneous nucleation by assuming that ion bombardment creates cylindrical regions of radius r, the damage level of which depends on the irradiation conditions and determines

how many cylinders must overlap to form the amorphous phase [45]. If amorphous material is produced within a single ion impact, no overlap is needed and the amorphous fraction f_a increases with ion fluence Φ as

$$\frac{df_a}{d\Phi} = \pi r^2(1 - f_a) \qquad \rightarrow \qquad f_a = 1 - e^{-\pi r^2 \Phi}. \tag{3.1}$$

In contrast, if m overlaps are required the relation becomes

$$f_a = 1 - \sum_{k=0}^{m} \frac{1}{k!} \left(\pi r^2 \Phi\right)^k e^{-\pi r^2 \Phi}. \tag{3.2}$$

The model by Campisano *et al.* describes damage formation as the nucleation and growth of amorphous clusters based on the Avrami-Johnson-Mehl equation for the kinetics of phase transformations [47]. Hecking *et al.* also assume direct and stimulated amorphization as damage formation mechanisms but combine them with the production and accumulation of point defects and defect clusters allowing various stages of damage build-up depending on temperature and ion fluence [48].

SHI regime

In the SHI regime the energy is transferred to target electrons leading to excitation and ionization of the electronic system. This yields repulsive Coulomb forces in the highly ionized region, altered non-equilibrium interatomic potentials and electron-phonon interaction, all of which may lead to a transfer of energy from electronic excitations to atomic motion [14]. Figure 3.2 shows a schematic of the two different stages of electron and atom dynamics and the corresponding time scales. Under certain circumstances the resulting transient disorder can lead to permanent structural changes in a narrow region around the ion path, forming a so-called ion track. The ion energy threshold above which track formation is observed depends on both material and projectile.

Each of the interaction processes mentioned above has been considered as the driving force for atomic motion along the ion path. The Coulomb Explosion model, originally proposed by Fleischer *et al.* [49], assumes that the repulsive

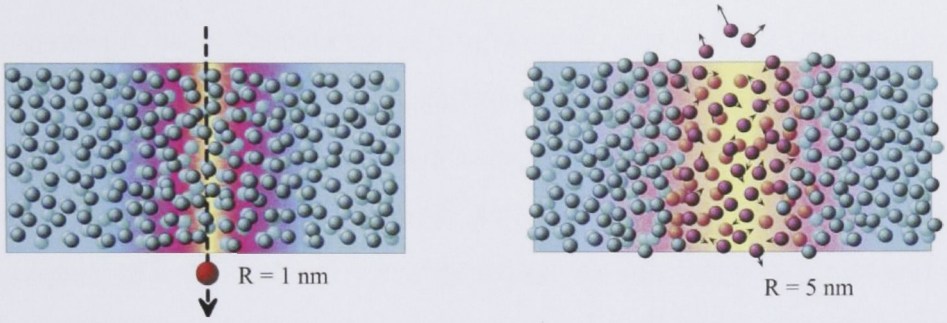

(a) Electron dynamics, $10^{-17} - 10^{-13}$ s (b) Atom dynamics, $10^{-13} - 10^{-11}$ s

Figure 3.2: Schematic of the time evolution of an ion track taken from [14].

Coulomb forces in the highly ionized center of the track lead to a collective outward motion of the target ions. This mechanism can only be significant if atomic motion is induced before charge neutralization.

In semiconductors and insulators, valence band states and conduction band states are typically of bonding and antibonding character, respectively. Stampfli argues that a high degree of electronic excitation therefore yields a weakening of covalent bonds and that the resulting structural instability persists long enough to create significant atomic disorder [50].

The Thermal Spike model assumes that the energy deposited into the electronic system is transferred to the target atoms via electron-phonon coupling [51]. This increases the thermal atomic motion and leads to melting of the material along the ion path if the temperature exceeds the melting point. The molten region may be subsequently quenched into the amorphous phase during rapid resolidification. The evolution of the thermal spike is typically described by two coupled non-linear differential equations, for example [52]

$$\begin{aligned} C_\mathrm{e}(T_\mathrm{e})\frac{\partial T_\mathrm{e}}{\partial t} &= \frac{1}{r}\frac{\partial}{\partial r}\left[rK_\mathrm{e}(T_\mathrm{e})\frac{\partial T_\mathrm{e}}{\partial r}\right] - g(T_\mathrm{e} - T_\mathrm{a}) + A(r,t) \\ C_\mathrm{a}(T_\mathrm{a})\frac{\partial T_\mathrm{a}}{\partial t} &= \frac{1}{r}\frac{\partial}{\partial r}\left[rK_\mathrm{a}(T_\mathrm{a})\frac{\partial T_\mathrm{a}}{\partial r}\right] + g(T_\mathrm{e} - T_\mathrm{a}) \end{aligned} \tag{3.3}$$

where C_e,K_e and C_a,K_a are the specific heat and thermal conductivity of electrons and atoms, respectively. T_e and T_a denote the electronic and atomic temperatures, respectively, t is the time, r is the distance from the center of the ion

track, g stands for the electron-phonon coupling efficiency and A represents the energy density deposited into the electronic system by the incident ion. The first equation thus describes the temperature evolution in the electronic system while the second equation models the lattice. The coupling term, $g(T_e - T_a)$, accounts for the energy transfer due to electron-phonon interaction. The coupling efficiency g strongly depends on the material and is usually determined empirically. The driving force for the evolution of the spike, and therefore a crucial term in Eq. (3.3), is the energy density deposited into the electronic system, $A(r,t)$. For semiconductors, Kamarou *et al.* assume the time dependence of $A(r,t)$ to be Gaussian while the spatial distribution is modeled with a "core" region given by the zone of primary ionization and a "halo" region defined by the range of the most energetic electrons produced [52, 53].

There has been much debate as to the appropriateness of the various models [13–15]. On the one hand, the main criticism of the Thermal Spike model is that it applies classical heat transport to a non-equilibrium process and that it lacks the distinction between electrons and holes [15]. On the other hand, Coulomb explosion has been ruled out as track formation mechanism for many materials among them metals and semiconductors [14, 15].

3.2 SHI induced damage formation

3.2.1 InP

Track formation and amorphization due to electronic energy deposition in InP was first reported by Herre *et al.* for irradiation with 250 MeV Xe at room temperature [54]. Using TEM, the authors find the damaged region to extend several micrometers into the sample corresponding to the range where S_e exceeds a value of $\sim 13\,\mathrm{keV\,nm^{-1}}$. A second region of heavy damage is observed at the depth of the maximum of S_n and is attributed to the effects of nuclear energy deposition. The material separating these two regions contains only point defects and small clusters. Herre *et al.* therefore conclude that $S_e \sim 13\,\mathrm{keV\,nm^{-1}}$ is the

threshold value for SHI induced track formation in InP. High irradiation fluences yield track overlap and the formation of an extended amorphous layer.

Damage formation due to electronic energy deposition in InP has since been studied using RBS in channeling configuration (RBS/c), TEM, XRD and a combination of selective chemical etching and optical microscopy [52, 55–60]. The main findings can be summarized as follows:

(i) Damage formation is determined not only by the total electronic energy deposited, S_e, but also by its radial distribution (velocity effect) [57].

(ii) Continuous tracks [52, 53, 61], discontinuous tracks [52–54, 62] and tracks with variable radii [55, 63] have been observed. Kamarou *et al.* argue that even a continuous track can appear intermittent when imaged by TEM due to regions with changing contrast [53]. In most cases, the tracks are reported to consist of amorphous material with a small amount of polycrystalline material also present [54, 55, 61].

(iii) In the sub-threshold regime multiple overlaps are necessary when fitting the damage formation determined by RBS/c as a function of ion fluence with the Gibbons overlap model (see Section 3.1.2). In contrast, damage formation above the threshold is characterized by $m = 0$ and direct impact amorphization [52].

(iv) Above the threshold, a thin surface layer of approximately $30 - 40\,\text{nm}$ remains almost undamaged even if the underlying region is already completely amorphized [58, 59]. This behavior is attributed to the incident ion having an initial charge state smaller than the equilibrium charge state and thus a lower electronic stopping power ($S_e \propto q^2$, where q is the charge state of the ion [58]).

(v) Damage formation above the threshold is significantly reduced when the irradiations are performed at liquid nitrogen temperature compared to room temperature [52, 55, 60]. Based on the Thermal Spike model, this is attributed to the higher thermal conductivity at low temperature causing the heat to be dissipated more efficiently than at room temperature [52].

(vi) SHI irradiation of InP pre-damaged with 600 keV Ge ions leads to annealing of the existing defects in the sub-threshold regime while damage formation dominates above the threshold [57].

The extended Thermal Spike model by Kamarou *et al.* (see Section 3.1.2) successfully predicts the experimental conditions under which tracks are formed in InP [52]. The simulated maximum atomic temperature inside the ion track $T_{\max}(r = 0)$ is plotted as a function of ion energy for Au, Xe and Kr irradiation in Fig. 3.3 (a). If irradiations are performed at room temperature, $T_{\max}(r = 0)$ exceeds the melting point of $T_{\mathrm{m}} = 1335\,\mathrm{K}$ for a wide energy range of Au and a smaller energy range of Xe but not for Kr. For Au or Xe irradiation with the same energies but performed at liquid nitrogen temperature $T_{\max}(r = 0)$ does not reach the melting point and hence no amorphous tracks are formed. The calculated maximum radius of the molten zone r_{sim} is plotted versus ion energy for Au and Xe irradiations at room temperature in Fig. 3.3 (b). Good agreement with TEM measurements is observed.

3.2.2 Other IV and III-V semiconductors

InSb is more susceptible to SHI induced damage formation than InP [53,63]. However, the material becomes porous at fluences lower than that necessary for complete amorphization rendering studies at higher fluences difficult [53]. Single ion tracks were also reported for GaSb and InAs after 385 and 830 MeV Pb irradiation, respectively, whereas no tracks were detected with TEM for GaAs, Ge and Si even with 2.1 GeV Pb [63]. In contrast, Komarov *et al.* observed tracks with optical microscopy in GaAs after irradiation with very small fluences of 710 MeV Bi or 1.3 GeV U and selective chemical etching [56]. However, the tracks extend almost to the end of the ion range and their origin (electronic or nuclear energy deposition or both) is thus not easily identified. At higher ion fluences, selective etching was not observed which the authors attribute to defect annealing during subsequent SHI irradiation. The annealing of pre-existing defects due to high electronic energy deposition in GaAs was also reported by

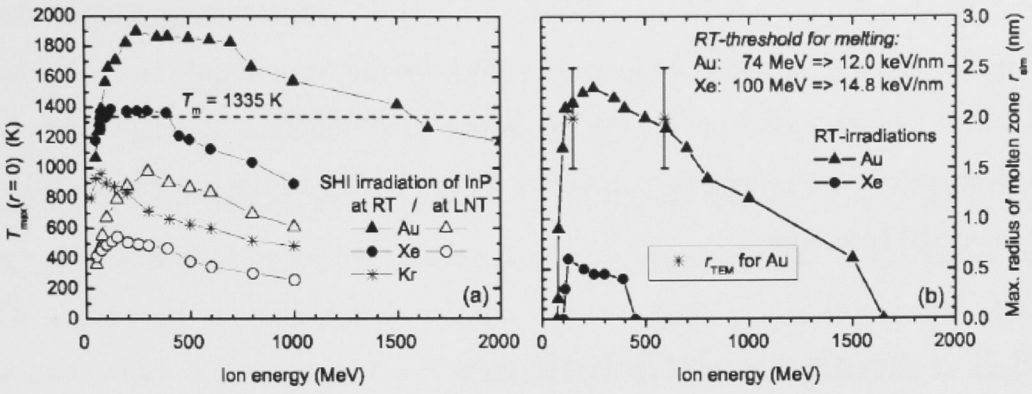

Figure 3.3: (a) Maximum atomic temperature $T_{\max}(r = 0)$ at the ion track axis and (b) maximum radius r_{sim} of the molten zone versus ion energy for InP. The dashed line in (a) represents the melting point. The stars in (b) give experimental track radii for Au irradiation determined with TEM. Graphs are taken from [52].

Wesch *et al.* for samples pre-damaged by ion irradiation in the keV range [64]. The defect concentration determined with RBS/c measurements due to 593 MeV Au irradiation did not exceed a few percent for GaAs, GaP, AlAs and Ge even after fluences of several $10^{14}\,\text{cm}^{-2}$ [12]. The damage produced is identified as point defects and defect clusters using optical and electrical techniques [65] and is attributed to the small but non-zero nuclear energy deposition [12].

The situation is clearly different when irradiations are performed with highly energetic clusters such as C_{60} instead of single ions highlighting again the importance of the deposited energy *density* and its radial distribution. Amorphous tracks are created due to C_{60} impact in Si, Ge and GaAs ([64] and references therein). For Si and Ge, the areal track density equals the cluster fluence and a direct impact process is operative. Applying their extended Thermal Spike model to these materials, Kamarou *et al.* simulated the temperature evolution during the spike and the resulting track radii are in good agreement with experimental findings [53]. Similar calculations for single ion irradiation of Si and Ge show that the maximum temperature inside the track is well below the melting point for all ion energies and thus tracks are not formed. For GaAs, the number of tracks is significantly smaller than the cluster fluence and the use of a direct impact model is not meaningful [53].

No simulations have been performed for III-V semiconductors other than InP. It therefore remains an open question why the response of the III-V compounds to high electronic energy deposition is so different and more detailed investigations are needed to gain better understanding of the processes involved under SHI irradiation.

3.3 Analytical techniques

3.3.1 Rutherford backscattering spectroscopy

RBS examines the energy spectrum of He ions backscattered from a target at a fixed angle, typically $\sim 170°$. The incident He ions have an initial energy E_0. While most ions penetrate deep into the sample, some undergo elastic scattering in the Coulomb potential of the target nuclei. The scattering angle θ is determined by the smallest distance in which the ion would pass the nucleus if there was no interaction between them, the so-called impact parameter. The energy of the backscattered ion E_i depends on the scattering angle θ, the initial ion energy E_0 and the mass of the target atom m_i. From the conservation of energy and momentum, E_i can be expressed by

$$E_i = K_i E_0 = \left[\frac{\cos\theta + \sqrt{(m_i/m_{\mathrm{He}})^2 - \sin^2\theta}}{1 + (m_i/m_{\mathrm{He}})} \right]^2 E_0 \tag{3.4}$$

where K_i is the kinematic factor and m_{He} denotes the mass of the He ion [66]. Thus, the higher the target mass, the higher the energy of the backscattered ion for fixed θ. Ions traveling through the target without undergoing backscattering still suffer a small energy loss ΔE due to other interactions with the material such as inelastic or small angle elastic scattering events [66]. For an ion backscattered at depth z, Eq. (3.4) thus becomes

$$E_i(z) = K_i \left(E_0 - \Delta E_{in}\right) - \Delta E_{out} \tag{3.5}$$

where ΔE_{in} and ΔE_{out} denote the energy loss on the way in and out, respectively. The number $\mathrm{d}Y_i$ of ions backscattered at target atoms i in the depth interval $\mathrm{d}z$

can be written as

$$dY_i = N \left(\frac{d\sigma}{d\Omega} \right)_i \Delta\Omega \rho_i^{\mathrm{p}} dz. \tag{3.6}$$

Here N is the number of incident ions, $\Delta\Omega$ stands for the solid angle of the detector and ρ_i^{p} denotes the particle density of species i. $(d\sigma/d\Omega)_i$ represents the differential scattering cross section, usually taken as the Rutherford cross section which is proportional to the square of the atomic number of the target nucleus, $(d\sigma/d\Omega)_i \propto Z_i^2$ [66]. The energy spectrum of the backscattered ions thus contains the following information:

(i) For a fixed scattering depth, the energy E_i provides information about the different elements present in the sample. For scattering at a given element, E_i yields information about the depth distribution of this element.

(ii) The yield contains information about the ratio in which different elements are present in the sample at a certain depth.

As an example, Fig. 3.4 shows the RBS spectra for Co/Si and SiO_2 measured with 2 MeV He and $\theta = 168°$. The two schematics illustrate backscattering at different elements i in different depths z and the resulting energies $E_i(z)$.

In crystalline targets the backscattering yield decreases drastically if the ions are incident parallel to a low index axis, an effect known as *channeling*. The ions entering the sample can be guided in the channels formed by atomic rows

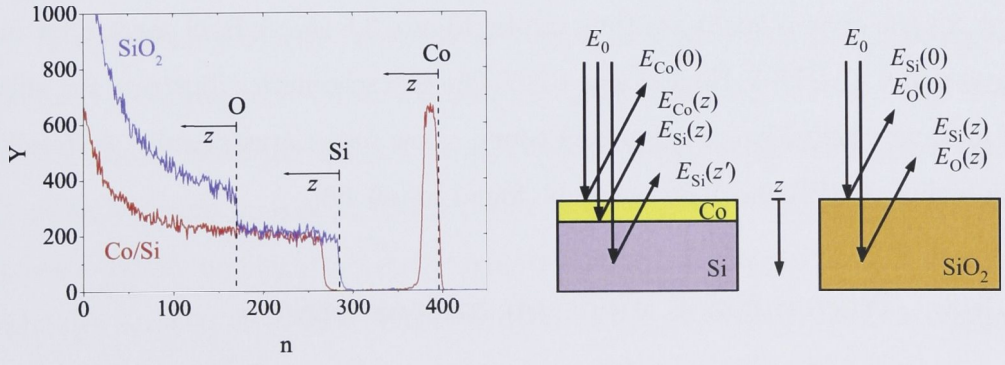

Figure 3.4: Backscattering yield Y versus channel number n for Co/Si and SiO_2 and scattering schematics showing the resulting He energies. Measuring a set of known calibration samples, n can be converted to backscattered ion energy E.

thus reducing the probability for backscattering events. Progressive small angle scattering results in loss of alignment between the ion direction and the crystal axis and thus leads to an increase of backscattering probability with increasing depth, called *dechanneling*. Channeling takes place if the angle between ion direction and crystal axis is smaller than a critical angle ψ_{crit} which can be estimated as

$$\psi_{\mathrm{crit}} = \left(\frac{\mathrm{e}^2}{4\pi\varepsilon_0} \frac{2Z_i Z_{\mathrm{He}}}{Ed} \right)^{\frac{1}{2}} \tag{3.7}$$

where e is the elementary charge, ε_0 is the electric constant, E is ion energy and d represents the distance between two target atoms along the crystal axis [66,67]. The minimum yield $\chi_{\mathrm{min}} = Y_{\mathrm{al}}/Y_{\mathrm{ra}}$ is defined as the ratio of the yields measured in aligned and random orientation, Y_{al} and Y_{ra}, respectively. Ions can also be guided in one dimension when incident parallel to a crystal plane, a situation called *planar channeling*. The reduction in backscattering yield is not as pronounced as for axial channeling but still significant.

Crystal defects consist of atoms that are displaced from their ideal lattice sites and can thus act as backscattering centers even for ions incident under a channeling configuration. The backscattering yield measured in aligned orientation increases with increasing number of defects until it reaches the yield measured in a random direction or for amorphized material. The minimum yield can thus be used to estimate the concentration of defects and serves as a measure for the crystal quality of the sample. Figure 3.5 shows RBS spectra for InP measured with 2 MeV He and $\theta = 168°$. The two schematics illustrate the effect of random orientation or alignment along a low index crystal axis. A detailed discussion of RBS and RBS/c can be found in [66–68].

3.3.2 Transmission electron microscopy

TEM studies the electron beam transmitted through a very thin target, typically 0.1 μm thick. The incident electrons can either pass through the sample undisturbed (direct beam) or undergo elastic scattering with the target nuclei

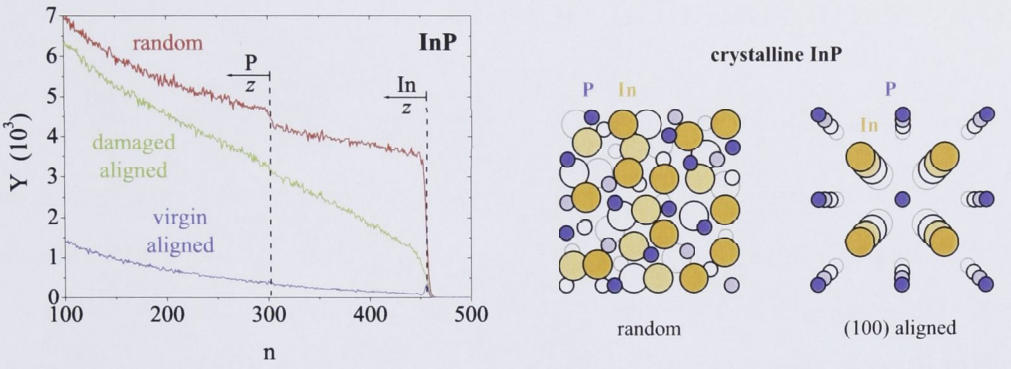

Figure 3.5: Backscattering yield Y versus channel number n for crystalline InP and schematics showing the effect of random and aligned orientation.

(scattered beam). Elastic scattering with target electrons and inelastic scattering also take place but usually play a minor role in basic TEM imaging although the resulting signals are exploited for other electron microscopy techniques. A very small fraction of the incident electrons is absorbed in the target and therefore does not contribute to the transmitted beam.

Elastic scattering with target nuclei is governed by the Rutherford cross section which is proportional to Z_i^2 [66]. Thus more electrons are scattered in high-Z material compared to low-Z material. Furthermore, thick samples yield stronger scattering of the electron beam than thin samples. Selecting either the direct (bright field, BF) or the scattered (dark field, DF) beam with an objective aperture and detecting the transmitted intensity with a fluorescent screen, photographic film or CCD camera yields an image with Z and/or thickness contrast.

In crystalline materials, coherent scattering of the electron beam (Bragg diffraction) gives rise to a diffraction pattern characteristic of the structure under investigation. Selecting special Bragg reflections by tilting the sample correspondingly yields images in which the area that satisfies the Bragg condition appears darker or brighter for BF and DF imaging, respectively. Using this technique, crystal structure, orientation and defects can be studied. A comprehensive discussion of the various aspects of TEM can be found in [69].

3.4 Experimental details

3.4.1 Irradiation

For the binary compounds single-crystal wafers of (100) orientation were used. Ternary alloys were grown as $Ga_{0.47}In_{0.53}As$/InP [2.5 μm/(100) substrate] and $Ga_{0.50}In_{0.50}P$/AlAs/GaAs [2.5 μm/50 nm/substrate] heterostructures by metal organic chemical vapor deposition. For the latter, GaAs substrates with a 10° miscut relative to the (100) direction were used to inhibit ordering of the mixed Ga/In sublattice. The chosen stoichiometries are lattice matched to their respective substrates yielding ternary alloys free of misfit dislocations. All compounds were nominally undoped. The material was cut into $5 \times 25\,mm^2$ strips and mounted on Al blocks with carbon paste to facilitate electrical and thermal contact. Irradiations were performed at room temperature with 185 MeV Au^{13+} ions at the Heavy-Ion Accelerator Facility of The Australian National University, Canberra, which is shown in Fig. 3.6. The beam was scanned over an area of $3 \times 6\,mm^2$ to ensure homogeneously irradiated samples. Fluences ranged from 2×10^{11} to $3 \times 10^{14}\,cm^{-2}$. For InP the beam current was maintained between 5 and 10 nA resulting in power densities below $1\,W\,cm^{-2}$. For the other materials, the beam current was varied between 5 and 50 nA to achieve higher ion fluences in feasible irradiation times. To avoid heating, the sample stage was cooled using a hydrocarbon based coolant (Shellsol D70) maintained at room temperature.

The precise measurement of irradiation fluences is not trivial. In this work, the ion fluence was determined by integrating the current measured on the sample holder. This method requires reasonable conductivity of the sample irradiated and thorough suppression of the secondary electrons created under ion impact. To calibrate the fluence measurement, small MoO_3 crystals of up to a few micrometers in size were irradiated with fluences of less than $2 \times 10^{11}\,cm^{-2}$. The crystals were deposited on holey carbon supported by a standard TEM Cu grid. Each incoming SHI creates a hole in the thin MoO_3. The real irradiated fluence can then be obtained by counting the ion impacts within a given area on

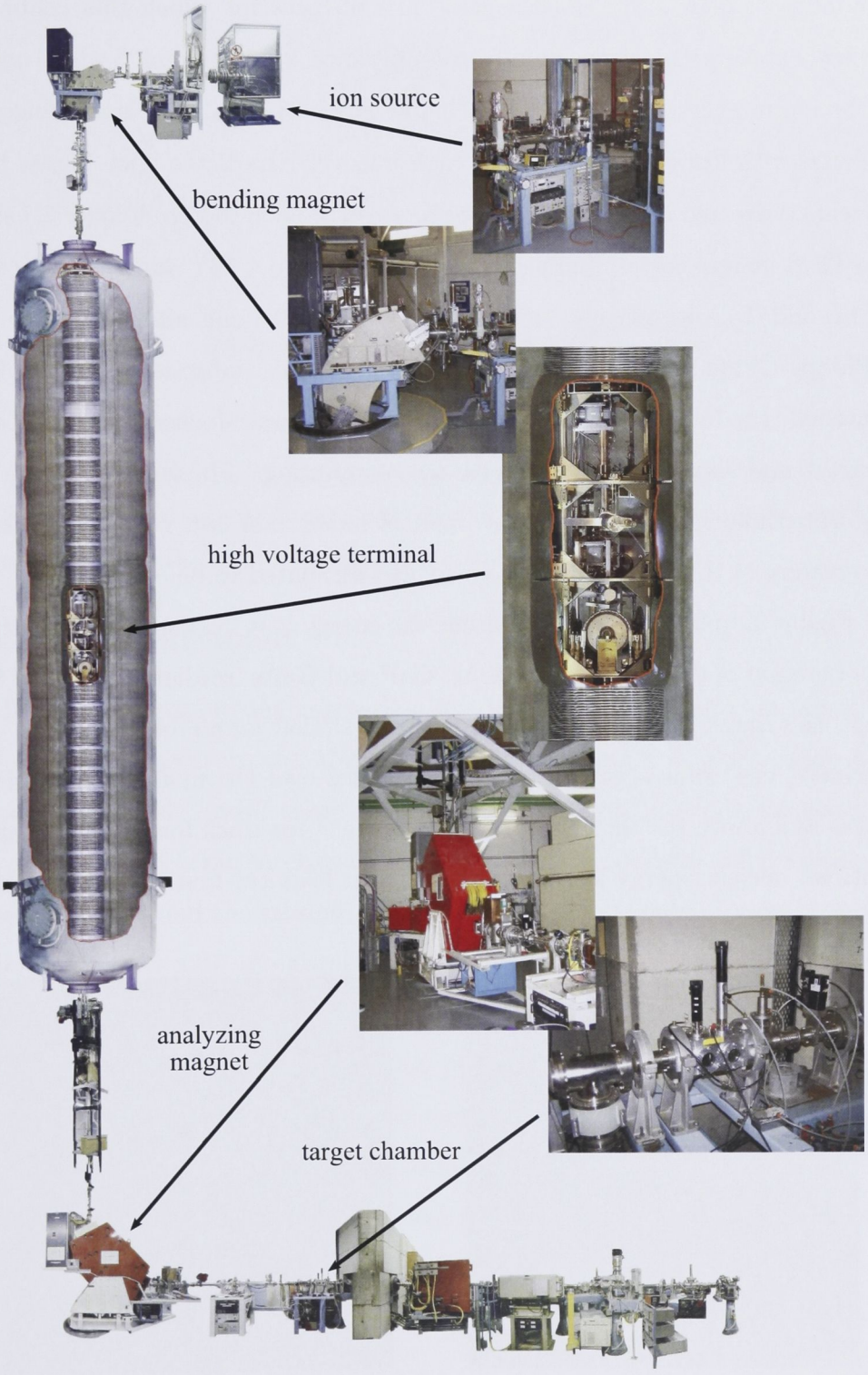

Figure 3.6: Layout of the Heavy-Ion Accelerator Facility at The Australian National University, Canberra. The machine is setup vertically with the ion source at the top and the experimental stations at the bottom.

a number of planview TEM images. The fluences for which this calibration method can be applied successfully are limited to a few $10^{11}\,\mathrm{cm}^{-2}$ where overlap of the ion impacts is still small. A change in calibration from low fluences (irradiated with low beam current) to high fluences (irradiated with higher beam current) is deemed unlikely but cannot be ruled out completely. Figure 3.7 shows two TEM images corresponding to a real fluence of 4×10^{10} and $1.3 \times 10^{11}\,\mathrm{cm}^{-2}$ for (a) and (b), respectively. Both images are $0.4 \times 0.4\,\mu\mathrm{m}^2$ and were taken with a Philips CM300 operating at 300 kV. Since no size information of the holes is needed, the images were taken with the beam under-focused to enhance the contrast and thus improve the accuracy of counting. Fluence calibration was performed multiple times over the span of more than two years. The overall uncertainty of the fluence measurement was estimated to be $\sim 20\,\%$.

Figure 3.8 plots electronic and nuclear energy loss, S_e and S_n, respectively, as a function of depth z for InP, InAs, GaP and GaAs irradiated with 185 MeV Au. The values of both contributions are very similar for all four materials. Furthermore, electronic stopping clearly dominates over the first few micrometers and is well above the threshold of $\sim 13\,\mathrm{keV\,nm}^{-1}$ for track formation in InP. In contrast, nuclear energy loss is negligible for at least the first few micrometers.

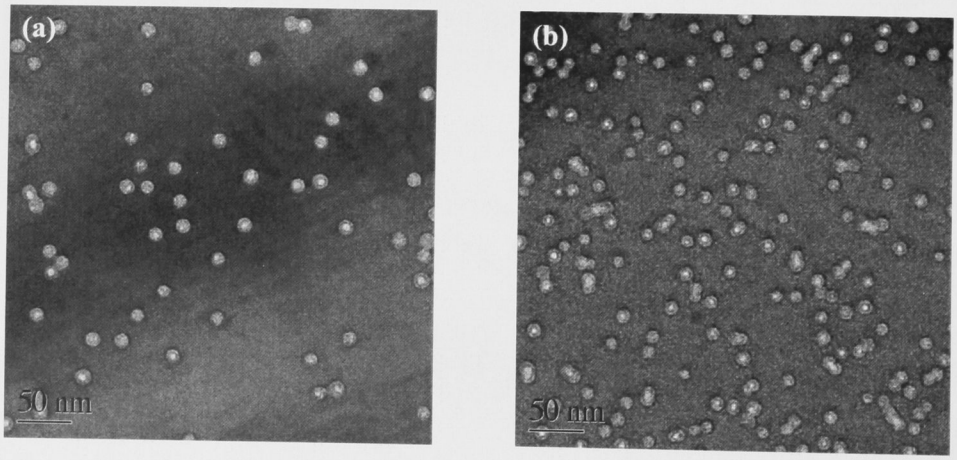

Figure 3.7: Planview TEM images of thin MoO_3 irradiated with 185 MeV Au to a fluence of (a) $4 \times 10^{10}\,\mathrm{cm}^{-2}$ and (b) $1.3 \times 10^{11}\,\mathrm{cm}^{-2}$. Both images are $0.4 \times 0.4\,\mu\mathrm{m}^2$. The holes created in the MoO_3 due to the ion impacts are visible as bright spots.

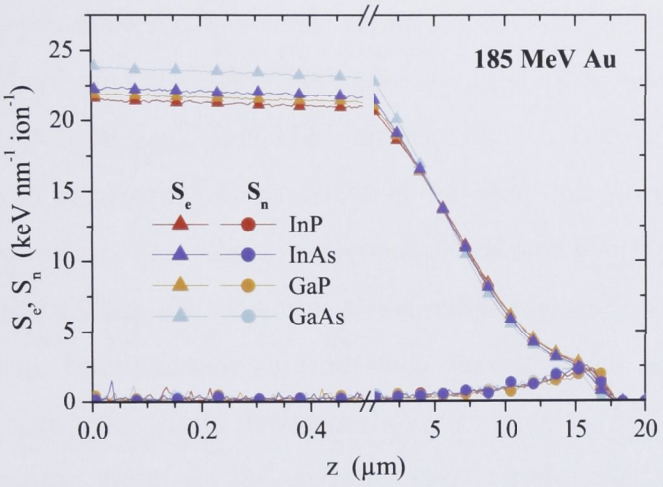

Figure 3.8: Electronic and nuclear energy loss, S_e and S_n, respectively, versus depth z for InP, InAs, GaP and GaAs. Values were calculated with the SRIM2003 code [43]. Note the break in depth scale at $z = 0.5\,\mu$m.

3.4.2 Measurement

Damage formation was analyzed with RBS/c measurements recording the backscattering spectrum of 2 MeV He ions under an angle of 168°. Each sample was measured several times with no significant effect of the He beam on the damage concentration observable. A channeling spectrum of unirradiated material, $Y_{\mathrm{al}}^{\mathrm{unirr}}$, and the random spectrum, Y_{ra}, were recorded for each strip of material together with the aligned spectra of the irradiated samples, $Y_{\mathrm{al}}^{\mathrm{irr}}$.

Cross section TEM samples were prepared with the small-angle cleavage technique to avoid sample preparation artifacts arising from heating and ion beam milling [70, 71]. The irradiated material was thinned to 130 μm by mechanical grinding and then cleaved to produce a wedge of $\sim 12°$ with a thin electron transparent tip. The wedge was mounted on a Cu ring and studied in cross section geometry using a Philips CM300 operating at 300 kV.

3.5 Analysis

Backscattering events from different elements that results in the same ion energy occur at different depths. Therefore, only the part of the RBS spectra

that comprises scattering from a single element was used in the analysis. Taking the In signal, this yields an accessible depth of $z > 0.5\,\mu$m for InP, $z \sim 0.21\,\mu$m for $Ga_{0.50}In_{0.50}P$ and $z \sim 0.18\,\mu$m for InAs and $Ga_{0.47}In_{0.53}As$. The Ga signal up to $z = 0.5\,\mu$m was used for GaP. Given the proximity of the Ga and As edges, basically the whole RBS spectrum of GaAs contains scattering from both elements. Thus, the slight difference in depth for Ga and As has been neglected and the sum of the scattering contributions was analyzed up to $z = 0.5\,\mu$m. From $\chi_{\min} = Y_{\mathrm{al}}/Y_{\mathrm{ra}}$ the relative concentration of displaced atoms, n_{da}, was calculated using the computer code DICADA [73] assuming randomly distributed point defects. DICADA describes axial dechanneling in compound crystals based on the approaches by Lindhard and Gärtner *et al.* [73]. Thermal vibrations of the lattice atoms are treated according to the Debye model (see Section 5.1.2). Table 3.1 summarizes the Debye temperatures Θ_{D}, lattice constants a and particle densities ρ^{P} used for the different materials. The normalized relative defect concentration, n_{def}, was then determined by $n_{\mathrm{def}} = (n_{\mathrm{da}}^{\mathrm{irr}} - n_{\mathrm{da}}^{\mathrm{unirr}})/(1 - n_{\mathrm{da}}^{\mathrm{unirr}})$. Thus, $n_{\mathrm{def}} = 0$ and $n_{\mathrm{def}} = 1$ correspond to unirradiated and amorphized material, respectively. In the following, n_{def} will be referred to simply as the defect concentration.

Figure 3.9 (a) shows the RBS/c spectra for InP irradiated with three different fluences of 185 MeV Au. The unirradiated aligned and random spectra are also plotted. The depth profiles of n_{def}, calculated using the DICADA code, are

		InP	$Ga_{0.50}In_{0.50}P$	GaP	InAs	$Ga_{0.47}In_{0.53}As$	GaAs
Θ_{D}	(K)	425	204 (*)	445	280	330	360
a	(Å)	5.8687	5.653	5.4505	6.0583	5.8687	5.6532
ρ^{P}	($10^{22}\,\mathrm{cm}^{-3}$)	3.96	4.46	4.94	3.59	3.98	4.42

Table 3.1: Debye temperature Θ_{D}, lattice constant a and particle density ρ^{P} at 300 K. All values are taken from [3] except (*) which is taken from [72]. Note that this value of Θ_{D} for $Ga_{0.50}In_{0.50}P$ is in stark contrast to those of InP and GaP. Performing the calculations with $\Theta_{\mathrm{D}} = 435\,\mathrm{K}$ instead of $\Theta_{\mathrm{D}} = 204\,\mathrm{K}$ yields defect concentrations that are systematically higher but still with experimental uncertainty.

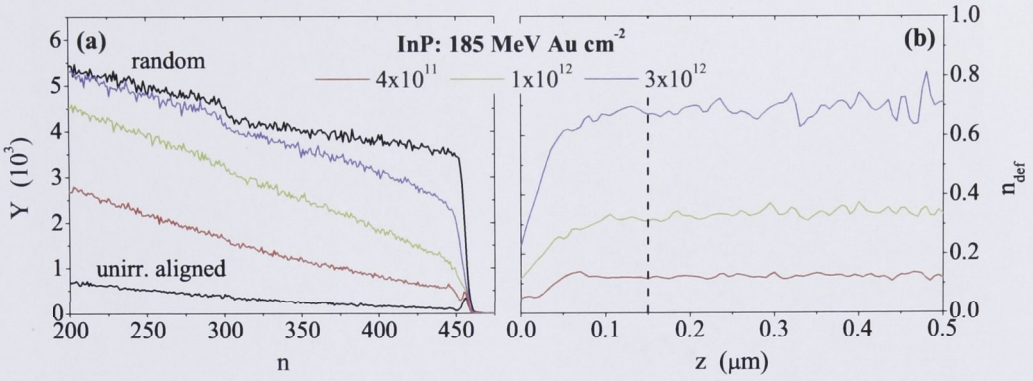

Figure 3.9: (a) Backscattering yield Y measured in channeling configuration versus channel number n for InP irradiated with 185 MeV Au. Also given are the aligned spectrum of unirradiated InP and the spectrum measured in random direction. (b) Defect concentration n_{def} versus depth z as obtained with the DICADA code [73] from the spectra shown in panel (a).

given in Fig. 3.9 (b). For $z > 0.05\,\mu$m the defect level remains almost unchanged corresponding to the nearly constant value of electronic energy loss in this region (see Fig. 3.8). The remarkably low level of damage in the region $z < 0.05\,\mu$m is consistent with previous findings and has been attributed to charge state effects of the incoming ions (see Section 3.2.1) [58,59]. Taking the defect concentration at a fixed depth, in this case at $z = 0.15\,\mu$m (see dashed line in Fig. 3.9 (b)), the damage formation can be evaluated as a function of ion fluence Φ. The uncertainty related to measurement and analysis was estimated to $\sim 10\,\%$ for $n_{\mathrm{def}} > 0.2$ and 0.02 for $n_{\mathrm{def}} < 0.2$.

3.6 Results and discussion

3.6.1 Binary compounds

Figure 3.10 (a) shows a cross section TEM image of InP irradiated with 185 MeV Au to a fluence of $4\times10^{10}\,\mathrm{cm}^{-2}$. The damage created under SHI irradiation is clearly visible as dark streaks running from top to bottom. Most of these tracks appear discontinuous consistent with previous observations [53, 62, 63]. This intermittent structure could be caused by two different effects [53]. Elec-

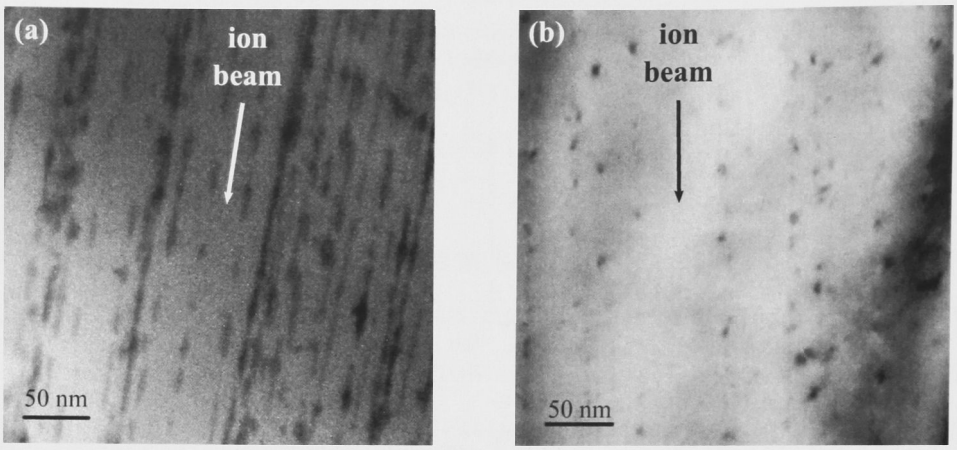

Figure 3.10: Cross section TEM images of (a) InP and (b) InAs irradiated with 185 MeV Au to a fluence of $4 \times 10^{10}\,\mathrm{cm}^{-2}$ and $1.2 \times 10^{11}\,\mathrm{cm}^{-2}$, respectively. Both images correspond to an area of $0.32 \times 0.32\,\mu\mathrm{m}^2$ and were taken at a depth of $z \sim 3\,\mu\mathrm{m}$.

tron capture and loss processes could lead to fluctuations of the ion charge state around the equilibrium value and hence to fluctuations of the electronic energy loss. Values that are alternately above and below the threshold for track formation would then yield a statistically discontinuous ion track. Alternatively, if the passage of the ion results in local melting, the liquid phase could change from a continuous molten cylinder to droplets due to surface tension (Rayleigh instability). Rapid resolidification would then lead to pockets of damaged material along the ion trajectory. The radii of the damaged zones visible in Fig. 3.10 (a) are between 3 and 4 nm in agreement with the findings of Kamarou *et al.* [52].

Figure 3.10 (b) shows a cross section TEM image of InAs irradiated with 185 MeV Au to a fluence of $1.2 \times 10^{11}\,\mathrm{cm}^{-2}$. Note that due to the variable thickness of cross section samples the number of ions that were incident on the imaged area is not quantifiable. Relating the number of tracks to the irradiated fluence or quantitatively comparing the two different samples is thus not possible. Qualitatively however, tracks are clearly visible for InP whereas the damaged zones in InAs are isolated and more spherical in shape. Given the electronic energy deposition calculated by the SRIM2003 code [43] is similar in both materials (see Fig. 3.8), the TEM cross section images are consistent with a higher threshold for track formation in InAs compared to InP and/or more

pronounced annealing of the damage in InAs than in InP (see below). No TEM studies on SHI irradiated InAs have been reported previously.

Figure 3.11 (a) and (b) show the defect concentration n_{def}, measured with RBS/c and taken at a depth of $z = 0.15\,\mu$m, as a function of ion fluence Φ for InP and InAs, respectively. The open symbols represent the measured values with different symbols corresponding to different sample holders. The full circles denote the average of the binned data. From Fig. 3.11 it is clear that the variation of data points is significantly larger than the uncertainty associated with measurement and analysis, in particular for InP (see Fig. 3.11 (a)). Several tests were thus performed with InP to clarify the source of this variation:

(i) RBS/c measurements performed two days, one and a half months and ten months after irradiation yielded the same defect concentration within uncertainty. This shows that no damage relaxation observable with RBS occurs in InP irradiated with 185 MeV Au and stored at room temperature. Furthermore, it demonstrates that the RBS/c measurements are reproducible within the estimated uncertainty of ~10 %.

(ii) Irradiation under an incident angle of 0° or 7.5° had no effect on the damage production and thus no channeling effects of the incident ions are apparent.

(iii) Irradiation with the same fluence four times on the same sample holder

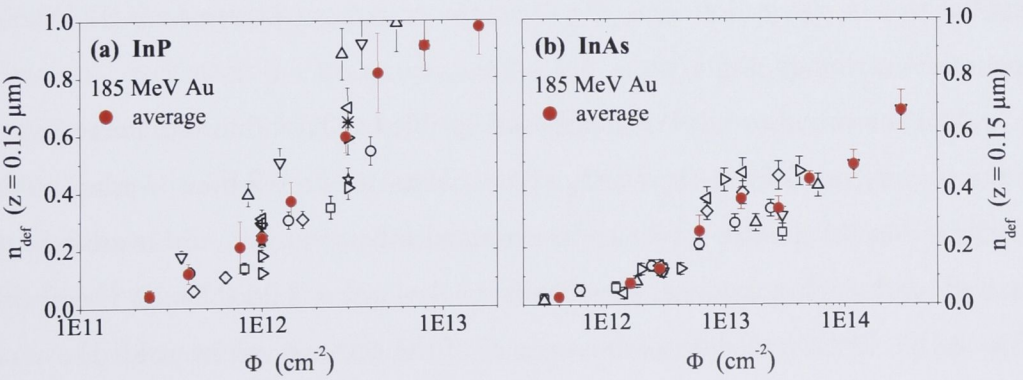

Figure 3.11: Defect concentration n_{def} at $z = 0.15\,\mu$m versus ion fluence Φ for (a) InP and (b) InAs irradiated with 185 MeV Au. The open symbols represent the data points (with different symbols corresponding to different sample holders) while the full circles give the average values of the binned data.

resulted in $\sim 15\,\%$ variation from the average value. This is within the range corresponding to $\sim 20\,\%$ uncertainty in ion fluence.

(iv) Irradiation without cooling the sample holder gave values $\sim 40\,\%$ higher than those obtained with cooling. (Note that for all other samples the stage was cooled during irradiation.)

It can thus be concluded that the variations observed in Fig. 3.11 are not caused by the RBS/c measurement or channeling effects of the incident ions. Uncertainties of the fluence measurement contribute to the spread but cannot account for all of it. Differences in thermal and electrical conductivity between material and sample holder may be another source of the variation.

Figure 3.12 shows n_{def}, taken at $z = 0.15\,\mu\mathrm{m}$, versus ion fluence Φ for InP, InAs, GaP and GaAs. For InP and InAs, the averaged values from Fig. 3.11 are plotted. For GaP and GaAs, all data points are given (with different symbols corresponding to different sample holders). InP is characterized by a strong increase of defect concentration with ion fluence and is rendered amorphous for $\Phi \sim 1 \times 10^{13}\,\mathrm{cm}^{-2}$. InAs also exhibits damage but only at fluences much higher than those required for InP. In contrast, only little damage is observed in GaP and GaAs and n_{def} remains below 0.1 even after irradiation with $\Phi = 2 \times 10^{14}\,\mathrm{cm}^{-2}$ consistent with the results of Wesch *et al.* [12]. Given the similarities in energy loss (see Fig. 3.8), the response of these four III-V compounds is strikingly different.

As discussed above, InP is highly susceptible to SHI induced damage formation. A very good fit of the average data points to the Gibbons overlap model (see Section 3.1.2 with $f_{\mathrm{a}} = n_{\mathrm{def}}$) is obtained for $m = 0$ (i.e. no overlap is required) and yields a damage cross section of $A = \pi r^2 = 3.2 \pm 0.2 \times 10^{-13}\,\mathrm{cm}^2$ (see Fig. 3.12). Fitting all data points instead of the average values yields the same result. The corresponding ion track radius equals $r = 3.2 \pm 0.1\,\mathrm{nm}$ in agreement with the values of $r = 2.3 \pm 0.1\,\mathrm{nm}$ and $r = 3.0 \pm 0.2\,\mathrm{nm}$ reported by Kamarou *et al.* [52] for 150 MeV and 593 MeV Au, respectively, and $r = 3 - 4\,\mathrm{nm}$ observed by Szenes *et al.* [63] after Pb irradiation with ion energies between 380 MeV and

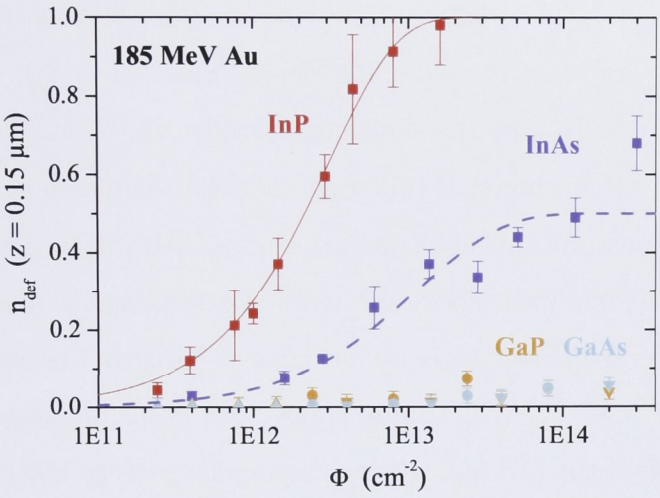

Figure 3.12: Defect concentration n_{def} at $z = 0.15\,\mu$m versus ion fluence Φ for InP, InAs, GaP and GaAs. The solid and dashed line present a fit with Gibbons model and the modified model, respectively (see below).

2.1 GeV. All these values were obtained from RBS/c measurements fitted to the Gibbons model. They agree well with the radii determined from TEM (this study and [52]). Note that while the RBS/c technique does provide information about the size of the damaged zone it is insensitive to the nature of the track (amorphous or polycrystalline, continuous or intermittent).

The InAs data cannot be fitted using the Gibbons model (Eq. (3.1) or (3.2)). An extension of the model is therefore proposed, taking into account possible SHI induced damage annihilation. Annealing of pre-existing defects due to high electronic excitation has been reported for InP and GaAs [57,64]. Furthermore, solid phase epitaxial regrowth in III-V semiconductors occurs due to thermal activation [74] and electron irradiation [75]. The amount of annealing in such a process would be proportional to the area of the damaged-crystalline interface. The latter depends on the size and morphology of the damaged area and is thus not easily accessible. Nevertheless, the amount of annealing should be proportional to n_{def} since only damaged material can anneal and to $(1 - n_{\mathrm{def}})$ since the crystalline region has to serve as a template for epitaxial growth. A modified model with

$$\frac{\mathrm{d}n_{\mathrm{def}}}{\mathrm{d}\Phi} = A(1 - n_{\mathrm{def}}) - Bn_{\mathrm{def}}(1 - n_{\mathrm{def}}) \tag{3.8}$$

is thus assumed. The dashed blue line in Fig. 3.12 was obtained with $A = 5 \times 10^{-14}\,\mathrm{cm}^2$ and $B = 1 \times 10^{-13}\,\mathrm{cm}^2$. Since $B = 2A$, the curve saturates at $n_{\mathrm{def}} = 0.5$. Despite the agreement between the fit and the experimental data, it cannot be concluded at this stage that the complex processes of damage formation and possibly annealing operative under SHI irradiation are sufficiently described by the modified model and more experiments are necessary to assess its validity. Nevertheless, the onset of damage formation is well characterized by $A = 5 \pm 1 \times 10^{-14}\,\mathrm{cm}^2$. This is almost one order of magnitude less than the value obtained for InP and reflects the smaller susceptibility of InAs to SHI induced damage formation [63]. The corresponding track radius amounts to $r = 1.3 \pm 0.3\,\mathrm{nm}$ compared to $r = 2.2\,\mathrm{nm}$ obtained by Szenes *et al.* for 830 MeV Pb irradiation [63]. No simulations of the temperature inside the ion track and the size of a potential molten zone have been performed for InAs yet.

3.6.2 Ternary alloys

As apparent in Fig. 3.12, the In compounds show considerable damage under SHI irradiation whereas the Ga compounds remain crystalline. Therefore the question arises of how ternary alloys with a mixed Ga/In sublattice behave when irradiated under the same conditions. Similar studies in the LEI regime found that $Ga_{1-x}Al_xAs$ shows a behavior intermediate to that of GaAs and AlAs over the whole compositional range [76] while for other ternary alloys, such as $Ga_{1-x}In_xAs$ and $Ga_{1-x}In_xP$, some stoichiometries are more easily amorphized than both binary compounds [77]. Note, however, that all binary compounds studied are amorphized by ion irradiation in the LEI regime (albeit at different fluences) whereas the response of the Ga compounds to SHI irradiation does not suggest amorphization even at higher fluences.

Figure 3.13 plots the defect profiles produced by 185 MeV Au in (a) InP, GaP and $Ga_{0.50}In_{0.50}P$ irradiated with $\Phi \sim 8 \times 10^{12}\,\mathrm{cm}^{-2}$ and (b) InAs, GaAs and $Ga_{0.47}In_{0.53}As$ irradiated with $\Phi = 6 - 8 \times 10^{13}\,\mathrm{cm}^{-2}$. The defect profile for $Ga_{0.50}In_{0.50}P$ (Fig 3.13 (a)) is very similar in shape albeit slightly lower than that

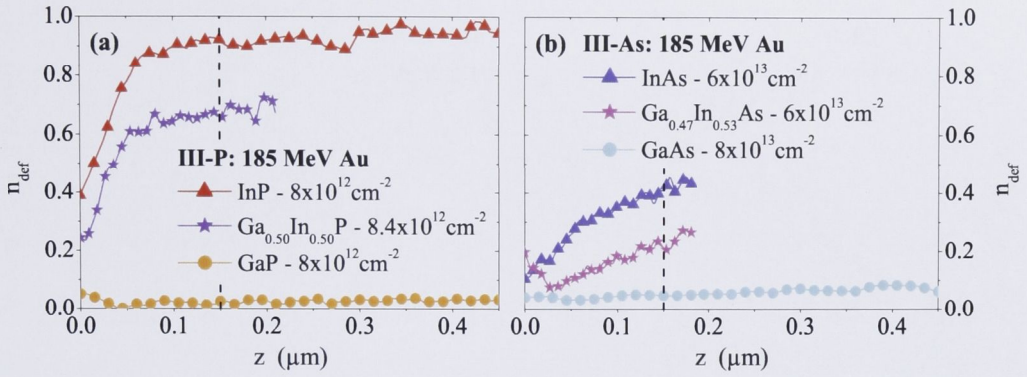

Figure 3.13: Defect concentration n_{def} versus depth z for (a) InP, $Ga_{0.50}In_{0.50}P$ and GaP and (b) InAs, $Ga_{0.47}In_{0.53}As$ and GaAs irradiated with 185 MeV Au. The dashed line at $z = 0.15\,\mu$m indicates the depth at which $n_{\mathrm{def}}(\Phi)$ is evaluated.

of InP indicating a very similar behavior of these two materials in contrast to that observed for GaP. The defect profile for $Ga_{0.47}In_{0.53}As$ is intermediate to those of InAs and GaAs but shows a slope similar to that of InAs for $z > 0.05\,\mu$m.

Figure 3.14 (a) and (b) plot n_{def} at $z = 0.15\,\mu$m versus ion fluence Φ for P and As compounds, respectively. Damage formation in $Ga_{0.50}In_{0.50}P$ (Fig. 3.14 (a)) is very similar to that observed for InP although slightly higher fluences are required to amorphize the ternary material. Given the radiation resistance of GaP, a change in damage susceptibility is expected with increasing Ga content in the ternary alloy. Whether this change occurs gradually over a large compositional range or abruptly at a certain stoichiometry is not yet known. It is clear, however, from the results presented herein, that a ternary alloy with equal parts of In and Ga behaves much more like InP than GaP, indicating that a larger Ga content is needed to significantly reduce the materials susceptibility for SHI induced damage formation. The best-fitting Gibbons curve for $Ga_{0.50}In_{0.50}P$ (solid purple line) yields $A = 1.8 \pm 0.2 \times 10^{-13}\,\mathrm{cm}^2$ but slightly underestimates the experimental data at low fluences while overestimating them at high fluences. In contrast, the data are well represented by the modified model given in Eq. (3.8) using $A = 2.7 \times 10^{-13}\,\mathrm{cm}^2$ and $B = 2.4 \times 10^{-13}\,\mathrm{cm}^2$. The damage formation cross section is then only slightly lower than that of InP ($A = 3.2 \pm 0.2 \times 10^{-13}\,\mathrm{cm}^2$) while significant annealing (not present in InP) leads to the observed difference

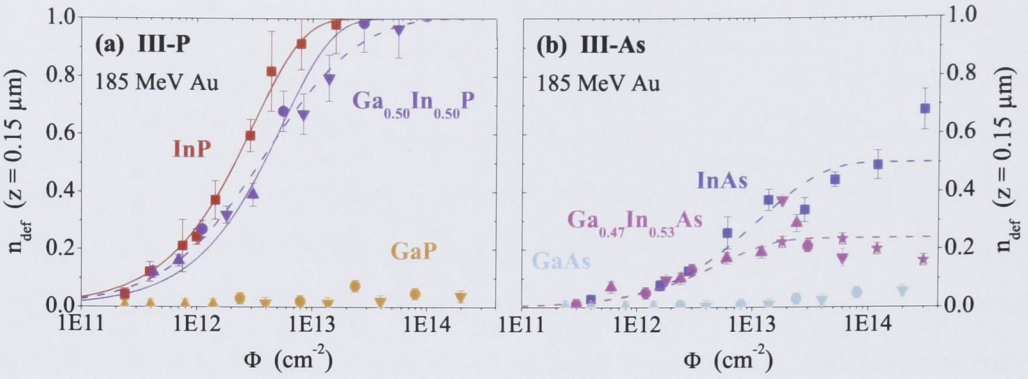

Figure 3.14: Defect concentration n_{def} at $z = 0.15\,\mu$m versus ion fluence Φ for (a) P and (b) As compounds. Different symbols correspond to different sample holders except for InP and InAs for which the averaged data points are plotted. Solid and dashed lines present fits with Gibbons model and the modified model, respectively.

in amorphization fluence.

At lower fluences, damage formation in $Ga_{0.47}In_{0.53}As$ (Fig. 3.14 (b)) is identical to that observed for InAs. For $\Phi > 2 \times 10^{13}\,\mathrm{cm}^{-2}$, however, the defect concentration clearly saturates at $n_{\mathrm{def}} \sim 0.2$. $Ga_{0.47}In_{0.53}As$ thus shows a behavior intermediate to that of InAs and GaAs. The saturation value may well be expected to depend on the stoichiometry of the ternary compound, decreasing with increasing Ga content. Similar to the case of InAs, the observed damage formation behavior cannot be described by the Gibbons model. The dashed magenta line in Fig. 3.14 (b) represents the modified model using $A = 5 \times 10^{-14}\,\mathrm{cm}^2$ and $B = 2 \times 10^{-13}\,\mathrm{cm}^2$. The damage formation cross section in $Ga_{0.47}In_{0.53}As$ is then the same as in InAs (with a similar uncertainty of $1 \times 10^{-14}\,\mathrm{cm}^2$) while the stronger annealing ($B = 2 \times 10^{-13}\,\mathrm{cm}^2$ compared to $B = 1 \times 10^{-13}\,\mathrm{cm}^2$, respectively) leads to a lower defect concentration at high fluences.

3.6.3 Track formation and damage annealing

Despite the simplicity of the modified model, it describes the different damage formation behaviors observed in the four In compounds rather well. Nevertheless, the physical processes operative under SHI irradiation and responsible for the strikingly different response of various III-V semiconductors remain elu-

sive. In principle, the very low defect concentration observed in GaP compared to InP, for example, can originate from two different effects: Either the SHIs do not create significant damage upon impact or damage is produced but then annealed immediately thereafter or during subsequent irradiation. A combination of material specific damage formation and annealing might be operative. All experimental techniques that have been applied so far study the irradiated material long after the ion energy has been dissipated and are thus not able to distinguish between the two possibilities.

Figure 3.8 shows that the energy deposited by the ion per unit path length is nearly identical for all four binary compounds. The question then is whether the same amount of deposited energy can have different effects depending on the properties of the material. Based on the Thermal Spike model, Szenes *et al.* compare the energy Q necessary to heat different semiconductors to their respective melting points, arguing that low Q values are advantageous for track formation [63]. Table 3.2 presents a similar comparison for the materials studied in this work together with Si and Ge. For both As and P compounds, Q increases with increasing Ga content (0, 0.5 or 1) which is mainly caused by the increase in melting point. For the same Ga content, Q is larger for the As compound than for the P compound due to the different densities. The trend in Q thus qualitatively agrees with the damage formation behavior. However, no quantitative predictions can be obtained from this approach. As discussed in Section 3.2, Kamarou *et al.* have simulated the maximum temperature inside the ion track for InP, Si and Ge based on a Thermal Spike model [53]. (No simulations have been performed for other III-V materials.) While the melting point is surpassed in InP over a wide range of Au energies, temperatures in Si and Ge stay far below their respective melting points. Without molten material that can be subsequently quenched into the amorphous phase, no significant damage is produced. In GaP and GaAs, the electronic energy loss may not be sufficient for melting and the small defect concentration observed may result from nuclear energy deposition as suggested by Wesch *et al.* [12]. If Coulomb Explosion and

	m_{III} (u)	m_V (u)	ρ (g/cm^3)	C_a (J/gK)	T_m (K)	Q (J/cm^3)	K_a (W/cmK)
InAs	114.8	74.9	5.67	0.35	1210	1820	0.23
$Ga_{0.47}In_{0.53}As$	92.3	74.9	5.50	0.34	1350 (*)	1980	
GaAs	69.7	74.9	5.32	0.33	1513	2140	0.51
InP	114.8	31.0	4.79	0.32	1335	1600	0.69
$Ga_{0.50}In_{0.50}P$	92.3	31.0	4.46	0.32	1530 (*)	1770	
GaP	69.7	31.0	4.13	0.31	1730	1840	0.75
Ge	72.6		5.33	0.33	1210	1610	0.59
Si	28.1		2.33	0.71	1687	2310	1.60

Table 3.2: Masses of the group III and group V constituents, m_{III} and m_V, respectively, density ρ, heat capacity of the atomic system C_a and melting point T_m. The energy required to heat a unit volume to the melting point is given by $Q = \rho C_a(T_m - T_{irr})$, where T_{irr} denotes the irradiation temperature. Also given is the thermal conductivity of the atomic system K_a. ρ, C_a and K_a are parameters at 300 K. All values are taken from [78,79] except for (*) that were calculated as the weighted average of the corresponding binary values.

weakening of bonds are used as track formation models (see Section 3.2), other material characteristics such as charge neutralization time, electron and hole mobility and energy levels of bonding and anti-bonding states must be considered. Again, given the complexity of the processes, no simple estimate is possible and no simulations have been performed so far.

For InAs, the experimental results demonstrate that significant damage is formed under SHI irradiation. A combination of damage production and annealing is proposed as a possible explanation for the slower increase of defect concentration with ion fluence compared to InP. Thermally stimulated solid phase epitaxial growth at the crystalline-amorphous interface in III-V semiconductors is operative much below the melting point [74]. At a fixed temperature, the growth rate for InAs is about four orders of magnitude larger than that for InP. Thus, the heat dissipated after the ion impact could lead to much greater annealing of damaged tracks in InAs relative to InP. However, the growth rates for InP and GaAs are very similar demonstrating that thermally induced epitax-

ial growth alone is insufficient to describe all the observed experimental results. Solid phase epitaxial recrystallization of amorphous clusters in III-V compounds is also stimulated by electron irradiation with energies well below the displacement energy [75]. Kamarou *et al.* found approximately 10 % of the free electrons created in InP by 185 MeV Au irradiation have energies of 1-2 keV [52]. Thus, annealing of damaged areas via solid phase epitaxial regrowth might also be stimulated by highly energetic electrons created during SHI irradiation.

3.7 Summary

The III-V binary compounds InP, InAs, GaP and GaAs and the related ternary alloys $Ga_{0.50}In_{0.50}P$ and $Ga_{0.47}In_{0.53}As$ were irradiated at room temperature with 185 MeV Au ions and fluences ranging from 2×10^{11} to $3 \times 10^{14}\,cm^{-2}$. The damage produced was assessed using TEM and RBS/c measurements. Despite the nearly identical energy loss values, the materials respond in a strikingly different manner. InP is amorphized readily under these irradiation conditions and a track radius of ~ 3 nm was obtained. InAs shows considerable damage although at much higher ion fluences compared to InP. GaP and GaAs remain almost undamaged even after irradiation with $2 \times 10^{14}\,cm^{-2}$. Regarding the ternaries, $Ga_{0.50}In_{0.50}P$ is amorphized at ion fluences only slightly higher than those required for InP and thus behaves very similarly to InP but not to GaP. In contrast, $Ga_{0.47}In_{0.53}As$ displays a damage formation behavior intermediate to that of InAs and GaAs. Based on the Gibbons overlap model, a combination of damage formation and annealing is proposed to describe the experimental findings. While the Gibbons model fits well for InP, the curve of $Ga_{0.50}In_{0.50}P$ is reproduced best with a modified model taking into account possible epitaxial regrowth during SHI irradiation. Assuming strong annealing, the modified model also describes the significantly lower damage levels in InAs and $Ga_{0.47}In_{0.53}As$. Nevertheless, the processes that govern the response of the various III-V semiconductors to SHI irradiation are not yet clear and other effects may also play a significant role.

Chapter 4

Atomic-scale structure of InP amorphized by ion irradiation

InP was amorphized by ion irradiation in two different regimes: 185 MeV Au irradiation where the energy loss is dominated by electronic interactions and Se irradiation with energies ranging from 80 keV to 7 MeV where nuclear stopping is dominant. The structural parameters of the amorphous phase were determined for as-irradiated and thermally relaxed samples. The amorphization mechanism operative in both regimes is identified.

4.1 Structure of amorphous semiconductors

Crystalline materials are characterized by well-defined short- and long-range order. Atoms that occupy equivalent sites of the crystal lattice are surrounded by the same local environment, that is by the same structural and chemical arrangements. In contrast, no long-range order exists in amorphous materials and similar atoms no longer all have the same environment. Bond length and bond angle distributions and mean coordination numbers are used to characterize the amorphous phase structure.

Continuous random network models with varying degrees of disorder (compared to the crystalline phase) have been introduced for covalently-bonded amorphous solids describing the structure in terms of topological rings [80–82]. For the diamond or zincblende crystal structure, all rings are even-membered

(sixfold) whereas the Polk model for the amorphous phase also includes odd-membered rings [81]. For a compound semiconductor such as InP this requires the presence of homopolar bonds which do not exist in the crystalline phase. Apart from the implications for structural models, the question whether such "wrong" bonds exist is of further interest due to their function as donor and acceptor states in the energy gap and the resulting influence on the electronic properties of the amorphous material [18]. Homopolar bonds in amorphous compound semiconductors have therefore been a major focus of many experimental studies. Using EXAFS spectroscopy, Theye *et al.* found indications for Ga-Ga bonds in flash evaporated amorphous GaP [83]. The same group later observed In-In bonds in flash evaporated amorphous InP, however, this material was highly non-stoichiometric [84]. The presence of homopolar bonds in stoichiometric material has since been confirmed (also by EXAFS spectroscopy) for InP [16] and InAs [17] amorphized by ion irradiation.

Different preparation techniques such as evaporation, sputtering and ion irradiation can yield different amorphous phase structures characterized by a free energy greater than that of the intrinsic, minimum-energy configuration [19]. Even with the same technique, differences in the experimental conditions can lead to different structural properties as demonstrated in an EXAFS study by Ridgway *et al.* [20]. The authors measured Ge samples amorphized by ion irradiation and found the structural parameters to depend on both irradiation fluence and temperature. Thus the question arises whether the fundamentally different energy deposition processes operative under ion irradiation in different energy regimes (see Section 3.1) yield different atomic structures of the amorphous phase. Gaiduk *et al.* have used cross-section TEM to compare the amorphous layer formed near the surface due to electronic stopping and near the end of the ion range due to nuclear stopping in InP irradiated with 250 MeV Xe [85]. Differences in the radial intensity of the diffraction patterns suggest different amorphous phase structures.

EXAFS is sensitive to subtle changes in the local atomic environment as

demonstrated by Ridgway *et al.* for amorphous Ge produced under different irradiation conditions (see above) [20]. The same group also studied Ge [21], InAs [22] and InP [19] amorphized by ion irradiation, comparing the structural parameters of as-irradiated and thermally-relaxed states. For all three materials, annealing at temperatures below the onset of recrystallization results in a structural relaxation of the amorphous phase towards the minimum-energy configuration.

Apart from experimental studies, the amorphous phase structure of a variety of materials has been predicted using molecular dynamics (MD) simulations. For InP, Lewis *et al.* have modeled the structure of the amorphous phase produced by rapid quenching from the liquid [86]. The system has an average coordination number slightly higher than the crystalline value of four and contains a significant percentage of homopolar bonds. Figure 4.1 (a) and (b) show ball-and-stick representations of crystalline and amorphous InP, respectively. Crystalline InP (c-InP) has the zincblende structure where every In atom is surrounded by four P atoms and each P atom is in turn bonded to four In atoms. This gives four unlike-atom first NNs, twelve like-atom second NNs and twelve unlike-atom third NNs. In amorphous InP (a-InP), long-range order is absent. Furthermore, atoms with coordination numbers other than four and like-atom bonding are clearly visible in Fig. 4.1 (b). The distributions of n-membered rings and total coordination numbers N are listed in Tables 4.1 and 4.2, respectively. Values for

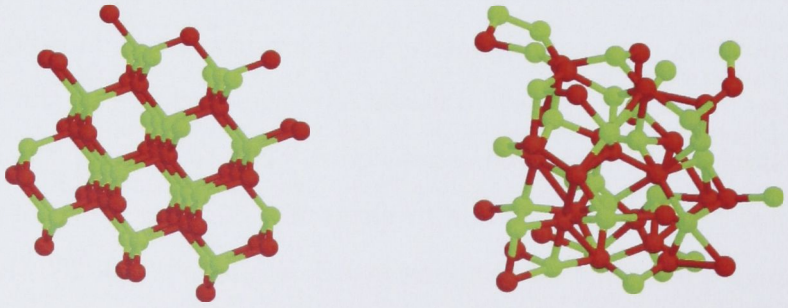

(a) Crystalline InP (b) Amorphous InP

Figure 4.1: Ball-and-stick representation of the atomic-scale structure in InP based on the calculations by Lewis *et al.* [86]. Images are taken from [87].

n	3	4	5	6	7
c-InP	0	0	0	4	0
a-InP	0.02	0.44	0.37	2.35	4.37

Table 4.1: Number of n-membered rings per atom for c-InP and a-InP (taken from [86]).

N	1	2	3	4	5	6	7
c-InP	0	0	0	100	0	0	0
a-InP	0	0	1.9	71.3	24.5	2.1	0

Table 4.2: Distribution (in %) of total coordination numbers N for c-InP and a-InP (taken from [86]).

ideal c-InP are also given. While the majority of atoms in the amorphous phase remain fourfold coordinated the material contains more seven-membered rings than six-membered rings in stark contrast to the crystalline phase.

4.2 Experimental details

4.2.1 Sample preparation

To prepare suitable EXAFS samples, the amorphized material of interest has to be separated from the bulk. Lattice-matched InP/$Ga_{0.47}In_{0.53}As$/InP heterostructures [2.75 μm/50 nm/(100) substrate] were grown by metal organic chemical vapor deposition. The InP epilayer was amorphized by ion irradiation with either dominant electronic (SHI sample) or dominant nuclear (LEI sample) energy loss and was isolated from the bulk using selective chemical etching. Figure 4.2 shows the different preparation steps for SHI and LEI samples.

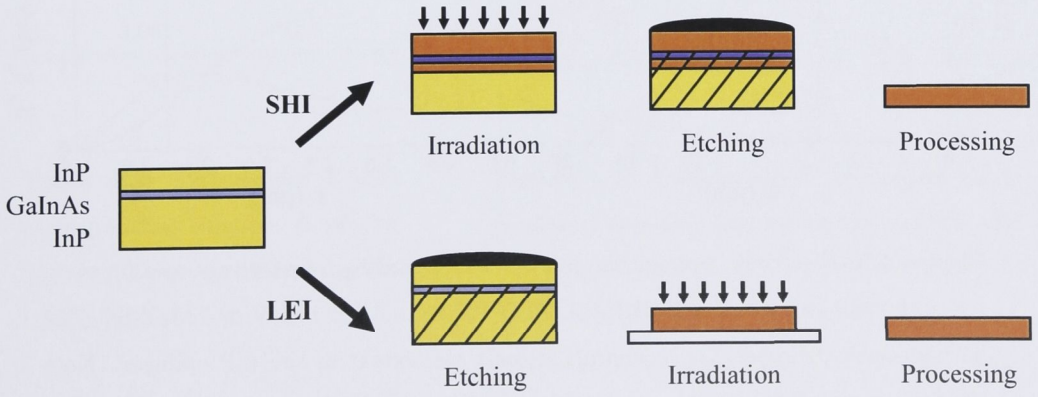

Figure 4.2: Schematic of the different preparation steps for SHI and LEI samples.

For the SHI sample, the heterostructures were irradiated at room temperature with 185 MeV Au ions (as described in Section 3.4) to a fluence of $3 \times 10^{13}\,\mathrm{cm}^{-2}$ which is safely beyond the fluence necessary for amorphization of InP. Figure 4.3 (a) plots the corresponding electronic and nuclear energy loss contributions, S_e and S_n, respectively, as a function of depth z. Electronic stopping is dominant over the entire depth of the InP epilayer and is well above the threshold value of $\sim 13\,\mathrm{keV\,nm}^{-1}$ for track formation. In contrast, nuclear stopping is negligible up to a depth of at least $\sim 5\,\mu\mathrm{m}$. As discussed in Section 3.2, amorphization of the InP epilayer under these irradiation conditions is due to electronic energy deposition. After irradiation (see Fig. 4.2) the heterostructures were masked with Apeizon black wax and the InP substrate was removed by etching in HCl(37%):H_2O (5:1) for ~ 80 min using the $Ga_{0.47}In_{0.53}As$ layer as a selective etch stop. The intermediate layer was then itself removed by etching in H_2SO_4(98%):H_2O_2(30%):H_2O (1:1:10) now using the InP epilayer as etch stop. After dissolving the wax the amorphized films were finely crushed and mixed with boron nitride to yield a homogeneous powder sample suitable for transmission EXAFS measurements.

As shown in Section 3.6.2, $Ga_{0.47}In_{0.53}As$ is only lightly damaged under ir-

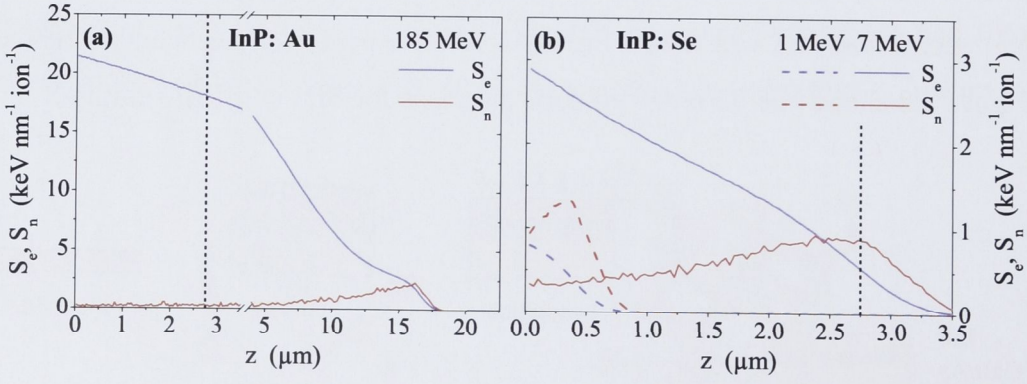

Figure 4.3: Electronic and nuclear energy loss, S_e and S_n, respectively, as a function of depth z for InP irradiated with (a) 185 MeV Au and (b) 1 MeV or 7 MeV Se. The dashed vertical line at $z = 2.75\,\mu\mathrm{m}$ indicates the extent of the InP epilayer. Note the break in depth scale in panel (a). Values were calculated using the SRIM2003 code [43].

radiation with 185 MeV Au ions thus maintaining reasonable selectivity in the etching process. In contrast, irradiation in the LEI regime produces significant damage and etching in HCl is no longer selective. For the LEI sample, the InP substrate and the $Ga_{0.47}In_{0.53}As$ layer were therefore removed by the same chemical processing described above but prior to irradiation (see Fig. 4.2). The isolated InP films, bonded to Si for support, were then amorphized at liquid nitrogen temperature by multiple Se irradiations with energies ranging from 80 keV to 7 MeV. Figure 4.3 (b) plots the electronic and nuclear energy loss, S_e and S_n, respectively, versus depth z for 1 MeV and 7 MeV Se. In this energy regime the electronic stopping is well below the track formation threshold and amorphization is caused by nuclear energy deposition. The fluences of the different Se irradiations were chosen to yield a constant value of total vacancy production over the entire InP epilayer. Table 4.3 lists all energy/fluence-combinations and Fig. 4.4 plots the total number of In and P vacancies V_{In+P} as a function of depth z for the various irradiations. The total irradiated fluence was $8.5 \times 10^{15}\,cm^{-2}$.

	E (MeV)	Φ ($10^{15}\,cm^{-2}$)
(1)	7.00	4.0
(2)	3.50	1.4
(3)	2.00	0.8
(4)	1.00	0.7
(5)	0.30	0.8
(6)	0.08	0.8

Table 4.3: Ion energies E and corresponding fluences Φ of the Se irradiations performed for the LEI sample.

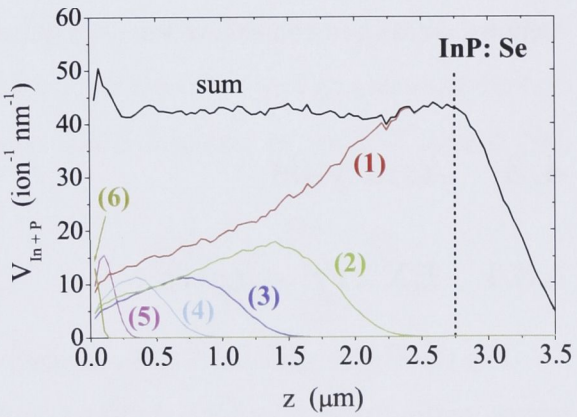

Figure 4.4: Total number of vacancies V_{In+P} produced as a function of depth z for the different Se irradiations. The curves are scaled according to the fluences given in Table 4.3 which also lists the corresponding ion energies. Values were calculated with the SRIM2003 code [43] using a displacement energy of $E_D = 8\,eV$ [52].

Similar to the irradiations in the SHI regime, the material was mounted on the sample holder with carbon paste to facilitate thermal contact while the areal power density was kept below $0.9\,\mathrm{W\,cm^{-2}}$. The amorphous nature of the material after irradiation was confirmed by RBS/c. A boron nitride diluted powder sample was prepared from the amorphized films as described above.

For a crystalline standard, a powdered c-InP sample was prepared by finely crushing a single-crystal InP wafer and mixing with boron nitride.

4.2.2 Measurement

EXAFS measurements of the In K-edge (27.940 keV) were performed in transmission mode using beam line NW10A at the Photon Factory, Japan. Depending on the sample, the height of the absorption edge $\Delta\mu t$ ranged from 0.08 to 0.45 making transmission the preferred detection mode. The measurement temperature was $\sim 20\,\mathrm{K}$ in order to minimize thermal vibrations of the atoms. After the measurement, the a-InP samples were annealed at 150°C for one hour to induce structural relaxation (see Section 4.1). The relaxed SHI and LEI samples were then remeasured at $\sim 20\,\mathrm{K}$.

4.3 Analysis

4.3.1 EXAFS spectra

The data were processed and analyzed using the IFEFFIT code [40] and the corresponding user interfaces ATHENA and ARTEMIS [41] as described in Section 2.4. Figure 4.5 (a) shows the k^3-weighted EXAFS signal as a function of photoelectron wave number k after background removal for c-InP and a-InP (SHI as-irradiated). FT was performed over a k-range of $k = 2 - 14\,\text{Å}$. The spectra for c-InP and a-InP (SHI as-irradiated) are plotted in Fig. 4.5 (b).

The EXAFS spectrum of the crystalline material shows a complex structure indicating the presence of several different frequencies. This is confirmed in the

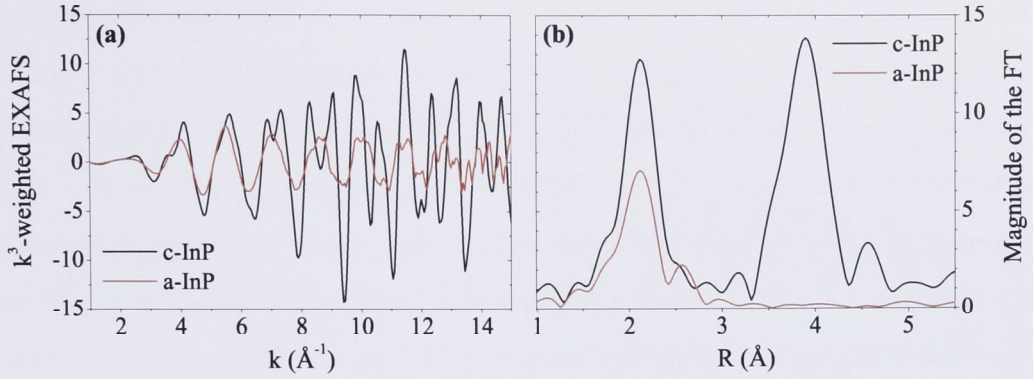

Figure 4.5: (a) k^3-weighted EXAFS spectra of c-InP and a-InP (SHI as-irradiated) versus the photoelectron wave number k. (b) FTs of the spectra shown in panel (a) as a function of the non-phase-corrected radial distance R from the absorber.

FT which contains three distinct peaks at $R \sim 2.1$ Å, $R \sim 3.9$ Å and $R \sim 4.6$ Å representing scattering from the first (P), second (In) and third (P) NNs, respectively. Figure 4.6 (a) shows a schematic of the absorbing In atom and its first and second NN shells. The EXAFS of the irradiated sample is dominated by a single frequency and only the first shell peak is observed in the FT. Structural disorder in amorphous materials is typically sufficient to prevent coherent scattering from beyond the first coordination shell. The absence of higher shell peaks in the spectrum is a characteristic feature of amorphous semiconductors and has been previously observed after ion irradiation in the LEI regime [88].

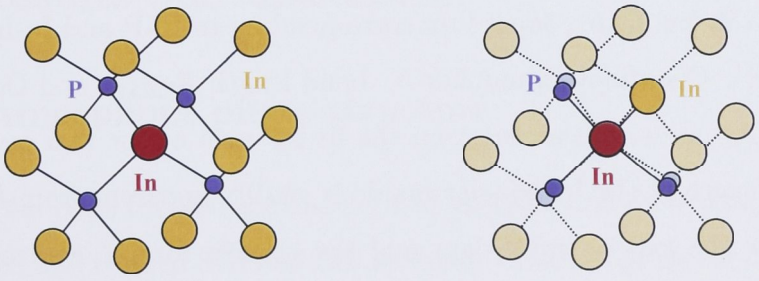

(a) c-InP (b) a-InP

Figure 4.6: Schematic of the atomic environment in InP showing the In absorber (red) and neighboring P and In atoms (blue and orange, respectively). The light-colored atoms in panel (b) indicate the atomic positions in the crystalline phase whereas the dark-colored atoms represent one possible first NN arrangement in a-InP.

The EXAFS measurements shown here are consistent with this behavior and confirm the formation of the amorphous phase after SHI irradiation as previously demonstrated by RBS/c, TEM and XRD [54, 60]. In addition to the reduction in amplitude of the first NN P peak, a small second peak at $R \sim 2.6$ Å is apparent in Fig. 4.5 (b) resulting from In atoms present in the first NN shell of the amorphous material. Similar findings were reported by Glover *et al.* [16] and Azevedo *et al.* [19] for amorphization in the LEI regime. Figure 4.6 (b) shows a schematic of one possible first NN environment in the amorphous phase.

4.3.2 Fitting

For the analysis only the first NN shell was considered. Fitting was performed in radial space over a range of $R = 1.5 - 2.9$ Å while applying multiple k-weights $= 2, 3, 4$. Scattering amplitudes and phase shifts were calculated *ab initio* with the FEFF8 code [36]. The amplitude reduction factor S_0^2 and the threshold energy E_0 were determined from the crystalline standard and were fixed while fitting the spectra of the amorphous samples. For c-InP, the bond length R_{EXAFS} and Debye-Waller factor $\sigma^2_{\mathrm{EXAFS}}$ of the first NN P path were floated while the coordination number N was fixed to the crystalline zincblende value of four (see Fig. 4.6 (a)). Figure 4.7 (a) shows the back-transformed experimental data together with the best fit. For a-InP, two scattering paths must be included in the fitting procedure corresponding to In-P and In-In pairs (see Fig. 4.6 (b)). Coordination number N, bond length R_{EXAFS} and Debye-Waller factor $\sigma^2_{\mathrm{EXAFS}}$ were determined from the fit for each of the two contributions. The significance of the homopolar bonds is readily apparent from Fig. 4.7 (b) which plots the experimental data and the best fit for the as-irradiated SHI sample in R-space. Also shown are the two individual scattering contributions arising from P and In atoms in the first NN shell. Figure 4.7 (c) plots the back-transformed experimental data and best fits for all a-InP samples.

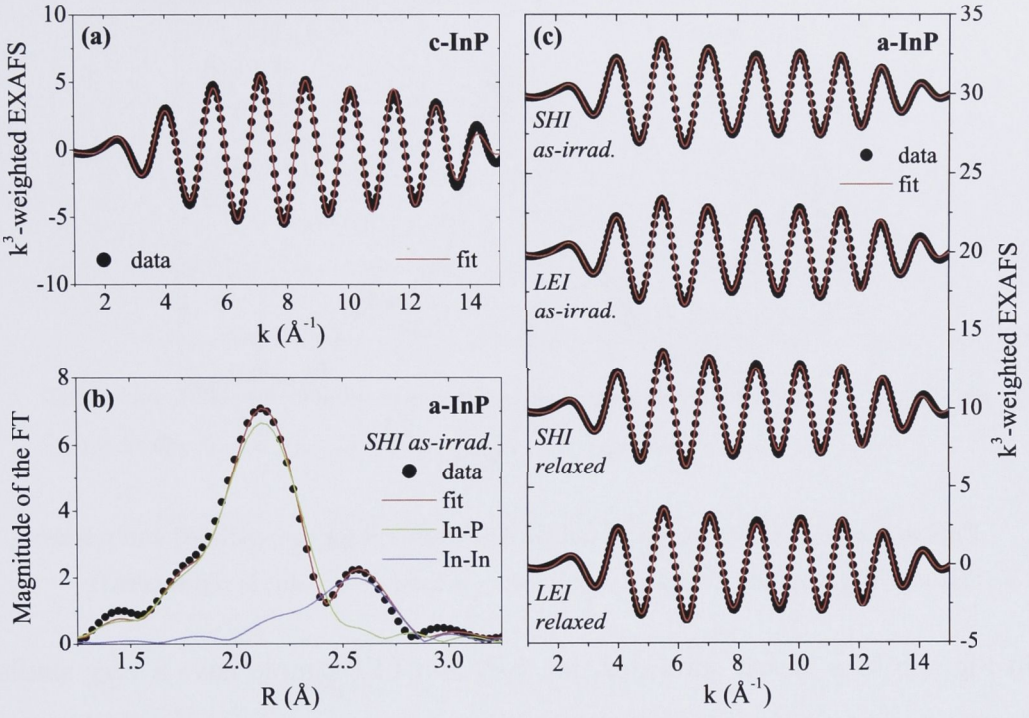

Figure 4.7: (a) k^3-weighted back-transformed experimental data and best fit versus k for c-InP. (b) FT of the experimental EXAFS and best fit as a function of R for a-InP (SHI as-irradiated). Also plotted are the two scattering contributions arising from In-P and In-In pairs. (c) k^3-weighted back-transformed experimental data and best fits versus k for as-irradiated and relaxed SHI and LEI samples. Graphs for different samples are offset for clarity.

4.4 Results and discussion

4.4.1 Amorphous phase structure

Figure 4.8 plots the Fourier transformed experimental data versus R for the as-irradiated and relaxed SHI and LEI samples. Clearly, the spectra for the two samples amorphized in the different energy regimes are very similar both before and after relaxation. The relaxed samples are characterized by an increase in amplitude of the P peak while the overall features of the amorphous phase are retained. All four spectra exhibit the smaller second peak at $R \sim 2.6\,\text{Å}$ associated with In-In bonds (see Fig. 4.7 (b)). The experimental data plotted

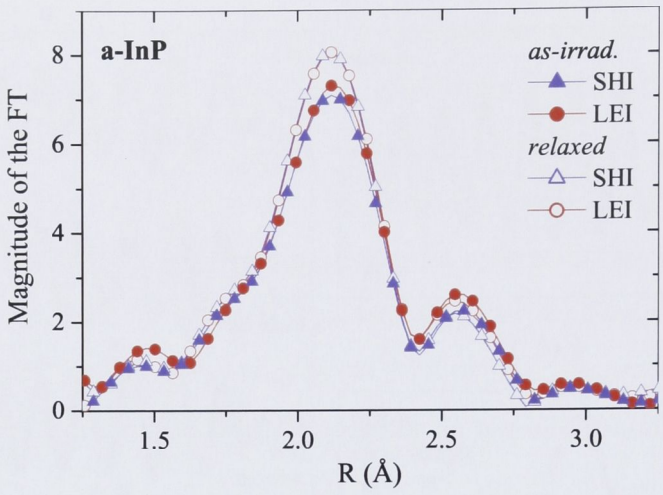

Figure 4.8: FTs of the experimental EXAFS versus R for as-irradiated and relaxed SHI and LEI samples. For clarity, only every second data point is represented.

in Fig. 4.8 thus clearly indicates that SHI and LEI sample have a very similar structure despite the fundamentally different energy regimes in which amorphization took place. The coordination number N, bond length R_{EXAFS} and Debye-Waller factor $\sigma^2_{\mathrm{EXAFS}}$ determined from the best fits to the experimental data are summarized in Table 4.4 and Table 4.5 for first NN P and first NN In atoms, respectively. The values are plotted in Fig. 4.9.

Comparing the as-irradiated and crystalline material, amorphization yields a decrease in heteropolar coordination number and an increase in bond length and Debye-Waller factor. The reduction in amplitude for the first NN P peak observed in Fig. 4.5 (b) is thus not only due to the increased disorder of the amorphous phase but also due to a reduced In-P coordination. Total coordination number N_{tot} and percentage of In-In bonds $\%_{\mathrm{In\text{-}In}}$ are listed in Table 4.6. N_{tot} is slightly higher than the crystalline value for all amorphous samples in good agreement with the predictions by Lewis *et al.* [86]. The fraction of homopolar bonds amounts to $\sim 15\%$. The In-In bond length is found to be significantly larger than the In-P distance (~ 2.78 Å versus ~ 2.58 Å) in agreement with the difference in covalent radii (~ 1.13 Å for P and ~ 1.41 Å for In [89]). These findings are very similar to the behavior previously observed after irradiation in the LEI regime [16, 19].

1^{st} NN In-P		N	R_{EXAFS} (Å)	$\sigma^2_{\mathrm{EXAFS}}$ (10^{-3} Å^2)
c-InP		4	2.542 ± 0.003	2.3 ± 0.2
a-InP SHI	as-irrad.	3.43 ± 0.26	2.575 ± 0.003	5.5 ± 0.8
	relaxed	3.54 ± 0.27	2.569 ± 0.004	4.8 ± 0.7
a-InP LEI	as-irrad.	3.47 ± 0.30	2.576 ± 0.004	5.5 ± 1.0
	relaxed	3.57 ± 0.23	2.570 ± 0.003	5.0 ± 0.6

Table 4.4: The 1^{st} NN In-P coordination number N, bond length R_{EXAFS} and Debye-Waller factor $\sigma^2_{\mathrm{EXAFS}}$ obtained from the best fits for c-InP and a-InP.

1^{st} NN In-In		N	R_{EXAFS} (Å)	$\sigma^2_{\mathrm{EXAFS}}$ (10^{-3} Å^2)
a-InP SHI	as-irrad.	0.70 ± 0.27	2.783 ± 0.009	5.8 ± 2.1
	relaxed	0.66 ± 0.15	2.767 ± 0.013	5.8 *fixed*
a-InP LEI	as-irrad.	0.63 ± 0.27	2.782 ± 0.008	4.4 ± 2.2
	relaxed	0.57 ± 0.10	2.771 ± 0.008	4.4 *fixed*

Table 4.5: The 1^{st} NN In-In coordination number N, bond length R_{EXAFS} and Debye-Waller factor $\sigma^2_{\mathrm{EXAFS}}$ obtained from the best fits for a-InP.

Relaxation of the amorphous phase leads to a small increase in heteropolar coordination number while the In-P Debye-Waller factor decreases slightly (see Table 4.4), both contributing to the increased amplitude of the P peak observed in Fig. 4.8. Due to the strong correlation between N and $\sigma^2_{\mathrm{EXAFS}}$, the In-In Debye-Waller factor has been fixed to the as-irradiated value while fitting the relaxed spectra following the analysis of Azevedo *et al.* [19]. This yields a small reduction of the homopolar coordination number upon relaxation (see Table 4.4). Nevertheless, a significant percentage of In-In bonds remains in the relaxed samples for both energy regimes (see Table 4.6) and thus confirms that chemical disorder is a characteristic feature of amorphous InP and most likely the III-V semiconductors in general. The In-P and In-In bond lengths are smaller in the relaxed samples compared to the as-irradiated values. In summary, relaxation yields a small change of the structural parameters towards

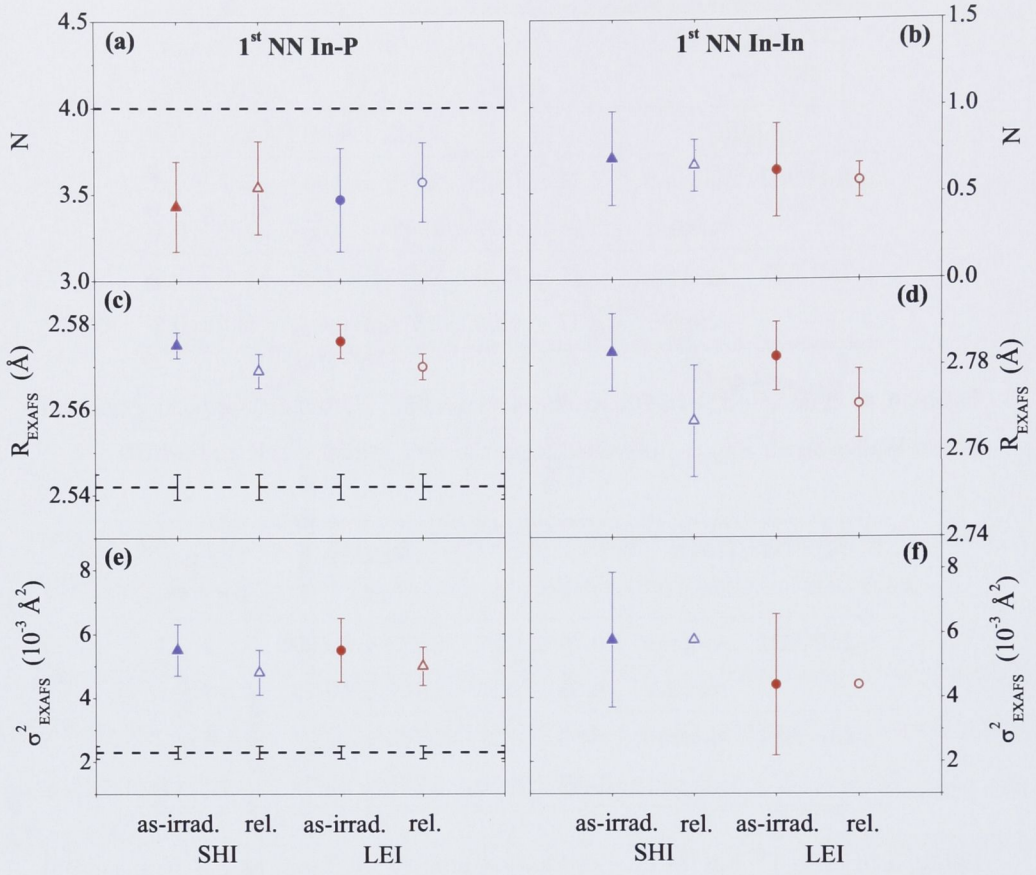

Figure 4.9: 1^{st} NN structural parameters obtained for as-irradiated and relaxed (full and open symbols, respectively) SHI and LEI samples (blue triangles and red circles, respectively). Plotted are the coordination number N, bond length R_{EXAFS} and Debye-Waller factor $\sigma^2_{\mathrm{EXAFS}}$ for In-P and In-In pairs as given in Table 4.4. The dashed lines in panel (a), (c) and (e) represent the values obtained for c-InP.

those of crystalline material, consistent with previous findings for samples amorphized in the LEI regime [19].

Note that the relaxation temperature is well below that required for recrystallization [19]. Relaxation therefore yields a small change in the amorphous phase structure reducing disorder but not inducing recrystallization. The ability to measure such changes (see Fig. 4.8) demonstrates the sensitivity of the EXAFS technique. No significant difference is observed when comparing the In-P contribution of the SHI sample with that of the LEI sample. Comparing the In-In contributions, a small difference is apparent in the amplitude of the peak.

		N_{tot}	$\%_{In\text{-}In}$
c-InP		4	
a-InP SHI	as-irrad.	4.13 ± 0.53	17 %
	relaxed	4.20 ± 0.42	16 %
a-InP LEI	as-irrad.	4.10 ± 0.57	15 %
	relaxed	4.14 ± 0.33	14 %

Table 4.6: Total coordination number N_{tot} and percentage of In-In bonds $\%_{In\text{-}In}$ for the various a-InP samples.

Though this difference is stable under various fitting conditions, the magnitude of the experimental uncertainty does not allow an unambiguous assignment of its physical origin. It is therefore concluded that amorphization in both energy regimes leads to a similar amorphous phase structure despite the fundamentally different energy transfer mechanisms. This is clearly in contrast to the results reported by Gaiduk *et al.* [85]. However, while in this work the LEI sample was produced by ion irradiation in the keV and low MeV region, Gaiduk *et al.* have studied the amorphous layer formed due to nuclear energy deposition at the end of range under SHI irradiation. EXAFS and TEM may also be sensitive to different aspects of the amorphous short-range order. Without relating the TEM measurements to structural parameters of the atomic environment, a comparison of the two studies is difficult. Application of a complimentary technique, such as Raman spectroscopy [90], may provide additional structural information and thus aid in the understanding of the amorphous phase structure of InP.

4.4.2 Amorphization mechanism

Ion irradiation processes are non-equilibrium in nature and different models have been proposed to account for experimental findings (see Section 3.1). For the SHI regime, Kamarou *et al.* have recently applied a Thermal Spike model to predict the irradiation conditions necessary to produce amorphous tracks in InP and good agreement with experimental data was obtained [52]. The Thermal Spike model assumes that electronic energy deposition above a certain threshold

leads to melting of the material along the ion trajectory which, in the present case, is subsequently quenched into the amorphous phase during rapid resolidification [51]. The SHI irradiation conditions used in this work fall within the energy range where the calculated maximum temperature inside the track exceeds the melting point and a "melt and quench" process is expected (see Section 3.2) [52].

Damage production in the LEI regime is usually associated with collision cascades and the formation, accumulation and growth of various types of defects [45, 47, 48]. Studies of InP irradiated under conditions very similar to those of the LEI sample in this work demonstrate that a direct amorphization process is operative, where amorphous material is produced within a single ion impact [10,91]. Nordlund *et al.* have investigated the amorphization mechanism during LEI irradiation using MD simulations. For both Ge [92] and GaAs [93] they report that recoils of several keV lead to molten regions in the material which subsequently form amorphous pockets upon cooling. In contrast, collision cascades in Si are less dense and hence less damage with a higher fraction of isolated defects results [92]. Figures 4.10 and 4.11 show the simulation cell with (a) the liquid-like atoms in the keV collision cascade and (b) the final defects after cascade quenching for Ge and Si, respectively (taken from [92]). The authors argue that crystal structure, melting point and mass are the relevant properties that determine the damage formation behavior. The crystal struc-

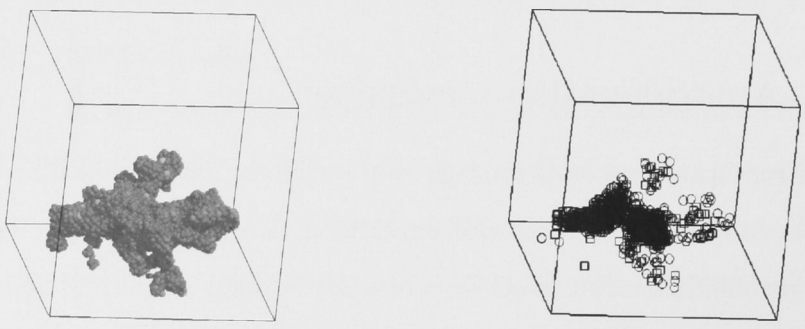

(a) Liquid-like atoms in the cascade (b) Final defects after cooling

Figure 4.10: MD simulations of keV collision cascades in Ge (taken from [92]).

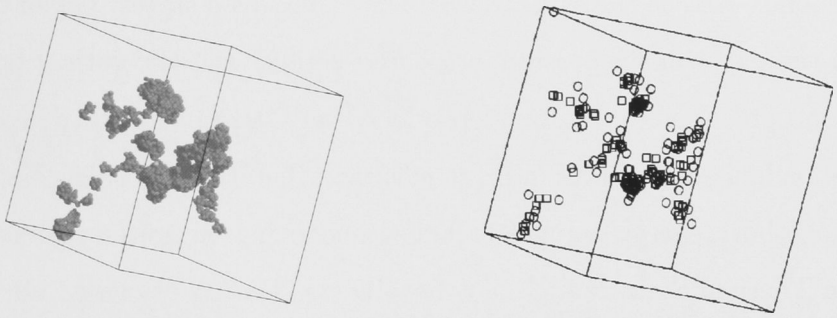

(a) Liquid-like atoms in the cascade (b) Final defects after cooling

Figure 4.11: MD simulations of keV collision cascades in Si (taken from [92]).

ture is very similar for all materials considered here (diamond structure for Ge and Si, zincblende structure for GaAs and InP). Melting point T_m and average mass per atom $\bar{m}$ are listed in Table 4.7. Comparing the values, it can be assumed that InP behaves similarly to Ge and GaAs. Following this argument and supported by the direct amorphization observed experimentally, a "melt and quench" process is expected for the LEI irradiation conditions applied in this work.

Thus, independent of the energy transfer mechanism, amorphization in both energy regimes proceeds via a similar process. As a consequence, SHI and LEI samples have a nearly identical atomic structure. As mentioned in Section 4.1, amorphization of InP by quenching from the liquid has been modeled with MD simulations by Lewis *et al.* [86]. Homopolar bonds are present in the liquid phase and are retained (8% of all bonds) after quenching into the amorphous phase. The authors conclude that the presence of chemical disorder is necessary to stabilize the amorphous phase. SHI and LEI samples contain a significant fraction

	Ge	GaAs	InP	Si
T_m (K)	1210	1513	1335	1687
$\bar{m}$ (u)	73	72	73	28

Table 4.7: Melting point T_m and average mass per atom $\bar{m}$ for Ge, GaAs, InP and Si. Values are taken from [79].

of In-In bonds in both the as-irradiated and the relaxed states. Given the agreement of the experimental results presented herein with theoretical predictions of the amorphous phase structure produced by a quench from the melt, these findings could be viewed as indirect evidence that the amorphization process common to both energy regimes is indeed quenching of molten regions. In line with the Thermal Spike model and the MD simulations discussed above, these molten regions are formed due to the energy loss of the incoming ions, either via electronic stopping for the SHI case or nuclear stopping for the LEI case.

4.5 Summary

InP has been amorphized by ion irradiation with either dominant electronic energy loss (SHI regime, 185 MeV Au ions) or dominant nuclear energy loss (LEI regime, Se ions with energies ranging from 80 keV to 7 MeV). Samples suitable for transmission EXAFS measurements were prepared using a combination of semiconductor processing techniques and selective chemical etching. Structural parameters of the as-irradiated and relaxed samples were obtained from the experimental data collected at ~ 20 K. The structural changes observed for crystalline versus amorphous and as-irradiated versus relaxed phase are similar to the findings previously reported for amorphization in the LEI regime. Furthermore, no significant difference in the atomic structure of the two samples amorphized in the different energy regimes was apparent. This suggests amorphization to take place via a common process despite the fundamentally different energy transfer mechanisms. For the irradiation conditions used in this work, the Thermal Spike model (SHI regime) and MD simulations for collision cascades (LEI regime) predict amorphization to proceed via a quench from the melt. Thus, independent of the transfer mechanism, the energy deposited into the system leads to a molten region in both regimes which is subsequently quenched into the amorphous phase.

Chapter 5

Vibrational anisotropy in crystalline and amorphous InP

The structural parameters of crystalline and amorphous InP were determined with EXAFS as a function of measurement temperature ranging from 20 to 295 K. Mean square relative displacements for first, second and third NN shells are compared to the uncorrelated mean square displacements determined from XRD measurements. Results are discussed in terms of the energy required for different types of atomic motion such as bond stretching and bond bending.

5.1 Temperature-dependent EXAFS theory

5.1.1 Cumulants and three-dimensional motion

In a perfect single crystal, static disorder can be assumed negligible, however, thermally induced vibrations cannot be neglected even at very low temperatures due to zero-point motion [23]. Figure 5.1 schematically shows the sites of absorber and backscatterer atoms in a state of absolute rest connected by $\mathbf{R}_0$ and surrounded by the ellipsoids defining their thermal motion. $\mathbf{u}_0$ and $\mathbf{u}_j$ denote the instantaneous displacement vectors of absorber and backscatterer, respectively. The interatomic distance vector $\mathbf{R}$ can thus be expressed as [94]

$$\mathbf{R} = \mathbf{R}_0 + \mathbf{u}_j - \mathbf{u}_0 = \mathbf{R}_0 + \Delta\mathbf{u} \qquad \text{with} \qquad \Delta\mathbf{u} = \mathbf{u}_j - \mathbf{u}_0. \tag{5.1}$$

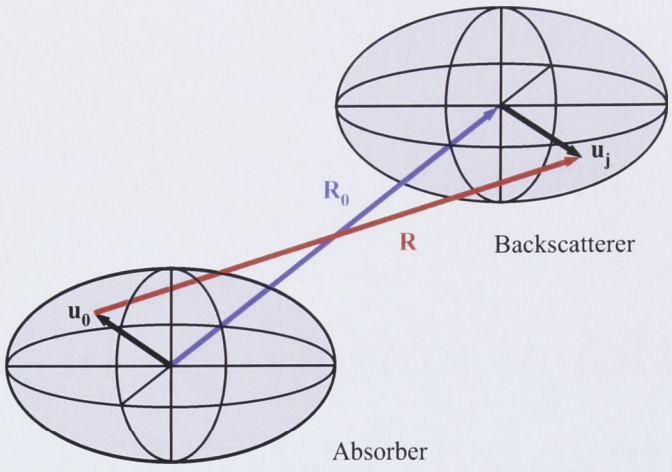

Figure 5.1: Ellipsoids defining the thermal motion of absorber and backscatterer atoms and their instantaneous displacement vectors, $\mathbf{u}_0$ and $\mathbf{u}_j$, respectively. The ideal positions of absolute rest, given by the centers of the ellipsoids, are connected by $\mathbf{R}_0$ while the actual instantaneous positions are connected by $\mathbf{R}$.

Defining $\hat{\mathbf{R}}$ as the unit vector along the line connecting the atomic pair, $\mathbf{R}_0 = R_0\hat{\mathbf{R}}$, the parallel and perpendicular components of the displacement vectors follow from

$$\begin{aligned} \Delta u_{\parallel} &= \Delta\mathbf{u}\cdot\hat{\mathbf{R}} = (\mathbf{u}_j - \mathbf{u}_0)\cdot\hat{\mathbf{R}} = u_{j,\parallel} - u_{0,\parallel} \\ \Delta u^2 &= \Delta u_{\parallel}^2 + \Delta u_{\perp}^2 = (u_{j,\parallel} - u_{0,\parallel})^2 + (u_{j,\perp} - u_{0,\perp})^2. \end{aligned} \tag{5.2}$$

They are illustrated in Fig. 5.2 (a). The instantaneous interatomic distance R can thus be written as

$$\begin{aligned} R &= \left[(R_0 + \Delta u_{\parallel})^2 + \Delta u_{\perp}^2\right]^{1/2} \\ &= \left[R_0^2 + 2R_0\Delta u_{\parallel} + \Delta u_{\parallel}^2 + \Delta u_{\perp}^2\right]^{1/2} \\ &= R_0\left[1 + \frac{2\Delta u_{\parallel}}{R_0} + \frac{\Delta u_{\parallel}^2}{R_0^2} + \frac{\Delta u_{\perp}^2}{R_0^2}\right]^{1/2}. \end{aligned} \tag{5.3}$$

For small displacements, $\Delta u \ll R_0$, Eq. (5.3) can be developed into a Taylor series [23, 94]

$$\begin{aligned} R &= R_0\left[1 + \frac{\Delta u_{\parallel}}{R_0} + \frac{\Delta u_{\perp}^2}{2R_0^2} + O(3)\right] \\ &= R_0 + \Delta u_{\parallel} + \frac{\Delta u_{\perp}^2}{2R_0} + O(3) \end{aligned} \tag{5.4}$$

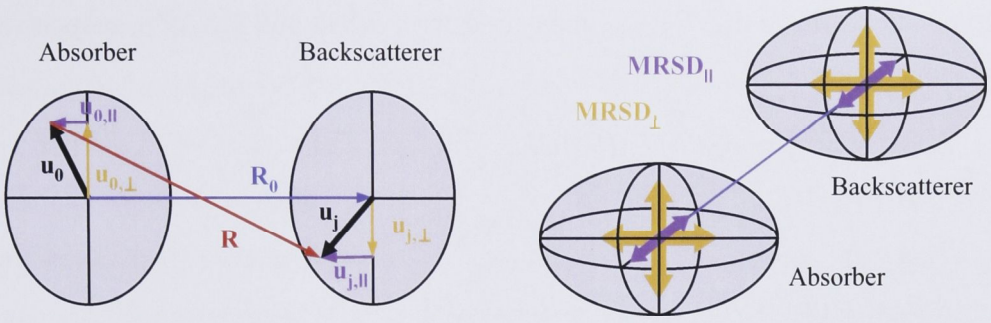

(a) Displacement vectors (b) Thermal vibrations

Figure 5.2: Parallel $\parallel$ and perpendicular $\perp$ components of the atomic motion with respect to the vector connecting the centers of the ellipsoids $\mathbf{R}_0 = R_0\hat{\mathbf{R}}$.

where $O(3)$ denotes all terms of order three or above. In Section 2.2.3, the EXAFS was parameterized in terms of the cumulants C_n of the one-dimensional distance distribution $\rho(R)$. Using Eqs (2.15) and (5.4) the cumulants can now be related to the three-dimensional atomic motion [23,25,94,95]. The first cumulant equals

$$R_{\mathrm{EXAFS}} = C_1 = \langle R \rangle = R_0 + \langle \Delta u_\parallel \rangle + \frac{\langle \Delta u_\perp^2 \rangle}{2R_0} + O(3). \tag{5.5}$$

For a harmonic crystal, where the potential energy is proportional to $(R - R_0)^2$, the average over $\Delta u_\parallel$ is zero. For a real, anharmonic crystal, $\Delta u_\parallel$ can be split into harmonic and anharmonic contributions, $\Delta u_\parallel = \Delta u_\parallel^{\mathrm{harm}} + \Delta u_\parallel^{\mathrm{anharm}}$ [23]. Neglecting the third order terms, Eq. (5.5) thus becomes

$$\begin{aligned} R_{\mathrm{EXAFS}} &= R_0 + \langle \Delta u_\parallel^{\mathrm{anharm}} \rangle + \frac{\langle \Delta u_\perp^2 \rangle}{2R_0} \\ &= R_{\mathrm{C}} + \frac{\langle \Delta u_\perp^2 \rangle}{2R_0}. \end{aligned} \tag{5.6}$$

In contrast to EXAFS which measures the average over the instantaneous interatomic distances (see Eq. (5.5)), XRD detects the distance between the average atomic positions, which is R_0 for harmonic crystals and $R_0 + \langle \Delta u_\parallel^{\mathrm{anharm}} \rangle$ for anharmonic crystals. R_{C} thus corresponds to the crystallographic distance obtained from XRD. R_{EXAFS} is larger than R_{C} due to relative vibrations perpendicular to the line connecting the absorber-backscatterer pair [23]. The thermal

expansions ΔR_{C} and $\Delta R_{\mathrm{EXAFS}}$ measured with XRD and EXAFS, respectively, are given by

$$\begin{aligned}
\Delta R_{\mathrm{C}}(T) &= R_{\mathrm{C}}(T) - R_{\mathrm{C}}(0\,\mathrm{K}) \\
&= \langle \Delta u_{\parallel}^{\mathrm{anharm}} \rangle(T) - \langle \Delta u_{\parallel}^{\mathrm{anharm}} \rangle(0\,\mathrm{K}) \\
\Delta R_{\mathrm{EXAFS}}(T) &= R_{\mathrm{EXAFS}}(T) - R_{\mathrm{EXAFS}}(0\,\mathrm{K}) \\
&= \Delta R_{\mathrm{C}}(T) + [\langle \Delta u_{\perp}^2 \rangle(T) - \langle \Delta u_{\perp}^2 \rangle(0\,\mathrm{K})]/2R_0
\end{aligned} \tag{5.7}$$

where T denotes the temperature. Since $\langle \Delta u_{\perp}^2 \rangle$ increases with temperature, $\Delta R_{\mathrm{EXAFS}}$ is larger than ΔR_{C}. Hence the thermal expansion measured by EXAFS is larger than that determined by XRD [23].

For the second cumulant, Eqs (2.15) and (5.4) yield

$$\begin{aligned}
\sigma^2_{\mathrm{EXAFS}} = C_2 &= \langle (R - R_{\mathrm{EXAFS}})^2 \rangle \\
&= \langle R^2 \rangle - R^2_{\mathrm{EXAFS}} \\
&= \langle \Delta u_{\parallel}^2 \rangle - \langle \Delta u_{\parallel} \rangle^2 + O(3).
\end{aligned} \tag{5.8}$$

An expression that also includes the leading higher order terms is given in [23, 95]. The error due to neglecting these higher order terms is usually smaller than 1% [95]. Furthermore, $\langle \Delta u_{\parallel} \rangle^2 = 0$ only for harmonic crystals whereas $\langle \Delta u_{\parallel} \rangle^2 = \langle \Delta u_{\parallel}^{\mathrm{anharm}} \rangle^2$ for anharmonic crystals. Nevertheless, this contribution is typically neglected and the EXAFS Debye-Waller factor becomes [23,25,94,95]

$$\begin{aligned}
\sigma^2_{\mathrm{EXAFS}} &= \langle \Delta u_{\parallel}^2 \rangle \\
&= \langle (u_{j,\parallel} - u_{0,\parallel})^2 \rangle \\
&= \langle u_{j,\parallel}^2 \rangle + \langle u_{0,\parallel}^2 \rangle - 2 \langle u_{j,\parallel} u_{0,\parallel} \rangle .
\end{aligned} \tag{5.9}$$

The first two terms of the last line, $\langle u_{j,\parallel}^2 \rangle$ and $\langle u_{0,\parallel}^2 \rangle$, correspond to the *uncorrelated* mean square displacement (MSD) of backscatterer and absorber, respectively, projected onto the line connecting the atomic pair [94, 96]. The one-dimensional MSD is connected to the XRD Debye-Waller factor B by [97]

$$\mathrm{MSD} = \frac{B}{8\pi^2}. \tag{5.10}$$

The last term in Eq. (5.9), $\langle u_{j,\parallel} u_{0,\parallel} \rangle$, represents the displacement correlation function and depends on the *correlated* motion of absorber-backscatterer pair [94, 96]. The EXAFS Debye-Waller factor, $\sigma^2_{\mathrm{EXAFS}} = \langle (u_{j,\parallel} - u_{0,\parallel})^2 \rangle$, thus corresponds to the *parallel* mean square relative displacement ($\mathrm{MSRD}_\parallel$) and is a measure for the vibrations of absorber and backscatterer relative to each other along the line connecting the atomic pair. The situation is shown schematically in Fig. 5.2 (b). Assuming the atoms to move either perfectly in phase or perfectly out of phase, lower and upper limits for $\sigma^2_{\mathrm{EXAFS}}$ can be estimated [98]

$$\mathrm{MSD}_{0+j} - 2\sqrt{\mathrm{MSD}_0 \mathrm{MSD}_j} \leq \sigma^2_{\mathrm{EXAFS}} \leq \mathrm{MSD}_{0+j} + 2\sqrt{\mathrm{MSD}_0 \mathrm{MSD}_j} \tag{5.11}$$

where $\mathrm{MSD}_{0+j} = \mathrm{MSD}_0 + \mathrm{MSD}_j$ is the sum of absorber and backscatterer MSD. Similar to $\mathrm{MSRD}_\parallel$, the MSRD *perpendicular* to the line connecting the atomic pair ($\mathrm{MSRD}_\perp$, see Fig. 5.2 (b)) is defined by

$$\begin{aligned} \mathrm{MSRD}_\perp &= \left\langle \Delta u_\perp^2 \right\rangle \\ &= \left\langle (u_{j,\perp} - u_{0,\perp})^2 \right\rangle \\ &= \left\langle u_{j,\perp}^2 \right\rangle + \left\langle u_{0,\perp}^2 \right\rangle - 2 \left\langle u_{j,\perp} u_{0,\perp} \right\rangle . \end{aligned} \tag{5.12}$$

If the thermal vibrations of the atoms are isotropic, the thermal ellipsoids in Figs 5.1 and 5.2 become spheres and the limits for $\mathrm{MSRD}_\perp$ are found to be

$$\mathrm{MSD}_{0+j} - 2\sqrt{\mathrm{MSD}_0 \mathrm{MSD}_j} \leq \frac{\mathrm{MSRD}_\perp}{2} \leq \mathrm{MSD}_{0+j} + 2\sqrt{\mathrm{MSD}_0 \mathrm{MSD}_j}. \tag{5.13}$$

The factor of $\frac{1}{2}$ compared to Eq. (5.11) stems from the fact that the perpendicular component of the atomic motion is the projection onto a plane while the parallel component and the MSD are projections onto a line. The ratio γ between $\mathrm{MSRD}_\perp$ and $\mathrm{MSRD}_\parallel$ depends on the correlation of the atomic motion both along the line connecting the atomic pair and perpendicular to it. For isotropic MSRDs, $\gamma = 2$, however, the ratio may have a different value, even if the thermal vibrations are isotropic, due to different parallel and perpendicular displacement correlation functions. Inserting Eq. (5.12) into Eq. (5.6) yields

$$\mathrm{MSRD}_\perp = 2R_0(R_{\mathrm{EXAFS}} - R_{\mathrm{C}}). \tag{5.14}$$

Thus the $\mathrm{MSRD}_{\perp}$ can be determined by comparing the average interatomic distances measured with EXAFS and XRD.

A discussion of the various terms comprising the third cumulant C_3 is given in [23, 95]. In principle, the angular averaging over $\rho(\mathbf{R})$, vibrations perpendicular to the line connecting the atomic pair and $\Delta u_{\parallel}^{\mathrm{anharm}}$ all contribute to the asymmetry of the one-dimensional distance distribution sampled with EXAFS. Fornasini *et al.* have shown, however, that C_3 is mainly due to the anharmonicity of the crystal potential while the other contributions are negligible [23, 95].

5.1.2 Debye and Einstein models

Many physical properties, most prominently the heat capacity, depend on the vibrational behavior of the atoms. Considering a simple model such as a one-dimensional, periodic chain of atoms, two different types of vibrations can be distinguished for non-Bravais crystals (systems with a unit cell that contains more than one atom) [99]. For small frequencies, *acoustic* modes are characterized by a linear dispersion relation, $\omega \sim cq$, where ω denotes the phonon frequency, q stands for the wave number and c is the phase velocity. *Optical* modes display a dispersion curve much flatter than that of the acoustic modes and often the frequency can be approximated by a constant, $\omega \sim \omega_0$, particularly for q close to zero. The same distinction between acoustic and optical branches can be made when considering three-dimensional crystals.

Based on the characteristics of acoustic and optical modes for small q, two models, the *Debye* model and the *Einstein* model, have been proposed [99]. The Debye model approximates the dispersion relation by the behavior of the acoustic branches and assumes $\omega = cq$. The Einstein model uses a constant frequency $\omega = \omega_{\mathrm{E}}$ and thus approximates the dispersion relation by the behavior of the optical modes. Knowing $\omega(q)$, the phonon density of states (DOS, $g(\omega)$) can be calculated [99]. It represents the total number of modes with frequencies between ω and $\omega + \mathrm{d}\omega$, divided by the volume of the crystal. In the Debye model, the phonon DOS becomes a quadratic function of the frequency below

the limit ω_D and zero above

$$\omega = cq \quad \rightarrow \quad g(\omega) = \begin{cases} (3\omega^2)/(2\pi^2 c^3) & \text{if} \quad \omega < \omega_D \\ 0 & \text{if} \quad \omega > \omega_D. \end{cases} \tag{5.15}$$

In the Einstein model, the phonon DOS is a Delta function at ω_E

$$\omega = \omega_E \quad \rightarrow \quad g(\omega) \propto \delta(\omega - \omega_E). \tag{5.16}$$

Both cases are shown schematically in Fig. 5.3 (a). The characteristic frequencies ω_D and ω_E are called the Debye and Einstein frequencies, respectively. They are related to the Debye and Einstein temperatures, Θ_D and Θ_E, respectively, by $\omega_D = \Theta_D k_B/\hbar$ and $\omega_E = \Theta_E k_B/\hbar$, where k_B denotes Boltzmann's constant and $\hbar$ stands for Planck's constant divided by 2π. For a crystal that is well described by the Debye model, a so-called Debye crystal, vibrations are isotropic and all NN shells are characterized by the same Debye temperature.

Figure 5.3 (b) shows the phonon DOS measured and simulated for InP [100]. Comparing panel (a) and (b), it becomes clear that both models present a rather crude approximation of the real DOS. Despite the strong simplification, both models have been applied successfully to describe thermal and vibrational properties of a large number of materials. Note that the Einstein frequency represents an average over the whole phonon spectrum and it is usually not possible to re-

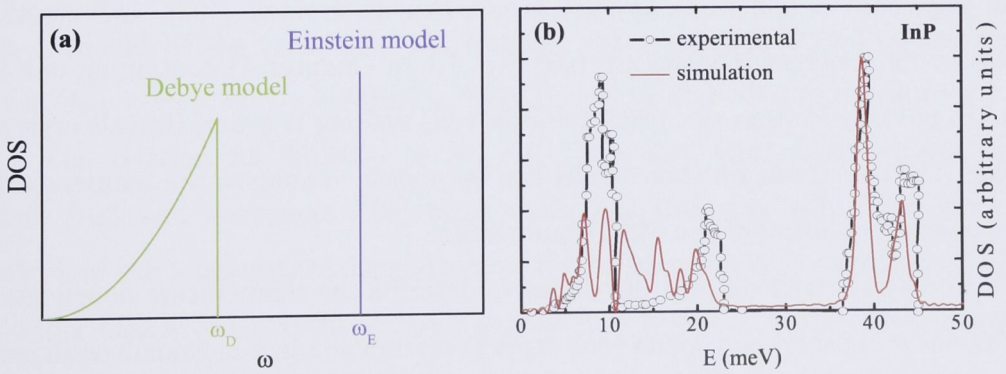

Figure 5.3: (a) Phonon DOS versus frequency ω according to the Debye and Einstein models. (b) Measured and simulated DOS versus phonon energy E for InP (taken from [100]). E is related to the frequency by $E = \hbar\omega$.

late ω_E to any specific feature of the DOS. Nevertheless, it is a useful quantity to monitor changes due to material modifications.

5.1.3 Temperature dependence of the cumulants

As shown in Section 5.1.1, the EXAFS Debye-Waller factor σ^2_{EXAFS} corresponds to the $MSRD_{\parallel}$ and is a measure for the relative vibrations along the line connecting the absorber-backscatterer pair. If the atoms move in phase, the MSRD will be significantly reduced with respect to the uncorrelated MSD and could equal zero if both atoms have the same MSD ($MSD_0 = MSD_j$ in Eq. (5.11)). Such correlations must be taken into account when modeling the temperature evolution of the EXAFS signal. Beni and Platzman [96] and Sevillano *et al.* [101] have developed *correlated* Debye and Einstein models to correctly describe the change of σ^2_{EXAFS} as a function of temperature. Vaccari and Fornasini have recently presented a rigorous derivation of these two models, substantiating their theoretical foundation [102].

The applicability of the correlated Debye model for non-Bravais crystals has been questioned since the best fitting Debye temperatures for σ^2_{EXAFS} vary significantly from shell to shell (see Section 5.2) and in comparison to values obtained with other experimental techniques [94]. Furthermore, Vaccari and Fornasini show that the derivation of the correlated Debye model for EXAFS MSRDs is not physically sound when applied to non-Bravais crystals [102]. InP crystallizes in the zincblende structure (see Fig. 4.1 in Chapter 4) containing one In atom and one P atom per primitive unit cell, making it a non-Bravais crystal. Thus, the correlated Einstein model has been used to analyze the temperature-dependent evolution of the MSRD and MSD.

The Einstein model was developed to describe the temperature dependence of the heat capacity and treats each atom as an independent harmonic oscillator. In contrast, the correlated Einstein model describing the temperature evolution of the EXAFS signal assumes each absorber-backscatterer pair to be an independent oscillator. The frequency of relative vibrations $\omega_E = \sqrt{k_0/\mu}$ depends

on the force constant k_0 of the bond between the two atoms and on the reduced mass μ of the atomic pair. The correlated Einstein model can thus be applied to both crystalline and non-crystalline systems and the Einstein temperature simply represents a measure of the strength of the bonds.

The derivation of Vaccari and Fornasini [102] is based on the harmonic crystal approximation and starts with the relations between $\mathrm{MSRD}_{\parallel}$ or $\mathrm{MSRD}_{\perp}$ and the three-dimensional displacements of the atoms as derived in Section 5.1.1 (see Eqs (5.2), (5.9) and (5.12)). The MSRDs are then expressed in terms of eigenfrequencies and eigenvectors of the dynamical matrix. Using the Einstein model approximations $\omega = \omega_{\mathrm{E}}$ and $g(\omega) \propto \delta(\omega - \omega_{\mathrm{E}})$ introduced in Section 5.1.2, the following relations are obtained

$$\begin{aligned} \mathrm{MSRD}_{\parallel} &= \frac{\hbar^2}{\mu k_{\mathrm{B}}} \frac{1}{2\Theta_{\mathrm{E},\parallel}} \coth\left(\frac{\Theta_{\mathrm{E},\parallel}}{2T}\right) + \sigma^2_{\mathrm{static},\parallel} \\ \mathrm{MSRD}_{\perp} &= \frac{\hbar^2}{\mu k_{\mathrm{B}}} \frac{1}{\Theta_{\mathrm{E},\perp}} \coth\left(\frac{\Theta_{\mathrm{E},\perp}}{2T}\right) + \sigma^2_{\mathrm{static},\perp}. \end{aligned} \tag{5.17}$$

In [102] only the temperature-dependent terms are given. Here, static contributions are added to account for different configurations of structural disorder present in the various samples. The two equations differ only by $\Theta_{\mathrm{E},\parallel}$ versus $\Theta_{\mathrm{E},\perp}$ and a factor of two. The latter is related to the fact that the $\mathrm{MSRD}_{\parallel}$ describes vibrations along a line while the $\mathrm{MSRD}_{\perp}$ describes vibrations in a plane. As Vaccari and Fornasini point out, there is no *a priori* reason, why $\Theta_{\mathrm{E},\parallel}$ and $\Theta_{\mathrm{E},\perp}$ should be the same. For the isotropic case, however, it can be assumed that $\Theta_{\mathrm{E},\parallel} = \Theta_{\mathrm{E},\perp}$ and $\gamma = \mathrm{MSRD}_{\perp}/\mathrm{MSRD}_{\parallel} = 2$ as discussed in Section 5.1.1.

The relation for $\mathrm{MSRD}_{\parallel}$ in Eq. (5.17) is also derived by Frenkel and Rehr [103] and Yokoyama [104] using a pair-potential approach. They further calculate the temperature dependence of the third and fourth cumulants by including higher order terms in the potential and applying perturbation theory. Treating the absorber-backscatterer pair as a one-dimensional oscillator, an interatomic potential of the form

$$V(R) = \frac{1}{2}k_0(R - R_0)^2 - k_3(R - R_0)^3 + \ldots \tag{5.18}$$

is assumed. Here, k_0 and k_3 are the harmonic and cubic force constants, respectively. The moments of the resulting distance distribution and their temperature dependence can then be calculated. The second and third moment correspond to the EXAFS second and third cumulant. In contrast, the first moment calculated within this framework does not represent the EXAFS first cumulant due to the fact that the one-dimensional model cannot take into account the effect of perpendicular vibrations [23]. The leading order term for $\sigma^2_{\mathrm{EXAFS}} = \mathrm{MSRD}_{\parallel}$ is given in Eq. (5.17). For the third cumulant the following relation is obtained

$$C_3 = \frac{\hbar^6}{\mu^3 k_{\mathrm{B}}^4} \frac{k_3}{\Theta_{\mathrm{E},\parallel}^4} \left[\frac{3}{2} \left(\coth\left(\frac{\Theta_{\mathrm{E},\parallel}}{2T} \right) \right)^2 - 1 \right] + C_{3,\mathrm{static}}. \tag{5.19}$$

A static contribution has again been added to the temperature-dependent term to account for structural disorder. In this work, Eqs (5.17) and (5.19) have been applied to determine the Einstein temperatures and anharmonic force constants of crystalline and amorphous InP. A derivation of the expressions for $\mathrm{MSRD}_{\parallel}$ and C_3 based on the pair-potential approach is presented in Appendix A.

5.2 Temperature-dependent EXAFS studies

Beni and Platzman [96] and Sevillano *et al.* [101] performed pioneering works for vibrational studies using temperature-dependent EXAFS measurements. The authors point out the difference between the *uncorrelated* MSD sampled by XRD measurements and the *correlated* MSRD obtained from EXAFS. Beni and Platzman also discuss the effect of anisotropic vibrations in Zn, which has a hexagonal crystal structure, and use different directional Debye temperatures to describe the relative atomic motion along the different crystallographic directions [96]. Since then many different systems have been studied, among them cubic metals [23,94], mono-elemental [25,27,105] and binary [26,28] semiconductors and AgI [24,29].

In an ideal Debye crystal, thermal vibrations and relative vibrations are isotropic and $\gamma = \mathrm{MSRD}_{\perp}/\mathrm{MSRD}_{\parallel} = 2$ as discussed in Sections 5.1.1 and 5.1.3.

Furthermore, the MSRDs of all coordination shells are described by the same Debye temperature. Fornasini *et al.* find γ for the first NN shell of Cu, a mono-elemental metal with the face-centered cubic structure, to be between 2 and 3 and thus close to the isotropic value [23]. The Debye temperatures of the first four coordination shells are very similar with only the value for the second shell $\sim$ 10-15 % lower as compared to the others. Cu thus closely resembles a perfect Debye crystal.

For Ge, a mono-elemental semiconductor with the diamond structure, γ of the first NN shell increases from ~ 3 at 10 K to ~ 5 at 300 K [25]. Furthermore, the $\mathrm{MSRD}_{\parallel}$ is much higher for the second and third NN shells than for the first NN shell [27]. This would yield different Debye temperatures for different NN shells in contradiction with the assumptions of the Debye model. The authors have therefore fitted the temperature dependence of the EXAFS Debye-Waller factors with a correlated Einstein model. The Einstein temperatures then simply represent a measure for the strength of relative vibrations between the absorber and backscattering atoms in the different NN shells. The values obtained for the first shell ($\Theta_{\mathrm{E},\parallel} = 360 \pm 10\,\mathrm{K}$) and for the higher shells ($\Theta_{\mathrm{E},\parallel} = 170 - 200\,\mathrm{K}$) differ by a factor of almost two [27].

A similar finding to that of Ge is reported for GaAs, a binary semiconductor with the zincblende structure [28]. Here the ratio between the Einstein temperatures for first and third NN shell even exceeds a factor of two. Furthermore, the authors compare the measured $\mathrm{MSRD}_{\parallel}$ to the uncorrelated MSD for Ga and As atoms. For the first NN shell, they observe that relative vibrations are strongly reduced with respect to the MSD. For the second NN shell, the $\mathrm{MSRD}_{\parallel}$ is still slightly smaller than the MSD whereas both agree very well for the third NN shell. This strikingly different behavior compared to Cu is attributed to the presence of optical modes in non-Bravais lattices and demonstrates the different extent to which atomic motion is correlated in the various coordination shells.

CdSe [26] and AgI [24], both with a wurtzite structure and more ionic bonding character, have a first NN γ of ~ 13 and ~ 10, respectively. Furthermore, for

AgI the $MSRD_{\parallel}$ measured for the second NN shell around the absorbing I atom is about four to five times larger than that observed for the first NN shell [29]. Considering the eigenvectors of the optical modes, the authors relate this difference to the specific motion of the various atoms and the resulting relative vibrations. Thus, EXAFS measurements can serve as a test for phonon eigenvectors obtained from dynamical models or *ab initio* calculations [23, 24, 29].

5.3 Experimental details

5.3.1 Sample preparation

Powder samples suitable for transmission EXAFS measurements were prepared for both crystalline and amorphous InP. For c-InP, a single-crystal InP wafer was finely crushed and mixed with boron nitride. For a-InP, the amorphous phase was produced by ion irradiation with either electronic (SHI regime) or nuclear (LEI regime) energy deposition. As-irradiated SHI and LEI samples were prepared as described in Section 4.2.1.

5.3.2 Measurement

EXAFS measurements of the In K-edge (27.940 keV) were performed in transmission mode at beam line NW10A at the Photon Factory, Japan. Spectra were recorded at eight different temperatures ranging from 20 to 295 K. After the measurements, the SHI and LEI samples were relaxed by annealing at 150°C for one hour and then remeasured (see Sections 4.2.2 and 4.4.1).

5.4 Analysis

5.4.1 EXAFS spectra

The data were processed using the IFEFFIT code [40] and the corresponding user interface ATHENA [41]. After background removal, FT was performed over

the photoelectron wave number k range of $k = 2 - 13.5\,\text{Å}^{-1}$. Figure 5.4 (a) and (b) show k^3-weighted EXAFS spectra as a function of k measured at 20 and 295 K for c-InP and a-InP (SHI relaxed), respectively. The corresponding FTs are plotted in Fig. 5.4 (c) and (d). For c-InP, scattering from the first three NN shells can be identified as discussed in Section 4.3.1. Interestingly, while the signal of the first peak in Fig. 5.4 (c) (corresponding to first NN P atoms) is reduced by about 20 % upon increasing the temperature from 20 to 295 K, the second (In) and third (P) NN peaks almost vanish. This clearly indicates a different thermal behavior for the different NN shells. For a-InP (Fig. 5.4 (d)), only scattering from the first NN shell can be observed due to the increased disorder present in the amorphous phase. As discussed in Section 4.3.1, this shell is now comprised of both P and In atoms yielding a double-peak structure of the spectrum: scattering due to In-P and In-In pairs appears at $R \sim 2.1$ Å and

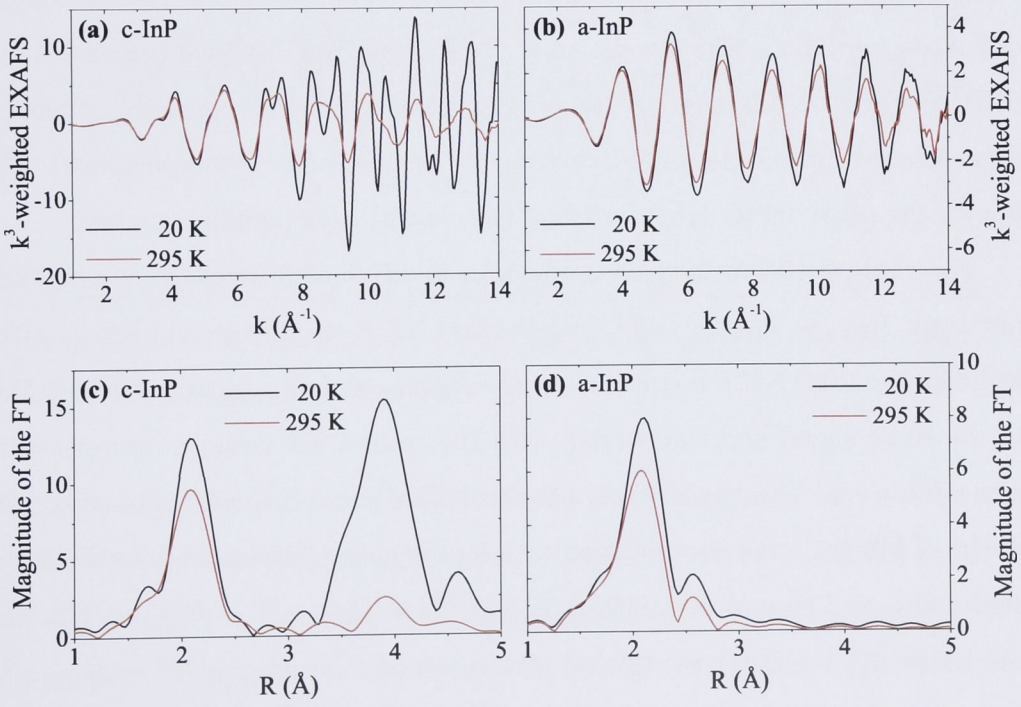

Figure 5.4: k^3-weighted EXAFS spectra of (a) c-InP and (b) a-InP (SHI relaxed) measured at 20 K and 295 K versus the photoelectron wave number k. (c), (d) Corresponding FTs as a function of the non-phase-corrected radial distance R from the absorber.

$R \sim 2.6\,\text{Å}$, respectively. Increasing the measurement temperature leads to a decrease of the scattering signal for both contributions with the relative drop for In-P being similar to that observed for c-InP.

5.4.2 Fitting

The spectra were fitted in radial space with multiple k-weights $= 2, 3, 4$ over a range of $R = 1.5 - 4.9\,\text{Å}$ using the IFEFFIT code [40] and the corresponding user interface ARTEMIS [41]. Scattering amplitudes and phase shifts were calculated *ab initio* with FEFF8 [36] while the amplitude reduction factor S_0^2 and the threshold energy E_0 were determined from the crystalline sample and then fixed throughout the analysis. Note that floating S_0^2 and E_0 for each measured temperature gave only a slight variation of the values that was significantly smaller than the experimental uncertainty and showed no trend with temperature. Hence, the parameters were fixed to average values, similar to the analysis of Sanson *et al.* [98]. Fits are shown in Fig. 5.5 (a) and (b) for c-InP and a-InP (SHI relaxed), respectively, together with the back-transformed experimental data. Clearly, fit and data are in excellent agreement for all temperatures. The fits for the other three a-InP samples (not shown) are of similar quality.

For c-InP, the following parameters were determined from the fit at each temperature: R_{EXAFS}, σ^2_{EXAFS} and C_3 for the first NN P and the second NN In paths while for the third NN P contribution only R_{EXAFS} and σ^2_{EXAFS} were floated. Due to the small signal and the overlap with the second NN peak, no temperature dependence could be extracted for the third NN C_3 and it was fixed to zero. The [In-In-P] MS path was also included with its distance restrained by the distances of the first and second NN paths, ${R_{\text{EXAFS}}}^{(\text{MS})} = {R_{\text{EXAFS}}}^{(1)} + {R_{\text{EXAFS}}}^{(2)}/2$, and the Debye-Waller factor set to that of the second NN, ${\sigma^2_{\text{EXAFS}}}^{(\text{MS})} = {\sigma^2_{\text{EXAFS}}}^{(2)}$. Tests were also performed with ${\sigma^2_{\text{EXAFS}}}^{(\text{MS})} = {\sigma^2_{\text{EXAFS}}}^{(2)}/2$ and without including the MS path altogether corresponding to the two extreme cases of heavily over- or underestimating the influence of the MS path, respectively. None of the choices of how to treat the third NN path or the MS path had a significant in-

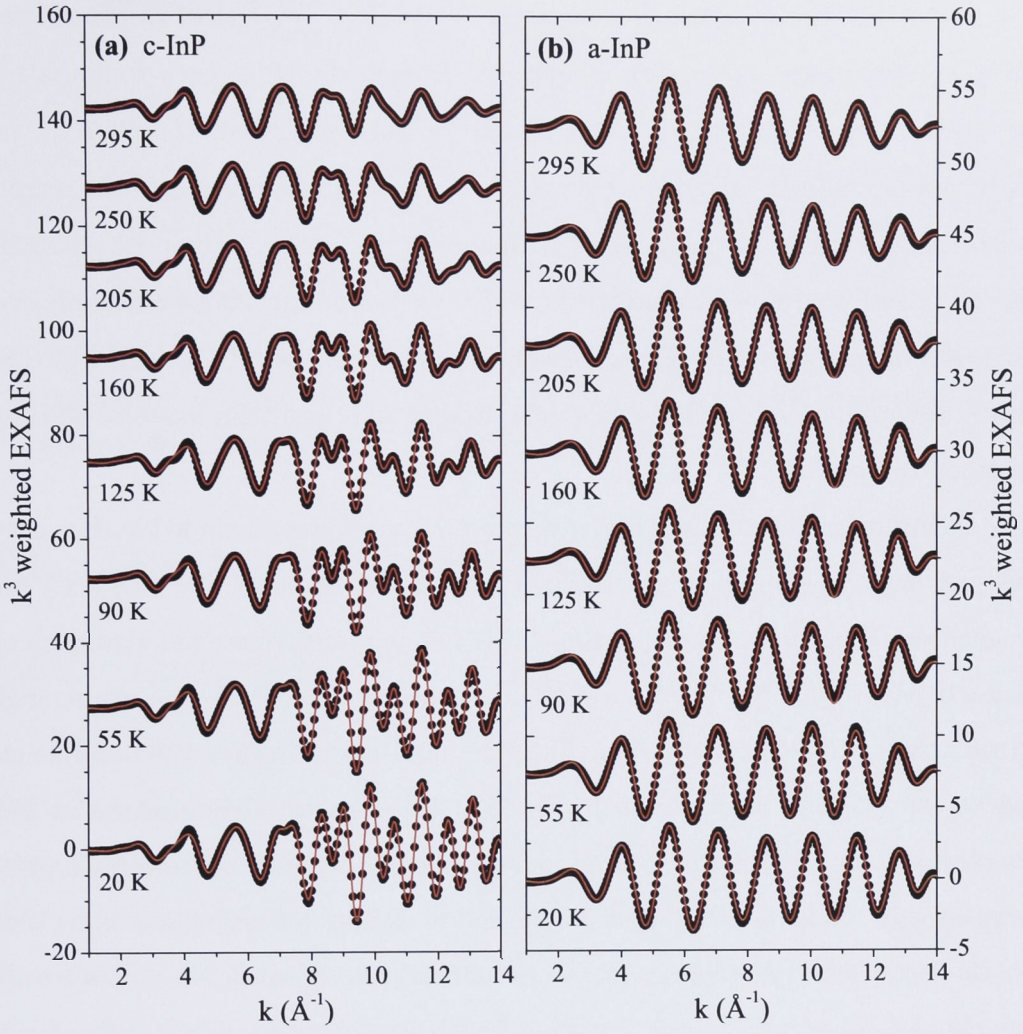

Figure 5.5: k^3-weighted back-transformed experimental data and best fits versus the photoelectron wave number k for (a) c-InP and (b) a-InP (SHI relaxed). Graphs for different temperatures are offset for clarity.

fluence on the first NN parameters or on the Debye-Waller factors of the higher shells. It did, however, strongly influence the second and third NN distances as well as $C_3{}^{(2)}$, a fact that should be kept in mind when interpreting these parameters. Furthermore, including a C_4 for the first NN path yielded values that were zero within uncertainty. Including C_4 in the higher shell fits will not result in physically meaningful values given the number of free parameters already present. Hence, fourth order cumulants were not further considered in the fitting procedure.

For a-InP, the coordination numbers N for first NN P and In atoms were fixed to the values obtained in Chapter 4. During the fit at each temperature, separate R_{EXAFS} and $\sigma^2_{\mathrm{EXAFS}}$ were floated for both contributions while C_3 was only varied for In-P. Given the comparatively weak In-In signal and the overlap with the In-P peak, no meaningful temperature dependence could be extracted for an In-In C_3. However, a positive C_3 is expected in amorphous materials even at low temperatures [27]. Thus, for consistency, a constant C_3 was included for In-In, determined from the spectra measured at 20 K and then fixed for all other temperatures.

To minimize the number of free parameters, no C_3 was included in the analysis presented in Chapter 4. With the coordination numbers now fixed, C_3 was reintroduced in the fit, knowing that these two parameters are not strongly correlated (see Eq. (2.18) in Section 2.2.3). In contrast, C_3 and R_{EXAFS} are strongly correlated and the inclusion of a third cumulant can influence the bond length parameter. Tables 5.1 and 5.2 list the first NN structural parameters at 20 K as obtained with the fitting procedure described above for In-P and In-In pairs, respectively. Compared to the values given in Tables 4.4 and 4.5, a slight shift in the bond lengths is apparent. These differences, however, do not alter the conclusion drawn in Chapter 4, namely that there is no significant difference in the atomic structure of SHI and LEI a-InP samples.

1^{st} NN In-P		N	R_{EXAFS} (Å)	$\sigma^2_{\mathrm{EXAFS}}$ (10^{-3} Å^2)	C_3 (10^{-5} Å^3)
c-InP		4	2.541 ± 0.005	2.5 ± 0.2	-2 ± 7
a-InP SHI	as-irrad.	3.43	2.584 ± 0.003	5.6 ± 0.2	22 ± 7
	relaxed	3.54	2.576 ± 0.003	5.0 ± 0.2	16 ± 6
a-InP LEI	as-irrad.	3.47	2.584 ± 0.003	5.8 ± 0.2	19 ± 6
	relaxed	3.57	2.580 ± 0.002	5.3 ± 0.2	18 ± 5

Table 5.1: The In-P bond length R_{EXAFS}, Debye-Waller factor $\sigma^2_{\mathrm{EXAFS}}$ and third cumulant C_3 obtained for c-InP and a-InP measured at a temperature of 20 K. Also given are the In-P coordination numbers determined in Chapter 4.

1^{st} NN In-In		N	R_{EXAFS} (Å)	$\sigma^2_{\mathrm{EXAFS}}$ (10^{-3} Å^2)	C_3 (10^{-5} Å^3)
a-InP SHI	as-irrad.	0.70	2.799 ± 0.006	5.8 ± 0.5	10 ± 20
	relaxed	0.66	2.796 ± 0.006	5.8 ± 0.5	20 ± 20
a-InP LEI	as-irrad.	0.63	2.813 ± 0.004	4.4 ± 0.3	30 ± 20
	relaxed	0.57	2.808 ± 0.004	4.4 ± 0.3	30 ± 20

Table 5.2: The In-In bond length R_{EXAFS}, Debye-Waller factor $\sigma^2_{\mathrm{EXAFS}}$ and third cumulant C_3 obtained for a-InP measured at a temperature of 20 K. Also given are the In-In coordination numbers determined in Chapter 4.

5.5 Results and discussion

5.5.1 Crystalline InP

Table 5.3 lists the fitting parameters determined for c-InP. The values are plotted versus temperature in Fig. 5.6. The Debye-Waller factor $\sigma^2_{\mathrm{EXAFS}}$ increases with both temperature and distance of the absorber-backscatterer pair. Strikingly, the values for the second and third NN shell increase at a higher rate than those of the first NN shell, reflecting differences in the thermally-induced amplitude reduction for these shells. A similar behavior has been observed for Ge [27], GaAs [28] and AgI [29] (see Section 5.2).

$\Delta R_{\mathrm{EXAFS}} = R_{\mathrm{EXAFS}}(T) - R_{\mathrm{EXAFS}}(0\,\mathrm{K})$ and C_3 for the first NN P slightly increase with temperature. For the second NN In, they both increase with temperature more rapidly than the first NN values for all fitting protocols. Relating the relative increase $\Delta R_{\mathrm{EXAFS}}/R_{\mathrm{EXAFS}}$ of the first and second shell to each other or to the relative lattice expansion $\Delta R_{\mathrm{C}}/R_{\mathrm{C}}$ is far from trivial since R_{EXAFS} depends on the crystallographic distance R_{C} and on the relative vibrations perpendicular to the line connecting absorber-backscatterer pair (Eqs (5.6) and (5.14)). The relative lattice expansion $\Delta R_{\mathrm{C}}/R_{\mathrm{C}}$ is the same for all coordination shells. In contrast, the $\mathrm{MSRD}_{\perp}$ may be different for first and second NN shell due to a different correlation in the absorber-backscatter motion, as is indeed observed for the $\mathrm{MSRD}_{\parallel} = \sigma^2_{\mathrm{EXAFS}}$ (see Fig. 5.6 (b) and above). In

fact, this very difference between R_{EXAFS} and R_{C} is exploited to obtain information about the $\mathrm{MSRD}_{\perp}$ for the first NN shell (see below). Given the strong correlation between ${R_{\mathrm{EXAFS}}}^{(2)}$ and ${C_3}^{(2)}$, the large uncertainties of the values and the dependence of the results on the fitting protocol, no such analysis or physical interpretation is attempted for the second shell. Similarly, the nearly constant $\Delta R_{\mathrm{EXAFS}}$ for third NN P is not physically meaningful without including a temperature-dependent C_3. The choice of not including a C_3 for the third NN shell rather than having a constant non-zero value is justified given that C_3 is approximately zero at low temperature for both first and second NNs.

First NN shell

Figure 5.7 (a) shows the first NN distance R_{EXAFS} determined from EXAFS and the R_{C} values obtained from XRD measurements by Deus *et al.* [106], as a function of temperature T. Two characteristics are readily apparent: R_{EXAFS} is larger than R_{C} at all temperatures and the difference increases with increasing temperature. As discussed in Section 5.1.1, this difference results from vibrations perpendicular to the bond direction. The increase of R_{C} with temperature is caused only by the anharmonicity of the crystal potential while the increase of R_{EXAFS} is also due to the increase of vibrational motion at higher temperatures.

Figure 5.7 (b) plots the $\mathrm{MSRD}_{\perp}$ determined from the values shown in Fig. 5.7 (a) together with the $\mathrm{MSRD}_{\parallel} = \sigma^2_{\mathrm{EXAFS}}$ for first NN P. The $\mathrm{MSRD}_{\perp}$ is larger than the $\mathrm{MSRD}_{\parallel}$ and increases more rapidly with temperature. The ratio $\gamma = \mathrm{MSRD}_{\perp}/\mathrm{MSRD}_{\parallel}$, plotted in Fig. 5.7 (c), is close to the isotropic value of 2 at low temperatures and increases to approximately 10 at room temperature. This value is significantly higher than that of ~ 5 reported for Ge [25] and similar to the values of ~ 13 and ~ 10 determined for CdSe [26] and AgI [24], respectively. Three cases can therefore be distinguished:

(i) Cu with γ close to the isotropic value of 2 [23],

(ii) Ge which already exhibits vibrational anisotropy and

(iii) InP, CdSe and AgI with the highest values of γ.

	1^{st} NN P			2^{nd} NN In			3^{rd} NN P	
T (K)	R_{EXAFS} (Å)	$\sigma^2_{\mathrm{EXAFS}}$ (10^{-3} Å^2)	C_3 (10^{-5} Å^3)	R_{EXAFS} (Å)	$\sigma^2_{\mathrm{EXAFS}}$ (10^{-3} Å^2)	C_3 (10^{-5} Å^3)	R_{EXAFS} (Å)	$\sigma^2_{\mathrm{EXAFS}}$ (10^{-3} Å^2)
20	2.541 ± 0.005	2.5 ± 0.2	-2 ± 7	4.169 ± 0.005	3.5 ± 0.1	7 ± 6	4.882 ± 0.007	4.2 ± 0.7
55	2.541 ± 0.004	2.4 ± 0.2	-2 ± 6	4.170 ± 0.006	4.5 ± 0.1	8 ± 6	4.881 ± 0.007	5.4 ± 0.8
90	2.544 ± 0.004	2.7 ± 0.2	2 ± 6	4.174 ± 0.007	5.9 ± 0.2	13 ± 8	4.882 ± 0.009	7.1 ± 1.0
125	2.544 ± 0.004	2.8 ± 0.2	3 ± 7	4.174 ± 0.008	7.1 ± 0.2	14 ± 10	4.881 ± 0.011	8.7 ± 1.4
160	2.545 ± 0.004	3.1 ± 0.2	3 ± 6	4.177 ± 0.009	8.3 ± 0.3	16 ± 12	4.882 ± 0.012	9.7 ± 1.4
205	2.544 ± 0.004	3.4 ± 0.2	2 ± 6	4.184 ± 0.010	9.7 ± 0.3	28 ± 14	4.882 ± 0.013	11.2 ± 1.6
250	2.548 ± 0.004	3.9 ± 0.2	5 ± 7	4.198 ± 0.015	11.6 ± 0.5	44 ± 22	4.885 ± 0.017	12.9 ± 2.2
295	2.551 ± 0.004	4.3 ± 0.2	9 ± 6	4.203 ± 0.018	13.4 ± 0.7	53 ± 28	4.885 ± 0.020	15.2 ± 2.5

Table 5.3: Structural parameters obtained for c-InP.

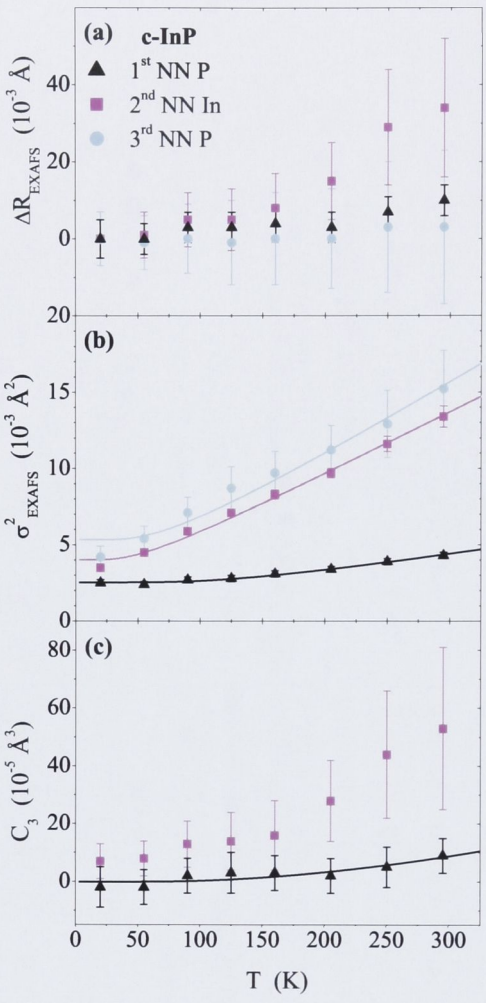

Figure 5.6: (a) Interatomic distance $\Delta R_{\mathrm{EXAFS}} = R_{\mathrm{EXAFS}}(T) - R_{\mathrm{EXAFS}}(0\,\mathrm{K})$, (b) Debye-Waller factor $\sigma^2_{\mathrm{EXAFS}}$ and (c) third cumulant C_3 versus temperature T for the first three NN shells of c-InP. The lines show the corresponding fits with the Einstein model.

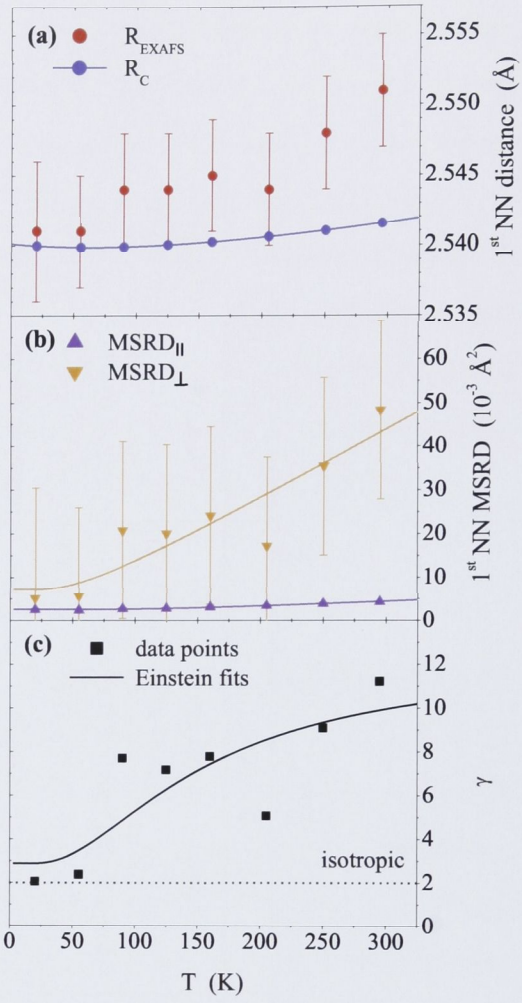

Figure 5.7: (a) First NN distance of c-InP determined by EXAFS, R_{EXAFS}, and by XRD [106], R_{C}, versus temperature T. (b) $\mathrm{MSRD}_{\parallel}$ and $\mathrm{MSRD}_{\perp}$ as a function of T. The solid lines show the corresponding Einstein fits. (c) $\gamma = \mathrm{MSRD}_{\perp}/\mathrm{MSRD}_{\parallel}$ for the data points and the fits given in panel (b).

The latter three materials behave similarly despite their different crystal structures and different ratios of mass and electronegativity of their atomic constituents. Significant vibrational anisotropy is thus present in the materials studied with a non-Bravais lattice structure. Furthermore, it is more pronounced for the binaries compared to mono-elemental Ge.

As noted by Fornasini *et al.*, the main contribution to the third cumulant comes from the anharmonicity of the crystal potential [23]. InP, CdSe [26] and Cu [23] all show very similar values for C_3 ranging from 9 to 15 $\times$ 10^{-5} Å^3 at room temperature. For Ge, a slightly lower value of 3 $\times$ 10^{-5} Å^3 has been reported [25, 107]. In contrast, AgI exhibits much greater anharmonicity, with $C_3 \sim 80 \times 10^{-5}$ Å^3 [24].

The degree of correlation governing the motion of the different NN shells becomes apparent when comparing the EXAFS MSRDs to the MSDs determined by XRD. The one-dimensional MSD has been calculated by $\mathrm{MSD_{In+P}} = (B_{\mathrm{In}} + B_{\mathrm{P}})/8\pi^2$ and $\mathrm{MSD_{In+In}} = (B_{\mathrm{In}} + B_{\mathrm{In}})/8\pi^2$ for In-P and In-In pairs, respectively, where B_{In} and B_{P} are the XRD Debye-Waller factors for In and P atoms, respectively (see Eq. (5.10)). Experimental XRD B values of InP are reported for room temperature by Saravanan *et al.* [108] while Reid calculated B values for a variety of zincblende materials over a large temperature range [109]. Schowalter *et al.* recently computed and parametrized the MSD temperature dependence for group IV, III-V and II-VI semiconductors [110]. The values are shown in Fig. 5.8 (a) and (b) for In-P and In-In pairs, respectively. Also plotted are the first NN $\mathrm{MSRD}_{\parallel}$ and $\mathrm{MSRD}_{\perp}/2$ and the third NN $\mathrm{MSRD}_{\parallel}$ in panel (a). The second NN $\mathrm{MSRD}_{\parallel}$ is shown in panel (b). Since all MSDs and $\mathrm{MSRD}_{\parallel}$s represent atomic motion along a line, a factor of 1/2 was applied to the $\mathrm{MSRD}_{\perp}$ (which describes atomic motion in a plane) for comparison.

Considering the first NN shell (Fig. 5.8 (a)), it is now evident that the $\mathrm{MSRD}_{\parallel}$ is much smaller than the MSD while the $\mathrm{MSRD}_{\perp}/2$ is very similar. The MSD values reported by Schowalter *et al.* were calculated based on the assumption that thermal vibrations of individual atoms are isotropic [110]. The sum of the first two terms in the last line of Eq. (5.9) thus corresponds to the $\mathrm{MSD_{In+P}}$. A smaller $\mathrm{MSRD}_{\parallel}$ is then only possible if the absorber and backscatterer vibrations along the bond direction are at least partially *in phase* resulting in a positive displacement correlation function (given by the last term of Eq. (5.9)). Using Eq. (5.11), the $\mathrm{MSRD}_{\parallel}$ lower limit for the case of vibrations perfectly

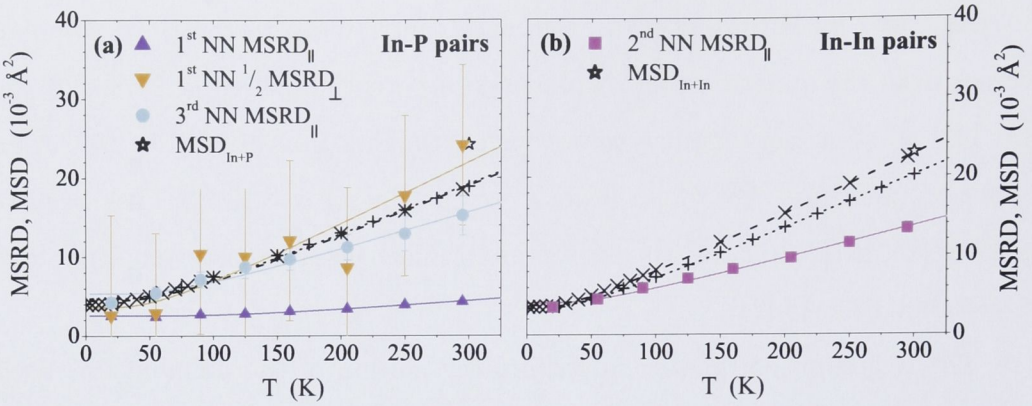

Figure 5.8: MSDs and MSRDs for (a) In-P and (b) In-In pairs of c-InP. The MSD values were derived from the data measured by Saravanan *et al.* [108] (open stars) and calculated by Reid [109] (× crosses) and Schowalter *et al.* [110] (+ crosses). The lines give the corresponding Einstein fits.

in phase has been calculated from the MSD values by Schowalter *et al.* [110] and amounts to 0.04×10^{-3} Å^2 at 295 K. This value is significantly smaller than the measured $\mathrm{MSRD}_{\parallel} = 4.3 \pm 0.2 \times 10^{-3}$ Å^2. The difference between MSD and $\mathrm{MSRD}_{\parallel}$ values is thus consistent with a strong (but not complete) in-phase-motion of the neighboring atoms along the bond direction. In contrast, as a consequence of the similarity of MSD and $\mathrm{MSRD}_{\perp}/2$, the last term in Eq. (5.12) is negligible indicating that the vibrations perpendicular to the bond direction are mostly uncorrelated.

This behavior is further illustrated by the Einstein temperatures Θ_{E} given in Table 5.4 that were obtained from best fits of the data with the Einstein model (Eq. (5.17) and Fig. 5.8). While relative vibrations parallel to the bond direction are characterized by $\Theta^{(1)}_{\mathrm{E},\parallel} = 392 \pm 8$ K, the value for relative vibrations perpendicular is $\Theta^{(1)}_{\mathrm{E},\perp} = 160 \pm 20$ K in good agreement with $\Theta^{\mathrm{MSD}}_{\mathrm{E}} = 174 \pm 2$ K for the $\mathrm{MSD}_{\mathrm{In+P}}$. No direct measurement of the Einstein temperature for InP has been reported so far. Debye temperatures published in the literature range from 210 to 440 K depending on the temperature and method of determination [78, 111]. Einstein temperatures reported for the EXAFS first NN $\mathrm{MSRD}_{\parallel}$ of Ge range from 350 to 360 K [25, 27, 107] while for GaAs $\Theta^{(1)}_{\mathrm{E},\parallel} = 360 \pm 20$ K [28] was observed.

c-InP		Θ_E (K)	σ^2_{static} (10^{-3}Å^2)
In-P	MSD_{In+P} [109]	174 ± 2	-1.2 ± 0.2
	MSD_{In+P} [110]	174 ± 2	-1.0 ± 0.2
	1^{st}NN $MSRD_{\parallel}$	392 ± 8	0.0 ± 0.2
	1^{st}NN $^1/_2$ $MSRD_{\perp}$	160 ± 20	-3 ± 10
	3^{rd}NN $MSRD_{\parallel}$	200 ± 10	0.4 ± 0.7
In-In	MSD_{In+In} [109]	105 ± 1	-0.3 ± 0.1
	MSD_{In+In} [110]	112 ± 1	-0.2 ± 0.1
	2^{nd}NN $MSRD_{\parallel}$	143 ± 5	1.1 ± 0.2

Table 5.4: Einstein temperature Θ_E and static contribution to the Debye-Waller factor σ^2_{static} as determined from fits with a correlated Einstein model for c-InP.

Though the significant difference between relative vibrations parallel and perpendicular to the bond direction may at first seem surprising, it is consistent with the well-known behavior of III-V semiconductor ternary alloys where the lattice mismatch of the binary compounds is accommodated primarily by bond angle relaxation and to a much lesser extent by bond length relaxation (see Chapter 6 and references therein). Bond bending is thus energetically much more favorable than bond stretching. Since relative vibrations parallel to the bond require bond stretching whereas relative vibrations perpendicular to the bond mainly involve bond bending, the observed vibrational anisotropy can be easily understood.

Many of the models that describe the structural distortions in ternary alloys use the Keating potential which consists of bond stretching and bond bending terms (see Eq. (6.2) in Section 6.1.2) [112]. The corresponding force constants α and β are deduced from fitting experimental bulk moduli and elastic constants [113, 114]. Considering only the bond stretching term for a single bond and comparing the coefficient of the harmonic contribution with the pair-potential given by Eq. (5.18) in Section 5.1.3, it follows that $k^{(1)}_{0,\parallel} = 3\alpha$. The value of $k^{(1)}_{0,\parallel} = 107 \pm 4\,\mathrm{Nm}^{-1}$ obtained herein indeed agrees reasonably well with the values of $3\alpha = 129\,\mathrm{Nm}^{-1}$ and $3\alpha = 121\,\mathrm{Nm}^{-1}$ reported by Martin [113] and Chen and Sher [114], respectively. Furthermore, the ratio of parallel to per-

pendicular force constants determined in this work, $k^{(1)}_{0,\parallel}/k^{(1)}_{0,\perp} \sim 6$, agrees well with the ratio of bond stretching to bond bending force constants, $\alpha/\beta \sim 7$ and $\alpha/\beta \sim 6$, reported in [113] and [114], respectively. The strong vibrational anisotropy observed for InP in this study is clearly related to the difference in energy required for bond bending and bond stretching in III-V semiconductors with the zincblende structure.

Second and third NN shells

Comparing the $\mathrm{MSRD}_\parallel$ of the first three NN shells with the corresponding MSD (Fig. 5.8 (a) for In-P pairs and (b) for In-In pairs), the following is observed:

(i) The first NN $\mathrm{MSRD}_\parallel$ is significantly smaller than the $\mathrm{MSD}_{\mathrm{In+P}}$ due to a strong correlation of the first NN atomic motion as discussed above.

(ii) The second NN $\mathrm{MSRD}_\parallel$ is considerably larger than that of the first NNs but still significantly lower than the $\mathrm{MSD}_{\mathrm{In+In}}$.

(iii) The third NN $\mathrm{MSRD}_\parallel$ closely approaches the $\mathrm{MSD}_{\mathrm{In+P}}$ values.

These observations indicate that the degree of correlation governing the atomic motion decreases rapidly with increasing distance between the absorber-backscatterer pair. Correspondingly, the difference between the Einstein temperatures for $\mathrm{MSRD}_\parallel$ and MSD decreases with increasing scattering distance. A similar observation was reported for GaAs where the third NN $\mathrm{MSRD}_\parallel$ agrees well with the corresponding $\mathrm{MSD}_{\mathrm{Ga+As}}$ [28]. Note that for GaAs the Einstein temperatures decrease continually with increasing NN distance, while for InP the second NN value is smaller than that of the third NN, $\Theta^{(2)}_{\mathrm{E},\parallel} = 143 \pm 5\,\mathrm{K} < \Theta^{(3)}_{\mathrm{E},\parallel} = 200 \pm 10\,\mathrm{K}$, due to the large difference in reduced mass for In-P and In-In pairs (negligible for GaAs).

The decrease of correlated motion for the higher shells is consistent with the lack of physical bonds between the absorber and second or third NNs. A change of first NN distance requires energetically unfavorable bond stretching. In contrast, a change of second or third NN distance can be achieved by bond bending at the bridging atom without changing first NN bond lengths (see Sec-

tion 6.5.3). Additional bridging atoms thus make it more likely that energetically favored bond bending will lead to a change in the corresponding higher NN distance. Hence, the correlation of vibrations along the absorber-backscatterer line strongly decreases for the higher shells and already approaches the MSD for the third NN shell (two bridging atoms).

5.5.2 Amorphous InP

In contrast to the crystalline phase of InP which comprises only heteropolar bonds (In-P), the amorphous phase contains both heteropolar and homopolar bonds (P and In atoms, respectively, in the first NN shell around the In absorber). Tables 5.5-5.8 list the first NN structural parameters obtained for as-irradiated and relaxed SHI and LEI samples. Figure 5.9 plots the values versus temperature T for In-P and In-In contributions. For In-P (Fig. 5.9 (a), (c) and (e)), the first NN parameters of c-InP are also included for comparison. Tables 5.9 and 5.10 summarize the parameters obtained from the corresponding best fits using Eqs (5.17) and (5.19).

The EXAFS Debye-Waller factors for the first NN In-P pairs (Fig. 5.9 (c)) for all amorphous samples are much higher than the crystalline values but with a similar temperature-dependence. $\sigma^2_{\mathrm{EXAFS}}$ for the LEI and SHI samples are very similar with the values of the relaxed phase slightly lower than those of the as-irradiated state. This behavior is reflected by the parameters determined from the Einstein fits: $\Theta_{\mathrm{E},\parallel}^{(\mathrm{In\text{-}P})} \sim 390\,\mathrm{K}$ for c-InP, $\sim 370\,\mathrm{K}$ for as-irradiated a-InP and $\sim 380\,\mathrm{K}$ for relaxed a-InP. A slightly lower Einstein temperature of the amorphous phase compared to that of the crystalline phase has also been reported for Ge ($330 \pm 10\,\mathrm{K}$ and $360 \pm 10\,\mathrm{K}$, respectively [27]) and is consistent with slightly looser or floppier bonds in the amorphous material. The static contribution is zero for c-InP whereas $\sigma^2_{\mathrm{static},\parallel}{}^{(\mathrm{In\text{-}P})} \sim 3 \times 10^{-3}\,\mathrm{Å}^2$ for a-InP. Hence, *thermally* induced disorder is very similar for c-InP and a-InP while *structural* disorder is clearly much higher in the amorphous phase.

The other In-P parameters yield similar findings (Fig. 5.9 (a) and (e), re-

	1^{st} NN In-P			1^{st} NN In-In	
T (K)	R_{EXAFS} (Å)	$\sigma^2_{\mathrm{EXAFS}}$ (10^{-3} Å^2)	C_3 (10^{-5} Å^3)	R_{EXAFS} (Å)	$\sigma^2_{\mathrm{EXAFS}}$ (10^{-3} Å^2)
20	2.584 ± 0.003	5.6 ± 0.2	22 ± 7	2.799 ± 0.006	5.8 ± 0.5
55	2.587 ± 0.003	5.8 ± 0.2	23 ± 7	2.802 ± 0.005	5.3 ± 0.4
90	2.588 ± 0.004	5.9 ± 0.3	30 ± 8	2.797 ± 0.006	5.8 ± 0.5
125	2.590 ± 0.004	6.3 ± 0.2	26 ± 8	2.806 ± 0.006	5.8 ± 0.5
160	2.590 ± 0.005	6.7 ± 0.3	30 ± 11	2.807 ± 0.008	6.3 ± 0.7
205	2.594 ± 0.006	6.9 ± 0.4	45 ± 13	2.813 ± 0.009	6.7 ± 0.9
250	2.594 ± 0.004	7.5 ± 0.3	40 ± 11	2.812 ± 0.007	6.7 ± 0.6
295	2.593 ± 0.004	7.8 ± 0.3	46 ± 9	2.807 ± 0.007	8.2 ± 0.7

Table 5.5: Structural parameters obtained for the as-irradiated SHI sample.

	1^{st} NN In-P			1^{st} NN In-In	
T (K)	R_{EXAFS} (Å)	$\sigma^2_{\mathrm{EXAFS}}$ (10^{-3} Å^2)	C_3 (10^{-5} Å^3)	R_{EXAFS} (Å)	$\sigma^2_{\mathrm{EXAFS}}$ (10^{-3} Å^2)
20	2.576 ± 0.003	5.0 ± 0.2	16 ± 6	2.796 ± 0.006	5.8 ± 0.5
55	2.584 ± 0.002	5.2 ± 0.2	30 ± 5	2.813 ± 0.004	5.5 ± 0.4
90	2.582 ± 0.003	5.5 ± 0.2	20 ± 6	2.800 ± 0.006	6.1 ± 0.5
125	2.581 ± 0.003	5.7 ± 0.2	22 ± 6	2.804 ± 0.006	5.9 ± 0.5
160	2.583 ± 0.003	5.6 ± 0.2	27 ± 6	2.796 ± 0.006	6.8 ± 0.5
205	2.587 ± 0.003	6.1 ± 0.2	31 ± 6	2.806 ± 0.006	7.2 ± 0.6
250	2.585 ± 0.003	6.7 ± 0.2	30 ± 7	2.799 ± 0.007	7.8 ± 0.7
295	2.590 ± 0.003	7.2 ± 0.2	40 ± 6	2.808 ± 0.007	8.5 ± 0.6

Table 5.6: Structural parameters obtained for the relaxed SHI sample.

spectively). $\Delta R_{\mathrm{EXAFS}}$ values are very similar for all amorphous samples (with the relaxed values slightly lower than those for the as-irradiated samples) but significantly higher than the crystalline values. The latter is typical for semiconductors [20, 115] and is consistent with sampling more anharmonicity of the interatomic potential due to increased disorder in the amorphous phase. For both a-InP and c-InP, the temperature dependence of $\Delta R_{\mathrm{EXAFS}}$ is small. C_3 values of all a-InP samples are very similar and significantly higher than that of c-InP. Nevertheless, both phases show approximately the same temperature

	1^{st} NN In-P			1^{st} NN In-In	
T (K)	R_{EXAFS} (Å)	$\sigma^2_{\mathrm{EXAFS}}$ (10^{-3} Å^2)	C_3 (10^{-5} Å^3)	R_{EXAFS} (Å)	$\sigma^2_{\mathrm{EXAFS}}$ (10^{-3} Å^2)
20	2.586 ± 0.003	5.8 ± 0.2	19 ± 6	2.813 ± 0.004	4.4 ± 0.3
55	2.591 ± 0.003	5.7 ± 0.2	29 ± 6	2.814 ± 0.004	4.3 ± 0.3
90	2.591 ± 0.003	6.0 ± 0.2	29 ± 6	2.816 ± 0.004	5.1 ± 0.3
125	2.593 ± 0.003	6.2 ± 0.2	34 ± 7	2.818 ± 0.005	5.5 ± 0.4
160	2.592 ± 0.003	6.4 ± 0.2	35 ± 7	2.813 ± 0.005	5.5 ± 0.4
205	2.592 ± 0.003	7.0 ± 0.2	27 ± 7	2.818 ± 0.004	5.3 ± 0.3
250	2.591 ± 0.003	7.3 ± 0.2	37 ± 8	2.811 ± 0.006	7.0 ± 0.6
295	2.597 ± 0.003	8.0 ± 0.2	44 ± 8	2.820 ± 0.006	6.6 ± 0.5

Table 5.7: Structural parameters obtained for the as-irradiated LEI sample.

	1^{st} NN In-P			1^{st} NN In-In	
T (K)	R_{EXAFS} (Å)	$\sigma^2_{\mathrm{EXAFS}}$ (10^{-3} Å^2)	C_3 (10^{-5} Å^3)	R_{EXAFS} (Å)	$\sigma^2_{\mathrm{EXAFS}}$ (10^{-3} Å^2)
20	2.580 ± 0.002	5.3 ± 0.2	18 ± 5	2.808 ± 0.004	4.4 ± 0.3
55	2.584 ± 0.003	5.5 ± 0.2	24 ± 6	2.807 ± 0.005	4.6 ± 0.4
90	2.582 ± 0.002	5.6 ± 0.2	26 ± 5	2.805 ± 0.004	5.0 ± 0.3
125	2.583 ± 0.003	5.8 ± 0.2	26 ± 5	2.805 ± 0.005	5.2 ± 0.4
160	2.583 ± 0.002	6.2 ± 0.2	27 ± 5	2.811 ± 0.005	6.1 ± 0.4
205	2.585 ± 0.003	6.6 ± 0.2	26 ± 7	2.808 ± 0.006	5.7 ± 0.4
250	2.587 ± 0.003	6.9 ± 0.2	33 ± 7	2.809 ± 0.007	6.5 ± 0.6
295	2.587 ± 0.003	7.3 ± 0.2	35 ± 7	2.805 ± 0.006	6.6 ± 0.5

Table 5.8: Structural parameters obtained for the relaxed LEI sample.

dependence as confirmed by the k_3 values given in Table 5.9 which are the same within experimental uncertainty. In contrast, the static contribution to the third cumulant is zero within uncertainty for c-InP but ranges from 19 to 25×10^{-5} Å^3 for a-InP.

No comparison with c-InP is possible for the first NN In contribution (Fig. 5.9 (b) and (d)) since homopolar bonds do not exist in the crystalline zincblende phase. For both amorphous samples, the In-In Debye-Waller factors of the as-irradiated state are comparable to those of the relaxed phase. The

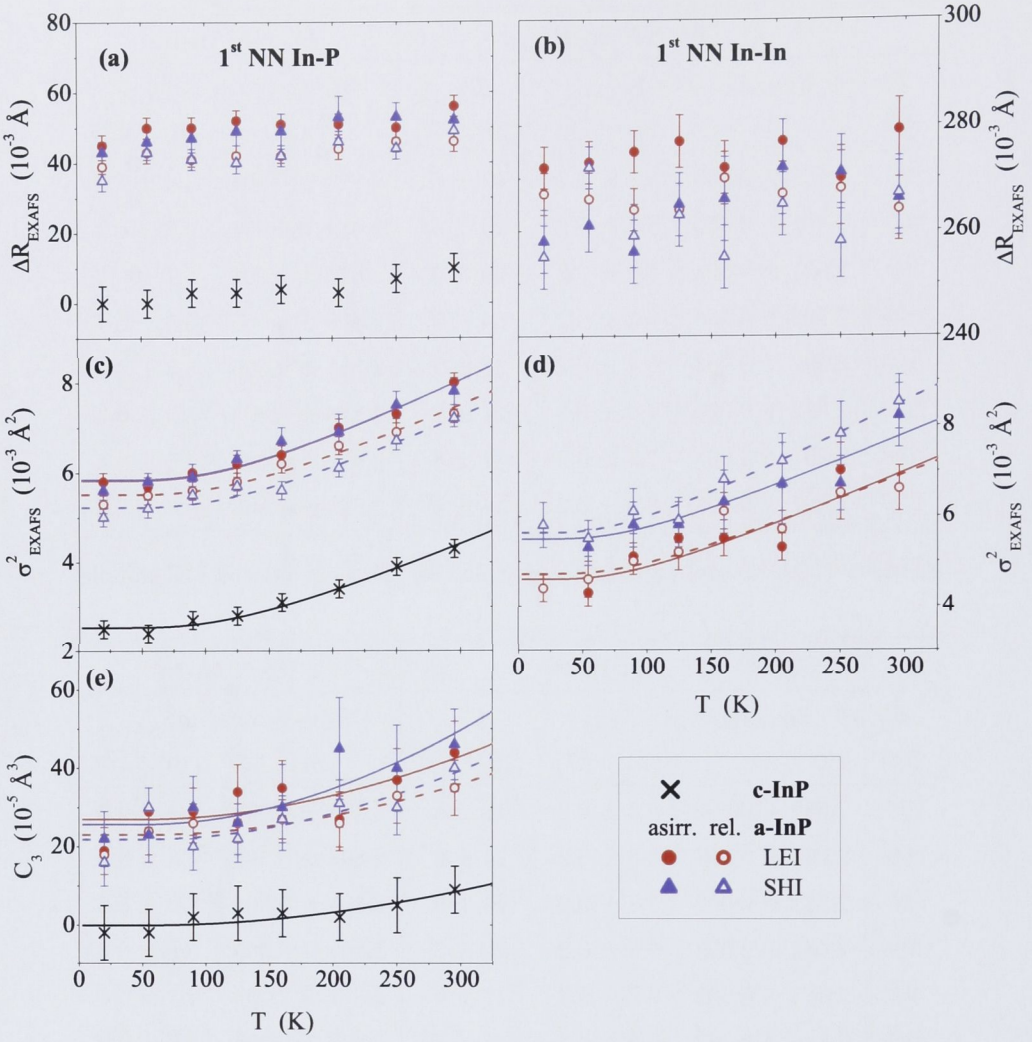

Figure 5.9: First NN structural parameters for a-InP versus temperature T. (a) and (b) show the interatomic distance $\Delta R_{\mathrm{EXAFS}} = R_{\mathrm{EXAFS}}(T) - 2.541$ Å, (c) and (d) plot the Debye-Waller factor $\sigma^2_{\mathrm{EXAFS}}$ for In-P and In-In, respectively. (e) displays the In-P third cumulant C_3. For In-P, the parameters of c-InP are also included for comparison. The lines give the corresponding Einstein fits.

SHI sample exhibits slightly higher values than the LEI sample as addressed in Section 4.4.1. The first NN In-In distances are similar and independent of temperature for all amorphous samples though the temperature evolution of $\Delta R_{\mathrm{EXAFS}}$ is not physically meaningful without a temperature-dependent C_3 included in the fit. The In-In C_3 values determined for the four a-InP samples at $T = 20$ K agree within experimental uncertainty (see Table 5.2).

1^{st} NN In-P		$\Theta_{E,\parallel}$ (K)	$\sigma^2_{static,\parallel}$ (10^{-3}Å^2)	k_3 (kgÅ^{-1}s^{-2})	$C_{3,static}$ (10^{-5}Å^3)
c-InP		392 ± 8	0.0 ± 0.2	120 ± 30	-1 ± 7
a-InP SHI	as-irrad.	370 ± 10	3.1 ± 0.2	230 ± 50	22 ± 6
	relaxed	382 ± 10	2.6 ± 0.2	200 ± 50	19 ± 6
a-InP LEI	as-irrad.	369 ± 10	3.1 ± 0.2	150 ± 50	25 ± 6
	relaxed	384 ± 10	2.9 ± 0.2	150 ± 50	21 ± 6

Table 5.9: Einstein temperature $\Theta_{E,\parallel}$, static contribution to the Debye-Waller factor $\sigma^2_{static,\parallel}$, anharmonic constant k_3 and static contribution to the third cumulant $C_{3,static}$ as determined for first NN In-P pairs in c-InP and a-InP.

1^{st} NN In-In		$\Theta_{E,\parallel}$ (K)	$\sigma^2_{static,\parallel}$ (10^{-3}Å^2)
a-InP SHI	as-irrad.	260 ± 20	3.9 ± 0.3
	relaxed	240 ± 20	3.9 ± 0.3
a-InP LEI	as-irrad.	260 ± 20	3.0 ± 0.3
	relaxed	270 ± 20	3.1 ± 0.3

Table 5.10: Einstein temperature $\Theta_{E,\parallel}$ and static contribution to the Debye-Waller factor $\sigma^2_{static,\parallel}$ as determined for first NN In-In pairs in c-InP and a-InP.

Comparing the Einstein temperatures $\Theta_{E,\parallel}$ of the amorphous samples with those obtained from the c-InP MSD and $MSRD_{\parallel}$ is instructive. Despite the subtle differences of the $\Theta_{E,\parallel}$ values given for In-P in Table 5.9 and discussed above, they are much closer to each other ($\sim 370 - 390$ K) than to the value obtained from MSD_{In+P} (~ 170 K). Similarly, $\Theta_{E,\parallel}$ for the first NN In-In pairs of the amorphous samples is much higher than the value for MSD_{In+In} (~ 260 K compared to ~ 110 K, respectively). Assuming the MSDs for both phases are of a similar order, vibrations of first NN atoms along the bond direction in the amorphous material must be correlated in a manner similar to that observed for c-InP with a strong (but not complete) in-phase-motion of the neighboring atoms.

Thus, comparing crystalline and amorphous phases, two main conclusions can be drawn:

(i) The thermal behavior ($\Theta_{E,\parallel}$, k_3) is similar for a-InP and c-InP whereas the structural disorder ($\sigma^2_{static,\parallel}$, $C_{3,static}$) is much higher in the amorphous phase than in the crystalline phase.

(ii) Relative motion of first NN atoms parallel to the bond direction is reduced by a similar amount for a-InP and c-InP when compared to the MSD.

Atomic motion is determined by the energy required to stretch and bend the bonds between atoms. The observed thermal and vibrational behavior thus suggests that the bonding character and hence the interatomic potential is similar for the two different phases.

5.6 Summary

Structural parameters of crystalline and amorphous InP have been determined using EXAFS measurements over a temperature range of 20 to 295 K. EXAFS is sensitive to the correlated motion of the atoms and thus yields valuable insight into the phase relation of atomic vibrations. Furthermore, by comparing XRD and EXAFS measurements, one can distinguish between vibrations parallel and perpendicular to the line connecting the absorber-backscatterer pair. For the first NN shell in c-InP, a strong vibrational anisotropy is observed where relative vibrations parallel to the bond are significantly smaller than the uncorrelated MSD determined by XRD while relative vibrations perpendicular to the bond are very similar. This is consistent with a strong (but not complete) in-phase-motion of the neighboring atoms along the bond direction and mostly uncorrelated vibrations perpendicular to it. Such behavior can be understood by considering the energy required for the two types of motion: Relative vibrations along the bond require bond stretching while relative vibrations perpendicular to the bond mainly change the bond angle and thus involve bond bending. For III-V semiconductors with the zincblende structure, bond bending is energeti-

cally favored over bond stretching with a ratio of $\sim 1/6$ for the corresponding force constants. A similar factor is obtained in the present study when comparing the force constants for relative vibrations perpendicular and parallel to the bond direction. The correlation of vibrations along the line of the absorber-backscatterer pair strongly decreases for the higher NN shells given changes of the bond angles alter the higher NN distances even if the first NN bond length remains unchanged. For the third NN shell, the amplitude of relative vibrations along the line of the two atoms already approaches the uncorrelated MSD. For a-InP, a strong increase of structural disorder is observed compared to c-InP, however, the temperature-dependent behavior and thus the thermally induced disorder are very similar for both phases. Furthermore, a strong reduction of first NN relative vibrations parallel to the bond is likely, similar to what is observed for c-InP. The similarities in vibrational behavior of crystalline and amorphous InP suggest that the bonding character is similar for the two phases despite their difference in structure.

CHAPTER 6

Composition-dependent structure of $Ga_{1-x}In_xP$ alloys

The interatomic distance distributions of the first three NN shells around Ga and In atoms in $Ga_{1-x}In_xP$ alloys were studied as a function of composition x. The mean value and standard deviation were determined for each atomic-pair. Different model calculations are discussed and compared to the experimental results. The extent of bond length and bond angle relaxation is evaluated.

6.1 Theoretical calculations

6.1.1 Bond length and bond angle relaxation

The two end-point binary compounds (AC and BC) of a ternary system $A_{1-x}B_xC$ often vary significantly in lattice constant due to the different size of their constituents. GaP and InP, for example, have lattice constants of 5.45 Å and 5.87 Å, respectively, corresponding to a relative difference of 8 % [78]. As a consequence, the question arises of how this lattice mismatch is accommodated in the atomic-scale structure of the ternary alloy.

Many materials, among them $Ga_{1-x}In_xP$ and $Ga_{1-x}In_xAs$ [78], exhibit a lattice constant that varies linearly with composition x between the two binary values, a behavior known as Vegard's Law [116]. The so-called virtual crystal approximation (VCA) hence assumes all atoms to occupy sites of an undis-

torted crystal lattice with the lattice constant determined by x [117]. All pairs of neighboring atoms have the same bond length and the bond angles remain unchanged. In contrast, Pauling and Huggins (P & H) assume the conservation of atomic radii which results in different bond lengths for the A-C and B-C pairs independent of x and identical to those of the binary compounds [118]. The lattice mismatch in this case is accommodated by adjustment of the bond angles. Figure 6.1 shows the A-C and B-C bond lengths, d_{AC} and d_{BC}, respectively, versus composition x for the VCA and P & H limits. As will be discussed in Section 6.2, experiments on a variety of III-V, II-VI and I-VII ternary alloys have shown the first NN distance distribution to be bimodal and closer to the P & H limit than the VCA (see Fig. 6.1). Considering the dilute limit of an impurity atom B in a crystal AC (denoted as AC:B), the dimensionless relaxation parameter ϵ is defined as the difference between the impurity bond length $d_{\mathrm{BC}}^{\mathrm{AC:B}}$ and the host bond length $d_{\mathrm{AC}}^{\mathrm{AC:B}} = d_{\mathrm{AC}}^{\mathrm{bin}}$ relative to the bond length difference of the two binaries: $\epsilon = (d_{\mathrm{BC}}^{\mathrm{AC:B}} - d_{\mathrm{AC}}^{\mathrm{bin}})/(d_{\mathrm{BC}}^{\mathrm{bin}} - d_{\mathrm{AC}}^{\mathrm{bin}})$ (see Fig. 6.1). The VCA thus corresponds to $\epsilon = 0$, the P & H limit to $\epsilon = 1$.

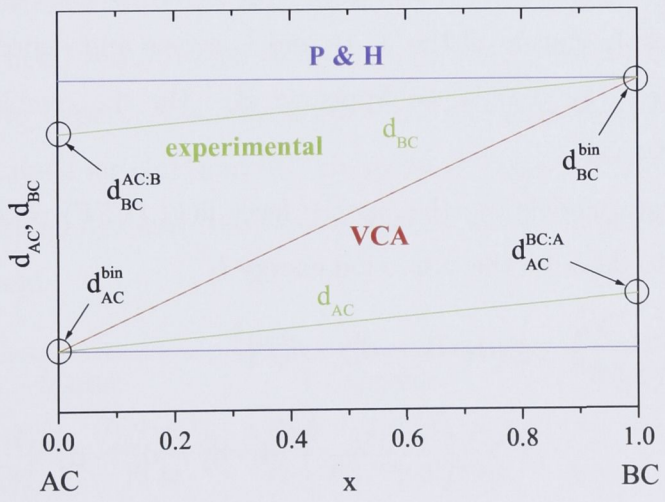

Figure 6.1: A-C and B-C bond lengths, d_{AC} and d_{BC}, respectively, versus composition x in the ternary alloy $A_{1-x}B_xC$. Shown are the VCA limit ($\epsilon = 0$), the P&H limit ($\epsilon = 1$) and typical experimental results ($\epsilon = 0.8$).

6.1.2 Models for the first NN shell

A number of models have been proposed to describe the first NN structure of ternary alloys, predominantly dating back to the 1980s [114,119–123]. Table 6.1 summarizes the main assumptions of the models described below and lists the ϵ values thus obtained.

Many of the early works only consider the dilute limit which has the advantage that the resulting symmetry around the impurity atom simplifies the calculation. Some authors then proposed a linear dependence for the first NN distance between the two end points as suggested by early experimental works [124]

$$\begin{aligned} d^{\mathrm{VCA}}(x) &= d_{\mathrm{AC}}^{\mathrm{bin}} + x\Delta d^{\mathrm{bin}} &&= d_{\mathrm{BC}}^{\mathrm{bin}} - (1-x)\Delta d^{\mathrm{bin}} \\ d_{\mathrm{AC}}(x) &= d_{\mathrm{AC}}^{\mathrm{bin}} + (1-\epsilon)x\Delta d^{\mathrm{bin}} &&= d^{\mathrm{VCA}}(x) - \epsilon x\Delta d^{\mathrm{bin}} \\ d_{\mathrm{BC}}(x) &= d_{\mathrm{BC}}^{\mathrm{bin}} - (1-\epsilon)(1-x)\Delta d^{\mathrm{bin}} &&= d^{\mathrm{VCA}}(x) + \epsilon(1-x)\Delta d^{\mathrm{bin}} \end{aligned} \tag{6.1}$$

with $d^{\mathrm{VCA}}(x)$ being the VCA distance at composition x and $\Delta d^{\mathrm{bin}} = d_{\mathrm{BC}}^{\mathrm{bin}} - d_{\mathrm{AC}}^{\mathrm{bin}}$.

The simplest model is that of Shih *et al.* [119]. It considers an impurity atom B and calculates the displacement of the surrounding first NN C atoms keeping all other atoms fixed. A harmonic potential is assumed for the first NN interactions with a geometric approximation to correlate the B-C and A-C distances. A single force constant is used for both bond types. The result is independent of the nature of the A, B, and C atoms and depends only on the crystal geometry (for details see Appendix B). For the zincblende structure, $\epsilon = 0.75$ is obtained.

More elaborate models use the valence force field (VFF) potential by Keating [112,113] to describe the distortion energy U

$$\begin{aligned} U = \sum_i \left(\frac{3\alpha_i}{8\left(d_i^{\mathrm{bin}}\right)^2} \right) \left[\mathbf{d}_i \cdot \mathbf{d}_i - \mathbf{d}_i^{\mathrm{bin}} \cdot \mathbf{d}_i^{\mathrm{bin}} \right]^2 \\ + \sum_{ij} \left(\frac{3\beta_{ij}}{8 d_i^{\mathrm{bin}} d_j^{\mathrm{bin}}} \right) \left[\mathbf{d}_i \cdot \mathbf{d}_j - \mathbf{d}_i^{\mathrm{bin}} \cdot \mathbf{d}_j^{\mathrm{bin}} \right]^2 . \end{aligned} \tag{6.2}$$

The sum of the first term includes all bond vectors $\mathbf{d}_i$ which are allowed to relax and represents the distortion energy due to bond stretching with the corresponding force constants α_i. α_i depends on the type of atoms that constitute

Model	Ref.	dilute limit	bond bending	2nd NN relaxation	A1	A2	GaP:In	InP:Ga
Shih *et. al*	[119]	yes	no	no	yes	yes	0.75	0.75
Martins & Zunger I	[120]	yes	yes	yes	yes	yes	0.63	0.73
Martins & Zunger II	[120]	yes	no	no	yes	yes	0.73	0.77
Chen & Sher	[114]	yes	yes	yes	yes	yes	0.70	0.80
Balzarotti *et. al*	[122]	no	no	no	no	no	0.78	0.73
Test 1		yes	no	no	yes	no	0.78	0.73
Test 2		yes	no	no	no	yes	0.73	0.77
Srivastava *et. al*	[123]	no	n/a	n/a	n/a	n/a	0.82	0.78
Cai & Thorpe I	[125]	no	yes	yes	yes	n/a	0.72	0.72
Cai & Thorpe II	[125]	no	yes	yes	yes	n/a	0.66	0.77
Silverman *et. al*	[30]	no	yes	yes	?	?	0.72	0.80

Table 6.1: Main assumptions of the different models discussed in Chapter 6.1 and ϵ values thus obtained. GaP:In refers to the case of In impurities in GaP, InP:Ga denotes Ga impurities in InP.

the particular bond and $\mathbf{d}_i^{\text{bin}}$ denotes the undistorted bond vector in the corresponding binary compound. The second sum includes all bond angles (formed by $\mathbf{d}_i$ and $\mathbf{d}_j$) which are allowed to relax and represents the distortion energy due to bond bending with the corresponding force constants β_{ij}. The bond stretching and bond bending force constants are determined for the binary compounds by fitting experimental elastic constants and bulk moduli [113,114,125]. The values obtained for GaP and InP are listed in Table 6.2. For application of Eq. (6.2) to ternary systems, the force constants of the corresponding binaries are typically used.

	Martin		Chen & Sher		Cai & Thorpe	
	α (N m^{-1})	β (N m^{-1})	α (N m^{-1})	β (N m^{-1})	α (N m^{-1})	β (N m^{-1})
GaP	47.32	10.44	44.764	10.737	44.50	10.69
InP	43.04	6.24	40.363	6.543	39.52	6.60

Table 6.2: Bond stretching and bond bending force constants, α and β, respectively, for GaP and InP by Martin [113], Chen and Sher [114] and Cai and Thorpe [125].

Martins and Zunger use the VFF potential described above to calculate the relaxation of first and second NN shells surrounding an impurity atom (Martins & Zunger I) [120]. Including the bond bending terms and relaxing the second NN shell change ϵ in opposite directions. Not including the two effects (Martins & Zunger II) thus gives a better result compared to experimental values than including only one. Both models use the following two approximations during the calculation: (A1) including only the harmonic terms of the potential and (A2) approximating the geometric relation between A-C and B-C distances (for details see Appendix B).

Chen and Sher consider not only the distortion energy due to bond stretching and bond bending but also "chemical" effects such as differences in binding energy and chemically driven charge redistribution [114]. Their extensive work further calculates various VFF models that differ in whether or not bond bending terms are included in the potential and in how the relaxation of higher NN shells is treated. For the case of In impurities in GaP, the ϵ values obtained with the different models vary by up to $\Delta\epsilon \sim 0.30$ illustrating the huge influence such choices have on the calculated results.

Balzarotti *et al.* calculate the ternary A-C and B-C distances for the entire compositional range of $Cd_{1-x}Mn_xTe$ and $Ga_{1-x}In_xAs$, using the Keating VFF potential (Eq. (6.2)) but without the bond bending terms and fixing the second NN atoms [121, 122]. In the dilute limit this model therefore corresponds to Martins & Zunger II except that the two approximations A1 and A2 are not applied. Following their methodology, the Ga-P and In-P distances were calculated in this work as a function of x (for details see Appendix B). To separately evaluate the influence of the two approximations A1 and A2, calculations have also been performed in the dilute limit including either one but not the other approximation (Test 1 and 2, respectively).

Srivastava *et al.* take a somewhat different approach using first-principles atomic pseudo-potentials but also calculate the first NN distances for the whole compositional range [123]. The corresponding ϵ values are 0.78 and 0.82 for Ga-P and In-P, respectively.

6.1.3 Models including the second NN shell

All the models discussed so far concentrate on the first NN interatomic distance with only a few simulations predicting multimodal distance distributions for the second NN shell [122]. Based on the Kirkwood VFF potential [126], Cai and Thorpe derived expressions for the mean value and the width of the first NN distance distributions and for the second NN distances of the various atomic pairs [125, 127]. Their *topological rigidity parameter* a^{**} depends on the bond stretching and bond bending force constants and is equivalent to ϵ. The $\epsilon = a^{**}$ values given in Table 6.1 are derived from the force constants given by Cai and Thorpe assuming mean values (Cai & Thorpe I) or taking individual values (Cai & Thorpe II) for Ga-P and In-P bonds. An alternative approach is to determine the ϵ value that best represents the first NN distances and to use this value to predict the second NN distances

$$\begin{aligned} d_{\mathrm{AA}}(x) &= \sqrt{\frac{8}{3}} d^{\mathrm{VCA}}(x) - \epsilon x \sqrt{\frac{3}{8}} \Delta d^{\mathrm{bin}} \\ d_{\mathrm{AB}}(x) &= \sqrt{\frac{8}{3}} d^{\mathrm{VCA}}(x) - \epsilon \frac{1}{2}(2x-1) \sqrt{\frac{3}{8}} \Delta d^{\mathrm{bin}} \\ d_{\mathrm{BB}}(x) &= \sqrt{\frac{8}{3}} d^{\mathrm{VCA}}(x) + \epsilon (1-x) \sqrt{\frac{3}{8}} \Delta d^{\mathrm{bin}}. \end{aligned} \tag{6.3}$$

The extensive work on $Ga_{1-x}In_xP$ by Silverman *et al.* starts from a thermodynamic description of the alloy structure including energetic and entropic terms with configurational, positional and vibrational contributions [30]. Among other properties, the first and second NN distance distributions as well as bond angle distributions are calculated.

6.2 Structure of ternary systems

6.2.1 First NN shell

A bimodal distance distribution with values much closer to the P & H limit than the VCA (see Fig. 6.1) has been observed in a large number of materials

such as $Ga_{1-x}In_xAs$ [124] and other III-V compounds [31, 128], various II-VI ternary alloys [31, 121, 122, 129] and in $K_{1-x}Rb_xBr$ and $RbBr_{1-x}I_x$ [130, 131]. The behavior of the III-V ternary alloys is characterized by $\epsilon = 0.75 - 0.80$ and a linear dependence of the bond lengths on composition x. In the sole brief report on $Ga_{1-x}In_xP$ alloys, Boyce and Mikkelsen give $\epsilon = 0.80 \pm 0.05$ and $\epsilon = 0.76 \pm 0.05$ for GaP:In and InP:Ga, respectively [31]. However, this study is limited to the first NN shell and no experimental data is available for the higher shells despite the extensive calculations by Silverman *et al.* [30] and the technological importance of $Ga_{1-x}In_xP$ alloys [5, 7, 8]. Compared to bulk material or relaxed layers, the situation is somewhat different in epitaxially grown strained thin films as shown by Woicik *et al.* for the case of buried $Ga_{1-x}In_xAs$ layers grown on InP [132, 133]. Here the first NN distances were observed to decrease with composition x and exhibited a slight nonlinear bowing of the curves. The authors conclude that the tetragonal distortion due to the external strain imposed by the substrate opposes the natural distance distortions due to alloying.

Considering bulk material again, the II-VI compounds show ϵ values similar to those of the III-V alloys but with a small deviation from the linear behavior [125]. The early works on the ionic alloys $K_{1-x}Rb_xBr$ and $RbBr_{1-x}I_x$ yielded significantly lower ϵ values of $0.55 - 0.65$ but also a linear dependence on composition [130]. In contrast, DiCicco *et al.* recently included deviations from the Gaussian distribution in the fits for $RbBr_{1-x}I_x$ and thus obtained $\epsilon = 0.75 - 0.80$ and considerable bowing of the curves [131].

6.2.2 Second NN shell

For $Ga_{1-x}In_xAs$, Mikkelsen and Boyce found that the As-As distance distribution is clearly bimodal (corresponding to a bridging Ga or In atom) and strongly deviates from the VCA [32]. In contrast, the cation-cation mean distances are much closer to the VCA. Nevertheless, they still systematically follow the relation Ga-Ga < Ga-In < In-In. Using high-energy XRD, Jeong *et al.* find the As displacements to be highly directional whereas the In and Ga displacements are

smaller and more isotropic [134]. Experimental results for other materials are also consistent with a strong distortion of the sublattice occupied by a single atom species whereas the mixed sublattice is close to the VCA albeit significantly broadened [128–130,135]. The effect of external strain on the second and third NN distances in $Ga_{1-x}In_xAs/InP$ and $InAs_xP_{1-x}/InP$ strained thin films has been studied by Tormen *et al.* [136] and Pascarelli *et al.* [135], respectively.

6.3 Experimental details

6.3.1 Sample preparation

$Ga_{1-x}In_xP/AlAs/GaAs$ heterostructures were fabricated by metal organic chemical vapor deposition, using GaAs substrates with a 10° miscut relative to the (100) direction to inhibit ordering of the mixed Ga/In sublattice. The composition of the $Ga_{1-x}In_xP$ layer was determined by XRD and RBS. Figure 6.2 shows the RBS backscattering yield Y versus channel number n measured in a random orientation for the three different stoichiometries grown (for experimental details on RBS measurements see Section 3.4). The spectra were fitted with

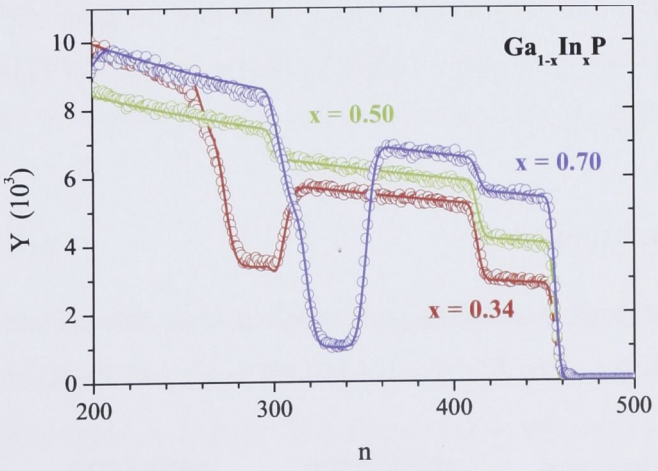

Figure 6.2: RBS backscattering yield Y versus channel number n measured in a random orientation for the three different $Ga_{1-x}In_xP$ stoichiometries grown (open symbols). Fitting (solid lines) was performed with the RUMP code [137]. The values obtained are listed in Table 6.3.

$Ga_{1-x}In_xP$	x	$1-x$	t_{GaInP} (μm)	t_{AlAs} (nm)
(1)	0.34 ± 0.02	0.66 ± 0.02	0.83 ± 0.01	20 ± 5
(2)	0.50 ± 0.02	0.50 ± 0.02	2.5	50
(3)	0.70 ± 0.03	0.30 ± 0.03	0.59 ± 0.01	30 ± 5

Table 6.3: $Ga_{1-x}In_xP$ composition x, $Ga_{1-x}In_xP$ layer thickness t_{GaInP} and AlAs layer thickness t_{AlAs} for the three different stoichiometries as obtained from the best fits (see Fig. 6.2). For stoichiometry (2) the thicknesses given are nominal values since they could not be determined from the fitting procedure.

the RUMP code [137] taking the In content and thickness of the $Ga_{1-x}In_xP$ layer, x and t_{GaInP}, respectively, and the thickness t_{AlAs} of the AlAs layer as variables. Table 6.3 lists the values determined from the best fits. The compositions of the three stoichiometries are $x = 0.34 \pm 0.02$, $x = 0.50 \pm 0.02$ and $x = 0.70 \pm 0.03$. RBS/c measurements also confirmed the crystallinity of the epitaxial layers.

To prepare samples suitable for EXAFS measurements, the $Ga_{1-x}In_xP$ layer was removed from the substrate by selective chemical etching. Figure 6.3 shows a schematic of the different preparation steps. The samples were first masked with wax to physically support the ternary layer. Then the AlAs layer was selectively dissolved in HF(48%):H_2O (1:10) over 24 hours. Afterwards, the wax was removed from the isolated $Ga_{1-x}In_xP$ layer and the films were finely crushed and mixed with boron nitride. Diluted powder samples of GaP and InP were prepared as references.

6.3.2 Measurement

EXAFS measurements were performed in transmission mode at the Photon Factory, Japan. The Ga K-edge (10.367 keV) and In K-edge (27.940 keV)

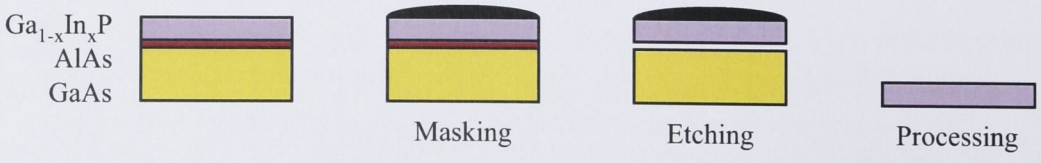

Figure 6.3: Schematic of the different sample preparation steps.

were measured at beam line 20B and NW10A, respectively. For both edges the measurement temperature was between 10 and 20 K.

6.4 Analysis

6.4.1 EXAFS spectra

The data were processed and analyzed using the IFEFFIT code [40] and the corresponding user interfaces ATHENA and ARTEMIS [41] as described in Section 2.4. FT was performed over a k-range of $k = 2 - 14$ Å for both edges. Figure 6.4 (a) shows the k^2-weighted EXAFS signal as a function of k for GaP and $Ga_{0.50}In_{0.50}P$ measured at the Ga K-edge. Figure 6.4 (b) shows the k-spectra for $Ga_{0.50}In_{0.50}P$ and InP measured at the In K-edge. The corresponding FTs are plotted in Fig. 6.4 (c) and (d).

For measurement at both edges, the peak at $R \sim 2$ Å in the FT spectra (due to scattering from first NN P atoms) is nearly identical for binary compound and ternary alloy. The other two ternary compositions exhibited similar behavior. In contrast, the contributions from the second and third NN shells in the region $R \sim 3 - 5$ Å change significantly with composition. For the binaries, scattering occurs at second NN Ga *or* In and third NN P atoms, whereas for the ternaries, scattering occurs at second NN Ga *and* In and third NN P atoms.

6.4.2 Fitting

Fitting of the first three shells was performed in radial space over a range of $R = 1.4 - 4.6$ Å and $R = 1.5 - 4.9$ Å for the Ga and In K-edges, respectively, using multiple k-weights = 1, 2, 3. The FEFF8 code [36] was used to calculate phase shifts and scattering amplitudes *ab initio* for GaP, InP and $Ga_{1-x}In_xP$. The amplitude reduction factor S_0^2 and the threshold energy E_0 were determined from the binary standards and were fixed while fitting the ternary samples. The coordination numbers N for the first and third NN shells (P) were set to the

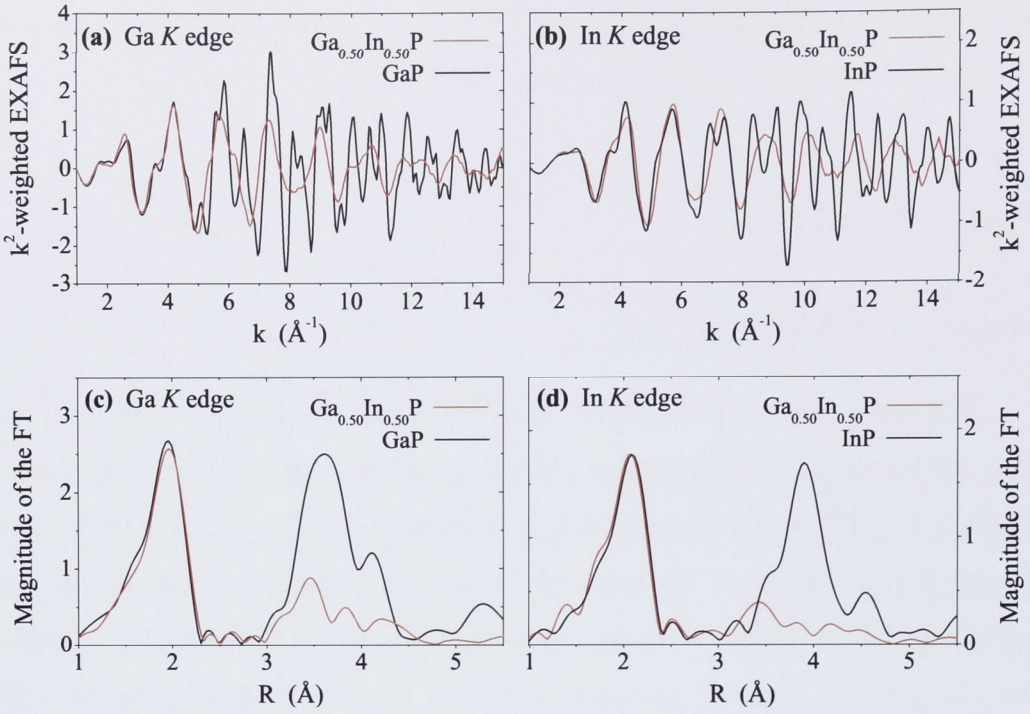

Figure 6.4: k^2-weighted EXAFS spectra versus the photoelectron wave number k for (a) GaP and $Ga_{0.50}In_{0.50}P$ measured at the Ga K-edge and (b) $Ga_{0.50}In_{0.50}P$ and InP measured at the In K-edge. (c), (d) Corresponding FTs as a function of the non-phase-corrected radial distance R.

zincblende values of four and twelve, respectively. For the second NN shell, the sum of Ga and In coordination numbers was fixed to the zincblende value of twelve while the ratio of the two was chosen according to the composition determined from RBS measurements (see Table 6.3). The interatomic distance R_{EXAFS} and Debye-Waller factor $\sigma^2_{\mathrm{EXAFS}}$ for each of the following scattering paths were floated: first NN P, second NN Ga, second NN In and third NN P, giving eight free parameters for each sample at each absorption edge measured. (Fits performed with the second NN Ga and In distances set equal in accordance with the VCA model were clearly inferior to those achieved with a bimodal distance distribution.) For the binary compounds only the corresponding second NN Ga *or* In scattering path was considered. The resulting best fits are shown in Fig. 6.5 (a) and (b) for measurement at the Ga and In K-edge, respectively, together with the back-transformed experimental data.

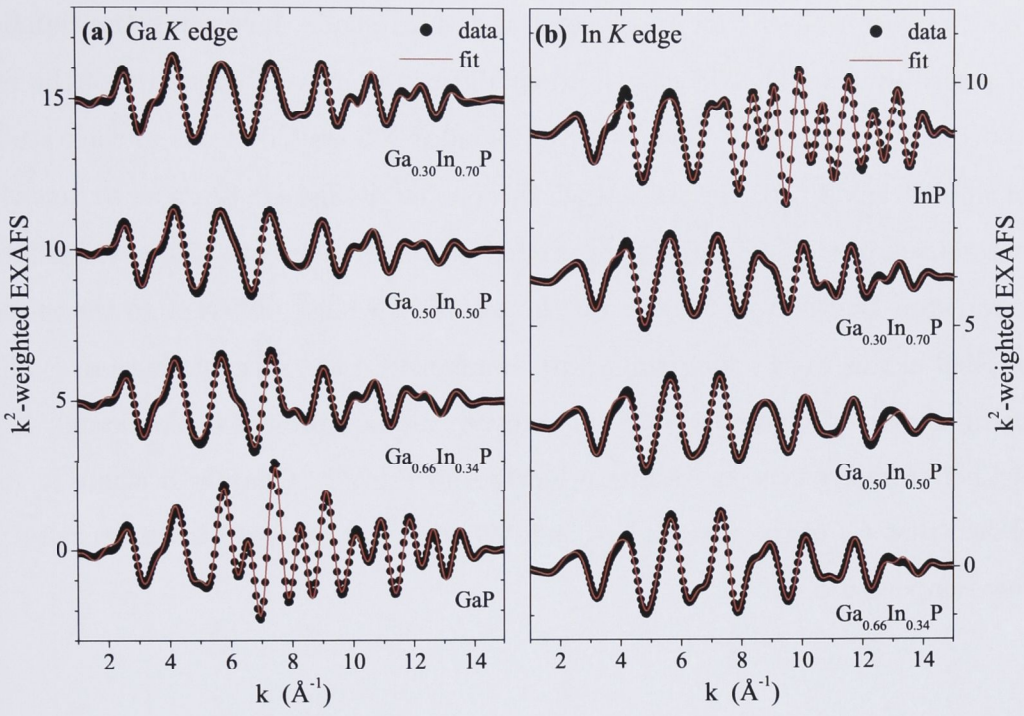

Figure 6.5: k^2-weighted back-transformed experimental data and best fits as a function of k for measurements taken at the (a) Ga K-edge and (b) In K-edge. Graphs for different stoichiometries are offset for clarity.

The fits described above were achieved with a single-scattering (SS) approximation. Though MS contributions are absent for a first-shell analysis of the zincblende structure, their potential influence must be considered for the analysis of higher shells such as that presented herein. It was found that the inclusion of MS contributions does not change the conclusions presented in Section 6.5. The negligible influence of MS contributions is attributed to the presence of bond length and bond angle distortion in the ternary alloys under study. MS is extremely sensitive to the local geometric arrangement and thus to structural disorder. In the ternary alloys studied in this work, the MS amplitudes are attenuated to a greater extent than SS amplitudes and to a greater extent than in binary compounds. Furthermore, the FEFF calculation does not take into account the composition-dependent bond length and bond angle changes, reducing the accuracy for the phase shift and amplitude of the MS paths. As described above, the fitting model contains three SS contributions (with two

free parameters each) for the second and third shell. Increasing the number of paths by including MS contributions did not improve the quality of the fits appreciably. (Note that Tormen *et al.* included MS contributions in their study of thin, strained $Ga_{1-x}In_xAs$ layers, however, no details are given as to how the parameters of the MS paths were treated [136]. Furthermore, the authors used a common Debye-Waller factor for the second NN shell, different to the model applied in this work.) Omitting third cumulants for the SS contributions is also justified given the number of free parameters already present in the model. It is further supported by the results presented for c-InP in Chapter 5 where it was shown that C_3 of the first and second NN shell was zero within uncertainty at low temperature.

6.5 Results and discussion

A schematic of the different first, second, and third NN atomic pairs in the $Ga_{1-x}In_xP$ ternary phase is shown in Fig. 6.6. The structural parameters obtained for the first three coordination shells are summarized in Tables 6.4 and 6.5 for measurements at the Ga and In K-edge, respectively. Coordination number N, interatomic distance R_{EXAFS} and Debye-Waller factor $\sigma^2_{\mathrm{EXAFS}}$ are listed for each of the four scattering contributions. Figure 6.7 plots R_{EXAFS} and $\sigma^2_{\mathrm{EXAFS}}$ as a function of composition x.

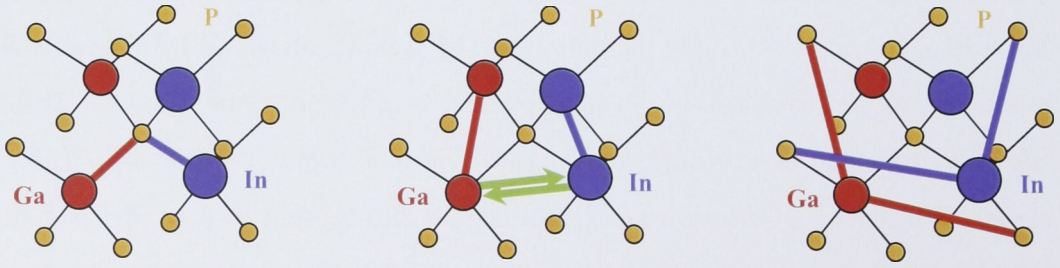

(a) First NNs (b) Second NNs (c) Third NNs

Figure 6.6: Interatomic distances (thick lines) of the possible absorber-backscatterer pairs in $Ga_{1-x}In_xP$ ternary alloys for measurement at the Ga and In K-edges.

Ga K-edge	**1^{st} NN P**			**2^{nd} NN Ga**			**2^{nd} NN In**			**3^{rd} NN P**		
	N	R_{EXAFS} (Å)	$\sigma^2_{\mathrm{EXAFS}}$ (10^{-3} Å^2)	N	R_{EXAFS} (Å)	$\sigma^2_{\mathrm{EXAFS}}$ (10^{-3} Å^2)	N	R_{EXAFS} (Å)	$\sigma^2_{\mathrm{EXAFS}}$ (10^{-3} Å^2)	N	R_{EXAFS} (Å)	$\sigma^2_{\mathrm{EXAFS}}$ (10^{-3} Å^2)
GaP	4	2.342 ± 0.006	2.7 ± 0.8	12	3.854 ± 0.005	3.8 ± 0.5				12	4.49 ± 0.01	4 ± 2
$Ga_{0.66}In_{0.34}P$	4	2.355 ± 0.004	2.7 ± 0.6	7.9	3.93 ± 0.02	7 ± 2	4.1	3.98 ± 0.03	7 ± 3	12	4.60 ± 0.02	11 ± 4
$Ga_{0.50}In_{0.50}P$	4	2.361 ± 0.004	3.0 ± 0.6	6.0	3.96 ± 0.02	8 ± 3	6.0	4.01 ± 0.02	7 ± 2	12	4.65 ± 0.03	12 ± 4
$Ga_{0.30}In_{0.70}P$	4	2.363 ± 0.005	2.8 ± 0.7	3.6	4.00 ± 0.04	7 ± 5	8.4	4.06 ± 0.02	7 ± 2	12	4.72 ± 0.03	11 ± 4

Table 6.4: Structural parameters for GaP and $Ga_{1-x}In_xP$ samples measured at the Ga K-edge. The coordination number N, interatomic distance R_{EXAFS} and Debye-Waller factor $\sigma^2_{\mathrm{EXAFS}}$ are listed.

In K-edge	**1^{st} NN P**			**2^{nd} NN Ga**			**2^{nd} NN In**			**3^{rd} NN P**		
	N	R_{EXAFS} (Å)	$\sigma^2_{\mathrm{EXAFS}}$ (10^{-3} Å^2)	N	R_{EXAFS} (Å)	$\sigma^2_{\mathrm{EXAFS}}$ (10^{-3} Å^2)	N	R_{EXAFS} (Å)	$\sigma^2_{\mathrm{EXAFS}}$ (10^{-3} Å^2)	N	R_{EXAFS} (Å)	$\sigma^2_{\mathrm{EXAFS}}$ (10^{-3} Å^2)
$Ga_{0.66}In_{0.34}P$	4	2.506 ± 0.003	2.4 ± 0.3	7.9	3.98 ± 0.01	5 ± 1	4.1	4.00 ± 0.02	4 ± 1	12	4.62 ± 0.02	11 ± 3
$Ga_{0.50}In_{0.50}P$	4	2.512 ± 0.003	2.4 ± 0.4	6.0	4.01 ± 0.02	8 ± 3	6.0	4.05 ± 0.02	8 ± 2	12	4.66 ± 0.03	13 ± 4
$Ga_{0.30}In_{0.70}P$	4	2.521 ± 0.003	2.5 ± 0.4	3.6	4.07 ± 0.03	7 ± 4	8.4	4.10 ± 0.01	7 ± 1	12	4.74 ± 0.02	11 ± 3
InP	4	2.531 ± 0.005	2.5 ± 0.7				12	4.157 ± 0.004	3.8 ± 0.4	12	4.85 ± 0.01	5 ± 2

Table 6.5: Structural parameters for InP and $Ga_{1-x}In_xP$ samples measured at the In K-edge. The coordination number N, interatomic distance R_{EXAFS} and Debye-Waller factor $\sigma^2_{\mathrm{EXAFS}}$ are listed.

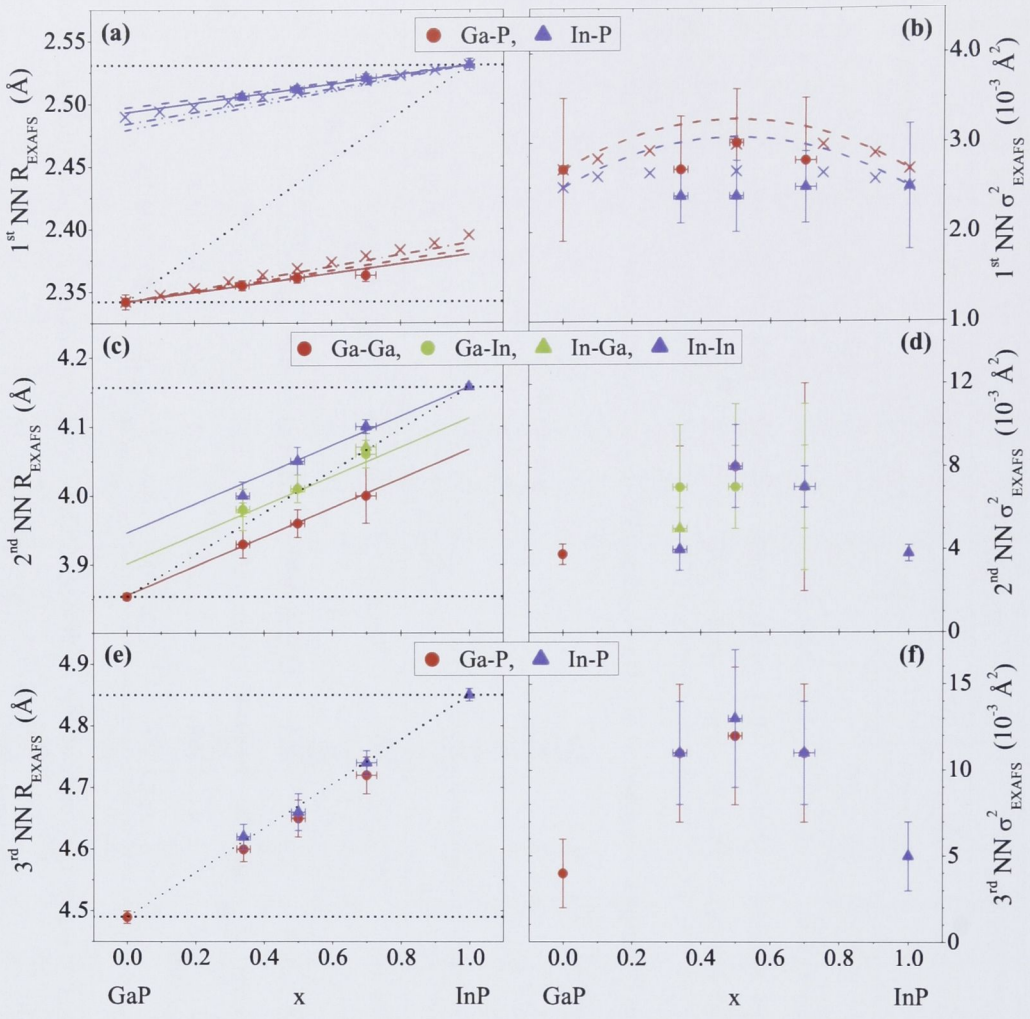

Figure 6.7: Structural parameters determined for GaP, InP and $Ga_{1-x}In_xP$ as a function of composition x. Shown are the interatomic distances R_{EXAFS} and Debye-Waller factors $\sigma^2_{\mathrm{EXAFS}}$ for scattering at the first NN P ((a) and (b)), at the second NN Ga or In ((c) and (d)) and at the third NN P ((e) and (f)) atoms. The dotted lines in panels (a), (c) and (e) represent the corresponding VCA and P & H limits. The solid lines in panel (a) represent the best linear fits of the data yielding $\epsilon = 0.80 \pm 0.04$ for both Ga-P and In-P pairs. *Theoretical calculations*: The calculations by Srivastava *et al.* (dashed line), Shih *et al.* (dashed-dotted line), Silverman *et al.* (dash-double-dotted line) and Balzarotti *et al.* (crosses) are shown in panel (a). The solid lines in panel (c) represent the calculations according to Cai & Thorpe using $\epsilon = 0.80$ determined from panel (a). Panel (b) gives the calculations by Cai & Thorpe again with $\epsilon = 0.80$ (dashed lines) and by Silverman *et al.* (crosses). For discussion of the various calculations see Section 6.1.

6.5.1 First NN distance distribution

The first NN distance distribution is clearly bimodal (Fig. 6.7 (a)). The values for Ga-P and In-P mean distances exhibit a linear dependence on the composition x and are much closer to the corresponding binaries values than to the VCA. A linear fit yields $\epsilon = 0.80 \pm 0.04$ for both atomic pairs which agrees very well with the results of other III-V bulk alloys including the previous report for $Ga_{1-x}In_xP$ (see Section 6.2) [31]. The Debye-Waller factors are constant within experimental uncertainty (Fig. 6.7 (b)) similar to the findings for other III-V and II-VI alloys [31,32,122,128]. The first NN shell of the ternary phase thus resembles a mixture of the binary atomic environments, having two distance distributions corresponding to Ga-P and In-P bonds with mean values and widths similar to those of the binary compounds.

Table 6.1 shows that all reported models yield ϵ values between 0.63 and 0.82 and thus, on average, slightly underestimate the experimentally determined extent of relaxation. Excellent agreement is found with the calculations by Srivastava *et al.* [123]. Comparing the different models, the following conclusions can be drawn:

(i) Using the different values of force constants reported in the literature [113, 114,125] for any given model yields only small differences in ϵ (≤ 0.02) that are much smaller than the variation due to the use of different models.

(ii) The choice of approximations is the most crucial factor to the resulting ϵ value. As discussed by Martins and Zunger, including neither the bond bending terms in the VFF potential nor the relaxation of the second NN shell gives better results than including only one of the two effects. Using a harmonic approximation to the VFF potential (A1) does not influence the calculated ϵ values (Test 1). In contrast, approximating the geometric relationship between the A-C and B-C distances (A2) not only changes the absolute values of ϵ but also the ratio between the values for GaP:In and InP:Ga (Test 2). As Cai and Thorpe argue, the relaxation in semiconductors extends out to a long range. Nevertheless, the simple models that only

consider relaxation of the first NN shell (Shih *et al.*, Martins & Zunger II and Balzarotti *et al.*) yield ϵ values similar to those of the more complex calculations. It is therefore very difficult to judge the appropriateness of a certain approximation without performing the complete calculation and comparing the result with experiments such as those presented here.

(iii) Most models give different ϵ values for GaP:In and InP:Ga due to the different force constants of the two binaries. This is not observed experimentally. The actual geometric arrangement determined by the energy balance of bond stretching versus bond bending appears insensitive to the difference in force constants. Instead, energy minimization favors a linear dependence of the lattice constant on composition x. In strained epitaxially grown thin films, on the other hand, the lattice constant is not free to adjust according to alloy composition and hence Vegard's Law is not obeyed. Under such circumstances the different force constants of the two binaries lead to a bowing of the curves as demonstrated by Woicik *et al.* [132, 133] for the case of strained $Ga_{1-x}In_xAs$ thin films.

Cai and Thorpe [125] and Silverman *et al.* [30] both predict the standard deviation of the first NN distance distribution. The values are calculated for a temperature of 0 K, yielding zero for the two binaries. It can therefore be viewed as the purely static contribution to the Debye-Waller factor. Zero-point motion leads to a small but positive contribution to the Debye-Waller factor even at 0 K. The measurements presented herein were performed at 10 - 20 K and thus a thermal contribution is to be expected. The resulting Debye-Waller factors for the binaries are small but non-zero. To compare the experimental results with the calculations, the binary value (determined experimentally) has been added to all calculated values. The predictions by Silverman *et al.* are closer to the experimental results than those of Cai and Thorpe (assuming $\epsilon = a^{**} = 0.80$), though both are within experimental uncertainty.

6.5.2 Second and third NN distance distributions

Similar to the first NN shell, the second NN distance distribution also features different mean values for the different atomic pairs (see Fig. 6.6 (b)). As apparent in Fig. 6.7 (c), the Ga-Ga distance is smaller than the Ga-In distance which, in turn, is smaller than the In-In distance, very similar to what is reported on $Ga_{1-x}In_xAs$ by Mikkelsen and Boyce [32]. The values for the mixed pair determined at either the Ga or In K-edge agree very well. The interatomic distances of all three pairs follow a linear dependence in x and have a similar slope. The second NN distance distribution thus still exhibits discrete mean distances corresponding to the different cation-cation pairs but the values are now much closer to the VCA. There is no obvious trend in the Debye-Waller factors when comparing the different atomic pairs (Fig. 6.7 (d)) but there is a significant increase for the ternaries compared to the binaries. Such findings are consistent with the mostly isotropic displacements of the mixed sublattice proposed by Jeong *et al.* [134] which would yield an average distance close to the VCA but a significantly broadened distribution.

As discussed in the previous section, most models give similar ϵ values despite their very different assumptions. The model by Cai and Thorpe is the only one that also derives expressions for the mean second NN distances [125]. As for $Ga_{1-x}In_xAs$, the predictions agree very well with the measurements when $\epsilon = a^{**} = 0.80$, determined from a best fit of the first NN distances, is used (see Fig 6.7 (c)). The experimental findings are also in good qualitative agreement with the calculations by Silverman *et al.* [30]. Both the relation between the distances of the three different pairs, namely Ga-Ga < Ga-In < In-In, as well as the broadening of the distributions from the binaries towards $x = 0.5$ can be clearly seen in Fig. 6.7 (c) and (d).

The mean third NN distance of the Ga-P pair is still systematically lower than that of the In-P pair but the difference is now within experimental uncertainty (Fig. 6.7 (e)). The values show a linear dependence on x and agree well with the VCA. The Debye-Waller factors for both atomic pairs are nearly

identical for the ternaries and show a strong increase compared to GaP and InP (Fig. 6.7 (f)). Averaging over various local arrangements, such as different bridging second NNs (see Fig. 6.6 (c)), thus makes the VCA a very good approximation for the interatomic distance of the third NN shell. The width of the distribution, though, is significantly broadened in the ternary alloys due to this averaging process.

6.5.3 Tetrahedral bond angles

Using the first and second NN distances, the tetrahedral bond angles θ and the complementary bond angles ϕ were calculated. Figure 6.8 shows a schematic of the different angles evaluated. The values for the tetrahedral bond angles $\sphericalangle$ Ga-P-Ga, $\sphericalangle$ Ga-P-In and $\sphericalangle$ In-P-In are listed in Table 6.6 and plotted as a function of composition x in Fig. 6.9 (a). The corresponding complementary angles $\sphericalangle$ P-Ga-Ga, $\sphericalangle$ P-Ga-In, $\sphericalangle$ P-In-Ga and $\sphericalangle$ P-In-In are given in Table 6.7 and Fig. 6.9 (b).

Considering the tetragonal bond angles with a central P atom, the two binary values agree very well though they are slightly higher than the ideal zincblende value of 109.5°. Accordingly, the binary ϕ values are slightly lower than the

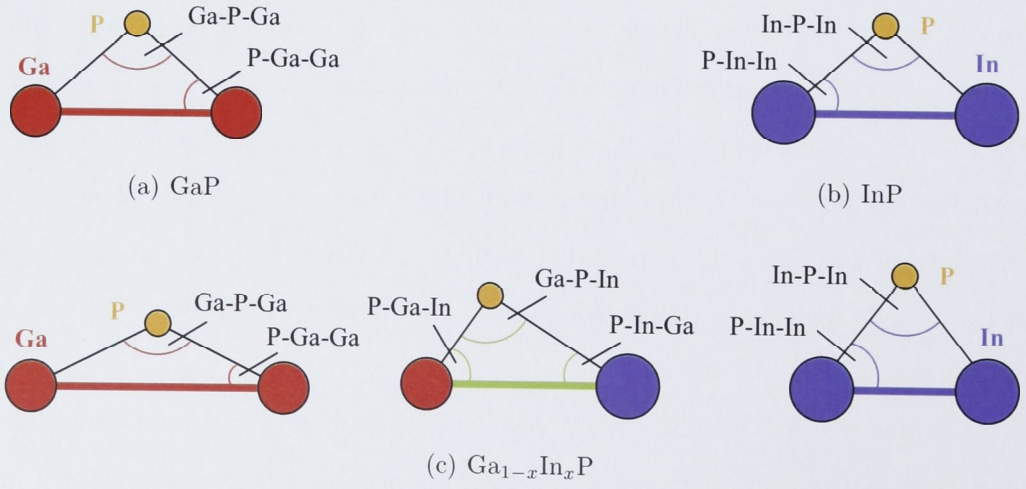

(a) GaP

(b) InP

(c) $Ga_{1-x}In_xP$

Figure 6.8: Schematic of the different bond angles evaluated from the first and second NN distances.

θ (degree)	$\sphericalangle$ Ga-P-Ga	$\sphericalangle$ Ga-P-In	$\sphericalangle$ In-P-In
GaP	110.7 ± 0.6		
$In_{0.34}Ga_{0.66}P$	113.1 ± 1.2	109.9 ± 0.7	105.9 ± 0.9
$In_{0.50}Ga_{0.50}P$	114.0 ± 1.2	110.7 ± 1.1	107.4 ± 1.0
$In_{0.70}Ga_{0.30}P$	115.6 ± 2.2	112.4 ± 1.1	108.8 ± 0.6
InP			110.4 ± 0.5

Table 6.6: Tetrahedral bond angle θ with P as central atom for GaP, InP and $Ga_{1-x}In_xP$.

zincblende value of 35.3°. This slight difference could be attributed to offsets in the absolute interatomic distance determination during the fitting, but it is clearly small compared to the change due to composition in the ternary alloy. As discussed in the previous section, the second NN distances follow the VCA more closely than the first NN distances. With increasing x the Ga-Ga distance thus increases to a greater relative extent than the Ga-P distance, leading to a larger $\sphericalangle$ Ga-P-Ga tetrahedral bond angle and a smaller $\sphericalangle$ P-Ga-Ga complementary bond angle compared to the ideal zincblende values (see Fig. 6.8). Similarly, $\sphericalangle$ In-P-In is expected to decrease from the ideal value with decreasing x while $\sphericalangle$ P-In-In is expected to increase. Such behavior is readily apparent in Fig. 6.9 (a) and (b). In the mixed triangle, the bond angle ϕ with a central Ga atom, $\sphericalangle$ P-Ga-In (see Fig. 6.8), is very close to the value of $\sphericalangle$ P-In-In in the "In triangle". Similarly, $\sphericalangle$ P-In-Ga is only slightly higher than $\sphericalangle$ P-Ga-Ga. Thus, the complementary bond angle ϕ is determined by the length of the opposite

ϕ (degree)	$\sphericalangle$ P-Ga-Ga	$\sphericalangle$ P-Ga-In	$\sphericalangle$ P-In-Ga	$\sphericalangle$ P-In-In
GaP	34.6 ± 0.3			
$In_{0.34}Ga_{0.66}P$	33.5 ± 0.6	36.3 ± 0.3	33.8 ± 0.3	37.1 ± 0.5
$In_{0.50}Ga_{0.50}P$	33.0 ± 0.6	35.9 ± 0.6	33.4 ± 0.5	36.3 ± 0.5
$In_{0.70}Ga_{0.30}P$	32.2 ± 1.1	35.0 ± 0.6	32.6 ± 0.6	35.6 ± 0.3
InP				34.8 ± 0.2

Table 6.7: Complementary bond angle ϕ with either Ga or In as central atom for GaP, InP and $Ga_{1-x}In_xP$.

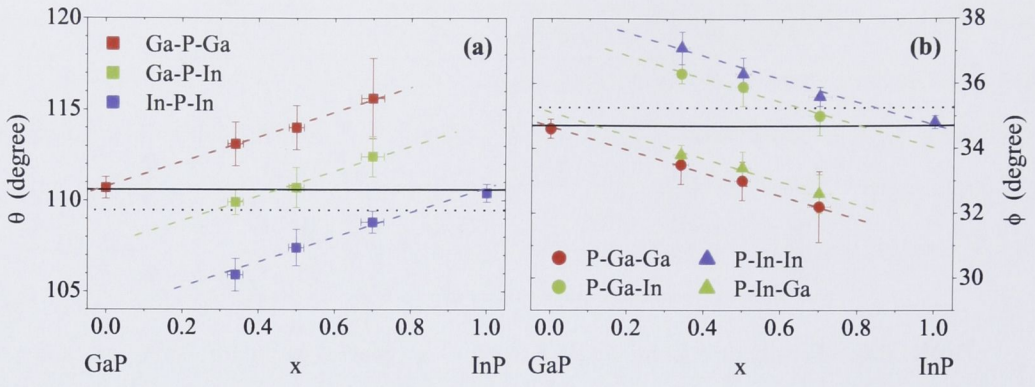

Figure 6.9: Values of the (a) tetrahedral bond angles θ and (b) complementary bond angles ϕ as a function of composition x. The solid line indicates the binary value determined herein whereas the dotted line represents the ideal zincblende value. The dashed lines in each panel are parallel and serve as a guide to the eye. A schematic of the different angles is shown in Fig. 6.8.

bond, that is by the type of the *other* cation in the triangle. Furthermore, the values for all angles show a linear dependence on x with one slope for all θ and another one slope for all ϕ. The change of the tetrahedral and complementary bond angles with composition clearly demonstrates that lattice mismatch is accommodated in the ternary alloy by adjusting both bond lengths *and* bond angles.

The distribution of tetrahedral bond angles with a central P atom shown by Silverman *et al.* does not differentiate between the various possible cation combinations (Ga-Ga, Ga-In or In-In) [30]. The mean value is relatively composition independent and agrees well with the ideal zincblende value. Assuming, as suggested by Fig. 6.9 (a), that the linear slope is the same for all three types of tetragonal angles, let this slope be $\Delta\theta$. Furthermore, $\sphericalangle$ Ga-P-Ga $(x = 0)$=$\sphericalangle$ Ga-P-In $(x = 0.5)$=$\sphericalangle$ In-P-In $(x = 1)$=θ^{bin}, where θ^{bin} denotes the binary value. The probability of finding a Ga or In atom on a particular site of the mixed sublattice in $Ga_{1-x}In_xP$ is $(1-x)$ or x, respectively. Hence, the probabilities for a "Ga triangle", a mixed triangle or an "In triangle" are $(1-x)^2$, $2x(1-x)$ or x^2, respectively. The weighted average $\sphericalangle$ i-P-i (x) over all tetragonal bond angles with a central P atom is then indeed θ^{bin} and independent of composition x:

$$\begin{aligned} \sphericalangle \text{Ga-P-Ga}\,(x) &= \theta^{\text{bin}} + x\Delta\theta \\ \sphericalangle \text{Ga-P-In}\,(x) &= \theta^{\text{bin}} + \tfrac{1}{2}(2x-1)\Delta\theta \\ \sphericalangle \text{In-P-In}\,(x) &= \theta^{\text{bin}} - (1-x)\Delta\theta \end{aligned} \tag{6.4}$$

and thus

$$\begin{aligned} \sphericalangle \text{i-P-i}\,(x) &= (1-x)^2 \sphericalangle \text{Ga-P-Ga}\,(x) + 2x(1-x) \sphericalangle \text{Ga-P-In}\,(x) \\ &\quad + x^2 \sphericalangle \text{In-P-In}\,(x) \\ &= \theta^{\text{bin}}\left[(1-x)^2 + 2x(1-x) + x^2\right] \\ &\quad + \Delta\theta\left[(1-x)^2 x + 2x(1-x)\tfrac{1}{2}(2x-1) - x^2(1-x)\right] \\ &= \theta^{\text{bin}}. \end{aligned} \tag{6.5}$$

Given the small change in mean first NN distances with composition, the fact that the higher NN shells follow Vegard's Law much more closely can only be realized by adjusting the tetrahedral bond angles. Bond bending is thus energetically favored over bond stretching and the lattice mismatch is mostly accommodated by bond angle relaxation rather than bond length relaxation. A similar behavior is observed in epitaxially grown strained thin films of $Ga_{1-x}In_xAs$ [136], $InAs_xP_{1-x}$ [135] and $Si_{1-x}Ge_x$ [138]. The first NN distances remain close to those of the binary compounds and the tetragonal strain is accommodated primarily by bond angle distortions.

6.6 Summary

EXAFS was used to measure the local atomic environment around Ga and In atoms in $Ga_{1-x}In_xP$ alloys as a function of composition x. The interatomic distance and Debye-Waller factor were determined for all atomic pairs in the first three NN shells. The first NN distance distribution is bimodal. The mean value for each contribution (Ga-P and In-P) is composition dependent though similar to the distances in the corresponding binaries. A relaxation parameter of $\epsilon = 0.80 \pm 0.04$ together with a linear dependence on x describes well the interatomic distances of both pairs. Most theoretical models slightly underestimate ϵ

but excellent agreement is found with the calculations by Srivastava *et al.* [123]. The second NN distance distribution exhibits three peaks corresponding to Ga-Ga, Ga-In and In-In. The mean distances are closer to the VCA than for the first NN shell but the widths are significantly increased compared to the two binaries. Using $\epsilon = a^{**} = 0.80$ determined from the first NN distances, the expressions derived by Cai and Thorpe [125] for the second NN distances agree well with the experimental values. The behavior of $Ga_{1-x}In_xP$ is thus similar to that of $Ga_{1-x}In_xAs$ for which the distances of all atomic pairs within the first and second NN shell are also well represented by the model of Cai and Thorpe when using the same value of $\epsilon = a^{**} = 0.80$. The results presented here also agree with the extensive calculations by Silverman *et al.* for $Ga_{1-x}In_xP$ alloys [30]. For the third NN shell, the mean Ga-P distance is still systematically smaller than that of In-P but both agree well with the VCA within experimental uncertainty. Thus, the averaging over various local atomic arrangements makes the VCA a valid approximation for the third NN shell but the distribution is significantly broader compared to the binary compounds. The tetrahedral bond angle around a central P atom changes linearly with composition x increasing ($\sphericalangle$ Ga-P-Ga) or decreasing ($\sphericalangle$ In-P-In) by $\sim 6.5°$ with respect to the binary value. This clearly demonstrates that the lattice mismatch is accommodated in the ternary structure by both bond length and bond angle relaxation though primarily via the latter.

Chapter 7

Conclusion

In this work, structural and thermal properties of III-V binary and ternary semiconductors and their response to swift heavy ion (SHI) irradiation were studied. Damage formation due to 185 MeV Au irradiation of InP, InAs, GaP, GaAs and the related ternary alloys $Ga_{0.50}In_{0.50}P$ and $Ga_{0.47}In_{0.53}As$ was assessed with Rutherford backscattering spectroscopy in channeling configuration and transmission electron microscopy. The atomic-scale structure of crystalline InP, amorphous InP and crystalline $Ga_{1-x}In_xP$ alloys was measured using extended x-ray absorption fine structure (EXAFS) spectroscopy. The amorphous phase of InP was produced by ion irradiation with either dominant electronic or nuclear energy deposition. Thermal vibrations in InP were studied using temperature-dependent EXAFS measurements.

Comparing crystalline and amorphous InP, the lack of long-range order and the increase of structural disorder in the first nearest neighbor (NN) environment are readily apparent for the amorphous phase. The most significant difference in short-range order compared to crystalline material is the presence of $\sim 15\,\%$ In-In bonds in the amorphous phase. Ion irradiation with dominant electronic or nuclear energy deposition produces the same amorphous phase structure despite the fundamentally different energy transfer mechansisms. Such findings are consistent with simulations predicting a quench from the melt as a common amorphization process for both regimes.

For the other III-V semiconductors, the processes governing damage formation under SHI irradiation are less understood. The Gibbons overlap model fails

to describe the apparent saturation of damage for InAs and $Ga_{0.47}In_{0.53}As$ and a combination of SHI induced damage formation and annealing is thus proposed. Despite the simplicity of the model, it describes the behavior of the different materials well. The proposed annealing of damaged zones could proceed via solid phase epitaxial regrowth stimulated by the heat dissipated from the ion trajectory and/or by energetic electrons created during the ion passage. Given the extremely low defect concentration observed for GaP and GaAs, the electronic energy deposition associated with 185 MeV Au irradiation may be insufficient to produce a molten track in these two materials consistent with simulations for Si and Ge. In contrast, the simulated temperature within the track in InP well exceeds the melting point. Similar simulations could help to establish whether the requirements for damage formation are satisfied for a given combination of material and irradiation conditions. Further systematic studies of the parameter space governing the irradiation might also contribute to a more comprehensive understanding of the processes involved. For example, ion flux and irradiation temperature will both influence the microscopic temperature distribution inside the material which should affect damage formation and annealing. Studying ternary alloys such as $Ga_{1-x}In_xP$, the most obvious question is that of how the response changes from being easily damaged (InP) to being radiation resistant (GaP). If this change in behavior could be correlated to a change in material properties this would be a significant step in identifying what governs the response to SHI irradiation. Similarly, the applicability of the modified model to the damage formation behavior for other ternary compositions should be tested.

$Ga_{1-x}In_xP$ alloys form the zincblende structure with a lattice constant equal to the average of the values of the binary compounds weighted according to the ternary composition. Locally, the lattice mismatch between InP and GaP can be accommodated by bond length relaxation and/or bond angle relaxation. In this work, it has been shown that the Ga-P and In-P bond lengths in the ternary alloy remain close to the binary values while a significant change in bond angles was observed consistent with the fact that in III-V semiconductors bond bending

is energetically favored over bond stretching. Lattice mismatch in $Ga_{1-x}In_xP$ is thus accommodated by both bond length and bond angle relaxation although primarily via the latter. In contrast to the first NN environment, the higher shells are well represented by the virtual crystal approximation due to the fact that a change in bond angle alters the higher NN distances even if the first NN distances remain the same.

The observed preference of bond bending over bond stretching also governs the thermal vibrations in crystalline InP. First NN atoms are characterized by a strong in-phase-motion parallel to the bond since relative vibrations in this direction require energetically unfavorable bond stretching. In contrast, relative vibrations perpendicular to the bond mainly involve energetically favorable bond bending leading to a largely uncorrelated motion in this direction. As mentioned above, changing the bond angle alters the higher NN distances. The correlation of motion parallel to the line connecting the atomic pair thus rapidly decreases with increasing number of bridging atoms between absorber and backscatterer. Hence, the relative thermal vibrations observed for first and higher NN atoms in crystalline InP are well explained by the differences in energy required for bond bending and bond stretching. Amorphous InP is characterized by significantly increased static disorder but very similar thermal disorder when compared to the crystalline phase. The results also suggest the first NN motion parallel to the bond direction to have a similar degree of correlation in both phases. If atomic vibrations are governed by the energy required for certain types of motion, these findings indicate that the bonding character is similar in both phases despite their difference in structure. A similar temperature-dependent EXAFS investigation of other III-V compounds should help to establish the influence of the difference in mass, size and ionicity of the two atomic constituents on the vibrational behavior. For this purpose, measurements on GaP, GaAs and GaSb are currently under way.

References

[1] D. C. Koningsberger and R. Prins, *X-ray Absorption*, Wiley, New York, 1988.

[2] J. J. Rehr and R. C. Albers, Rev. Mod. Phys. **72**, 621 (2000).

[3] http://www.ioffe.rssi.ru/SVA/NSM/Semicond/.

[4] E. F. Schubert, *Light Emitting Diodes*, Cambridge Univeristy Press, Cambridge, 2006.

[5] S. Mokkapati and C. Jagadish, Materials Today **12**, 22 (2009).

[6] S. Prasad, Materials Today **12**, 34 (2009).

[7] H. Cotal, C. Fetzer, J. Boisvert, G. Kinsey, R. King, P. Hebert, H. Yoon, and N. Karam, Energy Environ. Sci. **2**, 174 (2009).

[8] M. Bosi and C. Pelosi, Prog. Photovolt. **15**, 51 (2007).

[9] P. L. Dreike, D. M. Fleetwood, D. B. King, D. C. Sprauer, and T. E. Zipperian, IEEE Trans. Comp. Pack. Manufact. Tech. A **17**, 594 (1994).

[10] E. Wendler, T. Opfermann, and P. I. Gaiduk, J. Appl. Phys. **82**, 5965 (1997).

[11] E. Wendler, B. Breeger, C. Schubert, and W. Wesch, Nucl. Instr. Meth. B **147**, 155 (1999).

[12] W. Wesch, A. Kamarou, E. Wendler, and S. Klaumünzer, Nucl. Instr. Meth. B **242**, 363 (2006).

[13] E. M. Bringa and R. E. Johnson, Phys. Rev. Lett. **88**, 165501 (2002).

[14] G. Schiwietz, K. Czerski, M. Roth, F. Staufenbiel, and P. Grande, Nucl. Instr. Meth. B **226**, 683 (2004).

[15] S. Klaumünzer, in *Ion Beam Science: Solved and Unsolved Problems*, page 293, The Royal Danish Academy of Sciences and Letters, Copenhagen, 2006.

[16] C. J. Glover, M. C. Ridgway, K. M. Yu, G. J. Foran, T. W. Lee, Y. Moon, and E. Yoon, Appl. Phys. Lett. **74**, 1713 (1999).

[17] G. de M. Azevedo, M. C. Ridgway, K. M. Yu, C. J. Glover, and G. J. Foran, Nucl. Instr. Meth. B **190**, 851 (2002).

[18] E. P. O'Reilly and J. Robertson, Phys. Rev. B **34**, 8684 (1986).

[19] G. de M. Azevedo, C. J. Glover, M. C. Ridgway, K. M. Yu, and G. J. Foran, Phys. Rev. B **68**, 115204 (2003).

[20] M. C. Ridgway, C. J. Glover, K. M. Yu, G. J. Foran, C. Clerc, J. L. Hansen, and A. Nylandsted-Larsen, Phys. Rev. B **61**, 12586 (2000).

[21] C. J. Glover, M. C. Ridgway, K. M. Yu, G. J. Foran, D. Desnica-Frankovic, C. Clerc, J. L. Hansen, and A. Nylandsted-Larsen, Phys. Rev. B **63**, 073204 (2001).

[22] G. de M. Azevedo, C. J. Glover, K. M. Yu, G. J. Foran, and M. C. Ridgway, Nucl. Instr. Meth. B **206**, 1024 (2003).

[23] P. Fornasini, S. a Beccara, G. Dalba, R. Grisenti, A. Sanson, M. Vaccari, and F. Rocca, Phys. Rev. B **70**, 174301 (2004).

[24] G. Dalba, P. Fornasini, R. Gotter, and F. Rocca, Phys. Rev. B **52**, 149 (1995).

[25] G. Dalba, P. Fornasini, R. Grisenti, and J. Purans, Phys. Rev. Lett. **82**, 4240 (1999).

[26] G. Dalba, P. Fornasini, R. Grisenti, D. Pasqualini, D. Diop, and F. Monti, Phys. Rev. B **58**, 4793 (1998).

[27] G. Dalba, P. Fornasini, M. Grazioli, and F. Rocca, Phys. Rev. B **52**, 11034 (1995).

[28] G. Dalba, D. Diop, P. Fornasini, and F. Rocca, J. Phys.: Condens. Matter **6**, 3599 (1994).

[29] G. Dalba, P. Fornasini, F. Rocca, and S. Mobilio, Phys. Rev. B **41**, 9668 (1990).

[30] A. Silverman, A. Zunger, R. Kalish, and J. Adler, Phys. Rev. B **51**, 10795 (1995).

[31] J. B. Boyce and J. C. Mikkelsen, in *Ternary and Multinary Compounds*, page 359, Materials Research Society, Pittsburgh, 1987.

[32] J. C. Mikkelsen and J. B. Boyce, Phys. Rev. B **28**, 7130 (1983).

[33] M. Newville, *Fundamentals of XAFS*, http://xafs.org/Tutorials.

[34] E. A. Stern, Phys. Rev. B **10**, 3027 (1974).

[35] D. E. Sayers, E. A. Stern, and F. W. Lytle, Phys. Rev. Lett. **27**, 1204 (1971).

[36] A. L. Ankudinov, B. Ravel, J. J. Rehr, and S. D. Conradson, Phys. Rev. B **58**, 7565 (1998).

[37] G. Bunker, Nucl. Instr. and Meth. **207**, 437 (1983).

[38] Australian Synchrotron, http://www.synchrotron.org.au/content.asp?Document_ID=97.

[39] Australian Synchrotron, *Fact sheet XAS*, September 2008, http://www.synchrotron.org.au/content.asp?Document_ID=177.

[40] M. Newville, J. Synchrotron Rad. **8**, 322 (2001).

[41] B. Ravel and M. Newville, J. Synchrotron Rad. **12**, 537 (2005).

[42] FEFF8 manual, http://leonardo.phys.washington.edu/feff/Docs/Docs.html.

[43] J. F. Ziegler, J. P. Biersack, and U. Littmark, *The Stopping and Range of Ions in Solids*, Pergamon Press, New York, 2003.

[44] F. F. Morehead and B. L. Crowder, Rad. Effects **6**, 27 (1970).

[45] J. F. Gibbons, IEEE Proceedings **60**, 1062 (1972).

[46] D. A. Thompson, Rad. Eff. Def. Sol. **56**, 105 (1981).

[47] S. U. Campisano, S. Coffa, V. Raineri, F. Priolo, and E. Rimini, Nucl. Instr. Meth. B **80-81**, 514 (1993).

[48] N. Hecking, K. F. Heidemann, and E. Te Kaat, Nucl. Instr. Meth. B **15**, 760 (1986).

[49] R. L. Fleischer, P. B. Price, and R. M. Walker, J. Appl. Phys. **36**, 3645 (1965).

[50] P. Stampfli, Nucl. Instr. Meth. B **107**, 138 (1996).

[51] M. Toulemonde, C. Dufour, and E. Paumier, Phys. Rev. B **46**, 14362 (1992).

[52] A. Kamarou, W. Wesch, E. Wendler, A. Undisz, and M. Rettenmayr, Phys. Rev. B **73**, 184107 (2006).

[53] A. Kamarou, W. Wesch, E. Wendler, A. Undisz, and M. Rettenmayr, Phys. Rev. B **78**, 054111 (2008).

[54] O. Herre, W. Wesch, E. Wendler, P. I. Gaiduk, F. F. Komarov, S. Klaumünzer, and P. Meier, Phys. Rev. B **58**, 4832 (1998).

[55] P. I. Gaiduk, F. F. Komarov, and W. Wesch, Nucl. Instr. Meth. B **164-165**, 377 (2000).

[56] F. Komarov, L. Vlasukova, V. Yuvchenko, T. Petlitzkaya, and P. Zukowski, Vacuum **78**, 353 (2005).

[57] A. Kamarou, W. Wesch, E. Wendler, and S. Klaumünzer, Nucl. Instr. Meth. B **225**, 129 (2004).

[58] A. Kamarou, E. Wendler, and W. Wesch, J. Appl. Phys. **97**, 123532 (2005).

[59] N. Darowski, I. Zizak, G. Schumacher, S. Klaumünzer, and E. Wendler, Nucl. Instr. Meth. B **209**, 131 (2003).

[60] N. Darowski, I. Zizak, and G. Schumacher, Physica B **357**, 118 (2005).

[61] F. Komarov, P. Gaiduk, and A. Kamarou, Vacuum **63**, 657 (2001).

[62] A. Khalil, L. Chadderton, A. Stewart, M. Ridgway, D. Llewellyn, and A. Byrne, Rad. Measurements **40**, 770 (2005).

[63] G. Szenes, Z. E. Horváth, B. Pécz, F. Pászti, and L. Tóth, Phys. Rev. B **65**, 045206 (2002).

[64] W. Wesch, A. Kamarou, and E. Wendler, Nucl. Instr. Meth. B **225**, 111 (2004).

[65] M. Levalois and P. Marie, Nucl. Instr. Meth. B **156**, 64 (1999).

[66] W. K. Chu, J. W. Mayer, and M. A. Nicolet, *Backscattering Spectrometry*, Academic Press, New York, 1978.

[67] G. Götz and K. Gärtner, *High energy ion beam analysis of solids*, Akademie-Verlag, Berlin, 1988.

[68] J. R. Tesmer and M. Nastasi, *Handbook of modern ion beam analysis*, Materials Research Society, Pittsburgh, 1995.

[69] D. B. Williams and C. B. Carter, *Transmission Electron Microscopy*, Plenum Press, New York, 1996.

[70] J. P. McCaffrey, Microsc. Res. Tech. **24**, 180 (1993).

[71] R. Giulian, *PhD thesis*, The Australian National University, 2009.

[72] A. Joshi, M. O. Manasreh, E. A. Davis, and B. D. Weaver, Appl. Phys. Lett. **89**, 111907 (2006).

[73] K. Gärtner, Nucl. Instr. Meth. B **227**, 522 (2005).

[74] C. Licoppe, Y. I. Nissim, C. Meriadec, and P. Hénoc, Appl. Phys. Lett. **50**, 1648 (1987).

[75] I. Jenčič, E. P. Hollar, and I. M. Robertson, Phil. Mag. **83**, 2557 (2003).

[76] H. H. Tan, C. Jagadish, J. S. Williams, J. Zou, D. J. H. Cockayne, and A. Sikorski, J. Appl. Phys. **77**, 87 (1995).

[77] Z. S. Hussain, E. Wendler, W. Wesch, G. J. Foran, C. S. Schnohr, D. J. Llewellyn, and M. C. Ridgway, Phys. Rev. B **79**, 085202 (2009).

[78] S. Adachi, *Physical Properties of III-V Semiconductor Compounds*, Wiley, New York, 1992.

[79] S. Adachi, *Properties of Group-IV, III-V and II-VI Semiconductors*, Wiley, New York, 2005.

[80] W. H. Zachariasen, J. Am. Chem. Soc. **54**, 3841 (1932).

[81] D. E. Polk, J. Non-Cryst. Solids **5**, 365 (1971).

[82] G. A. N. Connell and R. J. Temkin, Phys. Rev. B **9**, 5323 (1974).

[83] M. L. Theye, A. Gheorghiu, and H. Launois, J. Phys. C **13**, 6569 (1980).

[84] A. M. Flank, P. Lagarde, D. Udron, S. Fisson, A. Gheorghiu, and M. L. Theye, J. Non-Cryst. Solids **97-98**, 435 (1987).

[85] P. I. Gaiduk, F. F. Komarov, V. S. Tishkov, W. Wesch, and E. Wendler, Phys. Rev. B **61**, 15785 (2000).

[86] L. J. Lewis, A. De Vita, and R. Car, Phys. Rev. B **57**, 1594 (1998).

[87] C. Glover, *PhD thesis*, The Australian National University, 2002.

[88] M. Ridgway, C. Glover, G. de M. Azevedo, S. Kluth, K. Yu, and G. Foran, Nucl. Instr. Meth. B **238**, 294 (2005).

[89] J. A. Van Vechten and J. C. Phillips, Phys. Rev. B **2**, 2160 (1970).

[90] J. Ibáñez, R. Cuscó, N. Blanco, G. González-Díaz, and L. Artús, Nucl. Instr. Meth. B **148**, 454 (1999).

[91] E. Bezakova, A. P. Byrne, C. J. Glover, M. C. Ridgway, and R. Vianden, Appl. Phys. Lett. **75**, 1923 (1999).

[92] K. Nordlund, M. Ghaly, R. S. Averback, M. Caturla, T. Diaz de la Rubia, and J. Tarus, Phys. Rev. B **57**, 7556 (1998).

[93] K. Nordlund, J. Peltola, J. Nord, J. Keinonen, and R. S. Averback, J. Appl. Phys. **90**, 1710 (2001).

[94] G. Dalba and P. Fornasini, J. Synchrotron Rad. **4**, 243 (1997).

[95] P. Fornasini, F. Monti, and A. Sanson, J. Synchrotron Rad. **8**, 1214 (2001).

[96] G. Beni and P. M. Platzman, Phys. Rev. B **14**, 1514 (1976).

[97] W. Böhmer and P. Rabe, J. Phys. C **12**, 2465 (1979).

[98] A. Sanson, F. Rocca, G. Dalba, P. Fornasini, R. Grisenti, M. Dapiaggi, and G. Artioli, Phys. Rev. B **73**, 214305 (2006).

[99] N. W. Ashcroft and N. Mermin, *Solid State Physics*, Saunders College, Philadelphia, 1976.

[100] P. S. Branicio and J. P. Rino, Phys. Stat. Sol. B **244**, 331 (2007).

[101] E. Sevillano, H. Meuth, and J. J. Rehr, Phys. Rev. B **20**, 4908 (1979).

[102] M. Vaccari and P. Fornasini, J. Synchrotron Rad. **13**, 321 (2006).

[103] A. I. Frenkel and J. J. Rehr, Phys. Rev. B **48**, 585 (1993).

[104] T. Yokoyama, J. Synchrotron Rad. **6**, 323 (1999).

[105] A. Filipponi and A. Di Cicco, Phys. Rev. B **51**, 12322 (1995).

[106] P. Deus, H. A. Schneider, U. Voland, and K. Stiehler, Phys. Stat. Sol. A **103**, 443 (1987).

[107] L. L. Araujo, P. Kluth, G. de M. Azevedo, and M. C. Ridgway, Phys. Rev. B **74**, 184102 (2006).

[108] R. Saravanan, S. K. Mohanlal, and K. S. Chandrasekaran, Z. Kristallogr. **200**, 7 (1992).

[109] J. S. Reid, Acta Crys. A **39**, 1 (1983).

[110] M. Schowalter, A. Rosenauer, J. T. Titantah, and D. Lamoen, Acta Crys. A **65**, 5 (2009).

[111] V. M. Glazov, A. S. Pashinkin, and L. M. Pavlova, High Temperature **40**, 369 (2002).

[112] P. N. Keating, Phys. Rev. **145**, 637 (1966).

[113] R. M. Martin, Phys. Rev. B **1**, 4005 (1970).

[114] A.-B. Chen and A. Sher, Phys. Rev. B **32**, 3695 (1985).

[115] M. C. Ridgway, G. de M. Azevedo, C. J. Glover, K. M. Yu, and G. J. Foran, Nucl. Instr. Meth. B **199**, 235 (2003).

[116] L. Vegard, Z. Phys. **5**, 17 (1921).

[117] L. Nordheim, Ann. Phys. **401**, 607 and 641 (1931).

[118] L. Pauling and M. L. Huggins, Z. Kristallogr. **87**, 205 (1934).

[119] C. K. Shih, W. E. Spicer, W. A. Harrison, and A. Sher, Phys. Rev. B **31**, 1139 (1985).

[120] J. L. Martins and A. Zunger, Phys. Rev. B **30**, 6217 (1984).

[121] A. Balzarotti, M. Czyżyk, A. Kisiel, N. Motta, M. Podgórny, and M. Zimnal-Starnawska, Phys. Rev. B **30**, 2295 (1984).

[122] A. Balzarotti, N. Motta, A. Kisiel, M. Zimnal-Starnawska, M. T. Czyżyk, and M. Podgórny, Phys. Rev. B **31**, 7526 (1985).

[123] G. P. Srivastava, J. L. Martins, and A. Zunger, Phys. Rev. B **31**, 2561 (1985).

[124] J. C. Mikkelsen and J. B. Boyce, Phys. Rev. Lett. **49**, 1412 (1982).

[125] Y. Cai and M. F. Thorpe, Phys. Rev. B **46**, 15879 (1992).

[126] J. G. Kirkwood, J. Chem. Phys. **7**, 506 (1939).

[127] Y. Cai and M. F. Thorpe, Phys. Rev. B **46**, 15872 (1992).

[128] Z. H. Wu, K. Q. Lu, Y. R. Wang, J. Dong, H. F. Li, C. X. Li, and Z. Z. Fang, Phys. Rev. B **48**, 8694 (1993).

[129] A. Balzarotti, in *Ternary and Multinary Compounds*, page 333, Materials Research Society, Pittsburgh, 1987.

[130] J. B. Boyce and J. C. Mikkelsen, Phys. Rev. B **31**, 6903 (1985).

[131] A. Di Cicco, E. Principi, and A. Filipponi, Phys. Rev. B **65**, 212106 (2002).

[132] J. C. Woicik, Phys. Rev. B **57**, 6266 (1998).

[133] J. C. Woicik, J. A. Gupta, S. P. Watkins, and E. D. Crozier, Appl. Phys. Lett. **73**, 1269 (1998).

[134] I.-K. Jeong, F. Mohiuddin-Jacobs, V. Petkov, S. J. L. Billinge, and S. Kycia, Phys. Rev. B **63**, 205202 (2001).

[135] S. Pascarelli, F. Boscherini, C. Lamberti, and S. Mobilio, Phys. Rev. B **56**, 1936 (1997).

[136] M. Tormen, D. De Salvador, A. V. Drigo, F. Romanato, F. Boscherini, and S. Mobilio, Phys. Rev. B **63**, 115326 (2001).

[137] M. Thompson, http://www.genplot.com/index.htm.

[138] J. C. Woicik, C. E. Bouldin, K. E. Miyano, and C. A. King, Phys. Rev. B **55**, 15386 (1997).

Abbreviations

DOS	Density of states
EXAFS	Extended x-ray absorption fine structure
FT	Fourier transformation, Fourier transform
LEI	Low energy ion
MD	Molecular dynamics
MS	Multiple scattering
MSD	Mean square displacement
MSRD	Mean square relative displacement
NN	Nearest neighbor
P & H	Pauling and Huggins
RBS	Rutherford backscattering spectroscopy
RBS/c	Rutherford backscattering spectroscopy in channeling configuration
SHI	Swift heavy ion
SS	Single scattering
TEM	Transmission electron microscopy
VCA	Virtual crystal approximation
VFF	Valence force field
XAFS	X-ray absorption fine structure
XANES	X-ray absorption near edge structure
XRD	X-ray diffraction

Appendix A

Temperature dependence calculations

The temperature dependence of the EXAFS second and third cumulants has been calculated by Frenkel and Rehr [103] and Yokoyama [104] using a one-dimensional oscillator model and quantum mechanical perturbation theory. In the following, a rigorous derivation of Eqs (5.17) and (5.19) based on Yokoyama [104] but including all the intermediate steps is given.

A.1 Pair-potential

The absorber-backscatterer pair is treated as a one-dimensional anharmonic oscillator that is characterized by the pair potential (5.18)

$$V(r) = \frac{1}{2}k_0 r^2 - k_3 r^3 + ... \tag{A.1}$$

where k_0 and k_3 are the harmonic and cubic force constants, respectively, and $R - R_0$ has been replaced by r. The Einstein frequency is related to k_0 by $\omega_{\mathrm{E},\|} \equiv \omega = \sqrt{k_0/\mu}$ where μ denotes the reduced mass of the atomic pair. As discussed by Fornasini *et al.* [23], the first cumulant $\tilde{C}_1$ calculated using Eq. (A.1) does not correspond to the EXAFS first cumulant R_{EXAFS} because the one-dimensional model cannot take into account effects due to perpendicular vibrations. In contrast, the second and third cumulant, $\tilde{C}_2$ and $\tilde{C}_3$, respectively, correspond to the EXAFS second and third cumulant [23]

$$
\begin{aligned}
R_{\mathrm{EXAFS}} &\neq \tilde{C}_1 = \langle r \rangle \\
\sigma^2_{\mathrm{EXAFS}} &= \tilde{C}_2 = \left\langle (r - \tilde{C}_1)^2 \right\rangle = \langle r^2 \rangle - \tilde{C}_1^2 \\
C_3 &= \tilde{C}_3 = \left\langle (r - \tilde{C}_1)^3 \right\rangle = \langle r^3 \rangle - 3 \langle r^2 \rangle \tilde{C}_1 + 2\tilde{C}_1^3 .
\end{aligned}
\tag{A.2}
$$

The total energy H of the system is the sum of kinetic and potential energy

$$
H = \frac{p^2}{2\mu} + V(r) = \frac{p^2}{2\mu} + \frac{k_0}{2} r^2 - k_3 r^3 \tag{A.3}
$$

where p denotes the momentum. The first two terms correspond to kinetic and potential energy of a harmonic oscillator. Writing this energy in terms of quantum mechanical operators yields

$$
\hat{H}_0 = \frac{\hat{p}^2}{2\mu} + \frac{k_0}{2} \hat{r}^2 . \tag{A.4}
$$

The solutions of the eigenvalue equation $\hat{H}_0 |n\rangle = E_n |n\rangle$ are the harmonic oscillator states $|n\rangle$ with eigenvalues $E_n = n\hbar\omega$. Here, the zero-point energy $E_0 = \hbar\omega/2$ has been set to zero for convenience [103]. The eigenstates $|n\rangle$ are normalized and orthogonal, thus

$$
\langle n' | n \rangle = \begin{cases} 1 & \text{if} \quad n' = n \\ 0 & \text{if} \quad n' \neq n. \end{cases} \tag{A.5}
$$

A.2 Thermal average and perturbation theory

The quantum mechanical thermal average of a physical quantity A is given by the ratio of two traces

$$
\langle \hat{A} \rangle = \frac{\mathrm{Tr}\, \hat{A} \mathrm{e}^{-\beta \hat{H}}}{\mathrm{Tr}\, \mathrm{e}^{-\beta \hat{H}}} = \sum_{n=0}^{\infty} \langle n | \hat{A} \mathrm{e}^{-\beta \hat{H}} | n \rangle \Big/ \sum_{n=0}^{\infty} \langle n | \mathrm{e}^{-\beta \hat{H}} | n \rangle . \tag{A.6}
$$

where $\mathrm{Tr}\, \mathrm{e}^{-\beta \hat{H}} = Z$ is the partition function and $\beta = 1/k_{\mathrm{B}}T$ depends on Boltzmann's constant k_{B} and the temperature T. Using Eqs (A.3) and (A.4), $\hat{H}$ can be written as

$$
\hat{H} = \hat{H}_0 + \hat{H}' \qquad \text{with} \qquad \hat{H}' = -k_3 \hat{r}^3 . \tag{A.7}
$$

If the anharmonic term $\hat{H}'$ is small compared to the harmonic term $\hat{H}_0$, the

quantity $e^{-\beta\hat{H}}$ can be approximated by quantum mechanical perturbation theory up to first order

$$\begin{aligned} e^{-\beta\hat{H}} &= e^{-\beta\hat{H}_0}\left[1 - \int_0^\beta e^{\beta'\hat{H}_0}\hat{H}'e^{-\beta'\hat{H}_0}d\beta' + ...\right] \\ &= e^{-\beta\hat{H}_0} - e^{-\beta\hat{H}_0}\int_0^\beta e^{\beta'\hat{H}_0}\hat{H}'e^{-\beta'\hat{H}_0}d\beta'. \end{aligned} \tag{A.8}$$

Using Eqs (A.7) and (A.8), the thermal average (A.6) thus becomes

$$\begin{aligned} \langle\hat{A}\rangle &= \frac{1}{Z}\operatorname{Tr}\hat{A}e^{-\beta\hat{H}_0} - \frac{1}{Z}\operatorname{Tr}\hat{A}e^{-\beta\hat{H}_0}\int_0^\beta e^{\beta'\hat{H}_0}\hat{H}'e^{-\beta'\hat{H}_0}d\beta' \\ &= \frac{1}{Z}\sum_{n=0}^{\infty}\langle n|\hat{A}e^{-\beta\hat{H}_0}|n\rangle \\ &\qquad + k_3\frac{1}{Z}\sum_{n=0}^{\infty}\langle n|\hat{A}e^{-\beta\hat{H}_0}\int_0^\beta e^{\beta'\hat{H}_0}\hat{r}^3e^{-\beta'\hat{H}_0}d\beta'|n\rangle. \end{aligned} \tag{A.9}$$

The zero order term can be further evaluated by

$$e^{-\beta\hat{H}_0}|n\rangle = |n\rangle\, e^{-\beta E_n} = |n\rangle\, e^{-\beta\hbar\omega n} = |n\rangle\, z^n \tag{A.10}$$

with $z = e^{-\beta\hbar\omega}$. Similarly,

$$e^{-\beta'\hat{H}_0}|n\rangle = |n\rangle\, e^{-\beta' E_n} \tag{A.11}$$

for the first order term. Now $\hat{r}^3|n\rangle$ has to be evaluated. To this end, $\hat{r}$ is expressed in terms of creation and annihilation operators, $\hat{a}^\dagger$ and $\hat{a}$,

$$\hat{r} = \sigma_0(\hat{a} + \hat{a}^\dagger) \tag{A.12}$$

with $\sigma_0 = \sqrt{\hbar/2\mu\omega}$ and

$$\begin{aligned} \hat{a}|n\rangle &= \sqrt{n}\,|n-1\rangle \\ \hat{a}^\dagger|n\rangle &= \sqrt{n+1}\,|n+1\rangle. \end{aligned} \tag{A.13}$$

Thus

$$\hat{r}|n\rangle = \sigma_0\sqrt{n}\,|n-1\rangle + \sigma_0\sqrt{n+1}\,|n+1\rangle \tag{A.14}$$

$$\begin{aligned} \hat{r}^2|n\rangle = {} & \sigma_0^2\sqrt{n(n-1)}\,|n-2\rangle + \sigma_0^2(2n+1)\,|n\rangle \\ & + \sigma_0^2\sqrt{(n+1)(n+2)}\,|n+2\rangle \end{aligned} \tag{A.15}$$

$$\begin{aligned}\hat{r}^3|n\rangle = \sigma_0^3\sqrt{n(n-1)(n-2)}\,|n-3\rangle + 3\sigma_0^3 n\sqrt{n}\,|n-1\rangle \\ + 3\sigma_0^3(n+1)\sqrt{n+1}\,|n+1\rangle \\ + \sigma_0^3\sqrt{(n+1)(n+2)(n+3)}\,|n+3\rangle.\end{aligned} \tag{A.16}$$

Using Eq. (A.16), the first order term in Eq. (A.9) can then be evaluated as

$$\begin{aligned}&\mathrm{e}^{-\beta\hat{H}_0}\int_0^\beta \mathrm{e}^{\beta'\hat{H}_0}\hat{r}^3\mathrm{e}^{-\beta'\hat{H}_0}\mathrm{d}\beta'|n\rangle \\ &= \sigma_0^3\sqrt{n(n-1)(n-2)}\,|n-3\rangle\, z^{n-3}\int_0^\beta \mathrm{e}^{\beta' E_{n-3}}\mathrm{e}^{-\beta' E_n}\mathrm{d}\beta' \\ &\quad + 3\sigma_0^3 n\sqrt{n}\,|n-1\rangle\, z^{n-1}\int_0^\beta \mathrm{e}^{\beta' E_{n-1}}\mathrm{e}^{-\beta' E_n}\mathrm{d}\beta' \\ &\quad + 3\sigma_0^3(n+1)\sqrt{n+1}\,|n+1\rangle\, z^{n+1}\int_0^\beta \mathrm{e}^{\beta' E_{n+1}}\mathrm{e}^{-\beta' E_n}\mathrm{d}\beta' \\ &\quad + \sigma_0^3\sqrt{(n+1)(n+2)(n+3)}\,|n+3\rangle\, z^{n+3}\int_0^\beta \mathrm{e}^{\beta' E_{n+3}}\mathrm{e}^{-\beta' E_n}\mathrm{d}\beta' \\ &= \frac{\sigma_0^3}{3\hbar\omega}\sqrt{n(n-1)(n-2)}\,|n-3\rangle\,(z^{n-3}-z^n) \\ &\quad + \frac{3\sigma_0^3}{\hbar\omega}n\sqrt{n}\,|n-1\rangle\,(z^{n-1}-z^n) \\ &\quad + \frac{3\sigma_0^3}{\hbar\omega}(n+1)\sqrt{n+1}\,|n+1\rangle\,(z^n-z^{n+1}) \\ &\quad + \frac{\sigma_0^3}{3\hbar\omega}\sqrt{(n+1)(n+2)(n+3)}\,|n+3\rangle\,(z^n-z^{n+3}).\end{aligned} \tag{A.17}$$

Furthermore, the following relations are needed to calculate the sums in Eq. (A.9)

$$\begin{aligned}\sum_{n=0}^{\infty} z^n &= \frac{1}{1-z} \\ \sum_{n=0}^{\infty} n z^n &= \frac{z}{(1-z)^2} \\ \sum_{n=0}^{\infty} n^2 z^n &= \frac{z(1+z)}{(1-z)^3} \\ \sum_{n=0}^{\infty} n^3 z^n &= \frac{z(1+4z+z^2)}{(1-z)^4}.\end{aligned} \tag{A.18}$$

A.3 Calculation of cumulants

Using Eqs (A.8), (A.10), and (A.17) the partition function Z can be determined. The first order term vanishes due to the orthogonality of the eigenstates (Eq. (A.5)) and only the zero order term remains

$$Z = \sum_{n=0}^{\infty} \langle n|\mathrm{e}^{-\beta\hat{H}}|n\rangle = \sum_{n=0}^{\infty} z^n = \frac{1}{1-z}. \tag{A.19}$$

Although the first cumulant $\tilde{C}_1$ does not represent the EXAFS first cumulant, it is needed to calculate the higher cumulants. Setting $\hat{A} = \hat{r}$, the term $\langle n|\hat{r}$ now has to be evaluated. Since r is a measurable physical quantity, its operator $\hat{r}$ is hermitian, $\hat{r} = \hat{r}^\dagger$, and can thus act on $\langle n|$

$$\langle n|\hat{r} = \langle n|\hat{r}^\dagger = \sigma_0\sqrt{n}\,\langle n-1| + \sigma_0\sqrt{n+1}\,\langle n+1|, \tag{A.20}$$

similar to Eq. (A.14). With Eq. (A.10) and the orthogonality of the eigenstates it follows that the zero order term in Eq. (A.9) equals zero. $\tilde{C}_1$ is thus given by the first order term

$$\begin{aligned}
\tilde{C}_1 &= \frac{k_3}{Z}\frac{\sigma_0^4}{\hbar\omega}\sum_{n=0}^{\infty}\left[3n^2(z^{n-1}-z^n) + 3(n+1)^2(z^n - z^{n+1})\right] \\
&= \frac{k_3}{Z}\frac{\sigma_0^4}{\hbar\omega}3(\frac{1}{z}-1)\left[\sum_{n=0}^{\infty} n^2 z^n + \sum_{n=0}^{\infty}(n+1)^2 z^{n+1}\right] \\
&= 6\frac{k_3\sigma_0^4}{\hbar\omega}(1-z)\frac{(1-z)}{z}\frac{z(1+z)}{(1-z)^3} \\
&= 6\frac{k_3\sigma_0^4}{\hbar\omega}\frac{(1+z)}{(1-z)}
\end{aligned} \tag{A.21}$$

where Eqs (A.17) and (A.18) have been used.

According to Eq. (A.2), the second cumulant is given by $\tilde{C}_2 = \langle r^2\rangle - \tilde{C}_1^2$. Based on Eq. (A.15), the expression $\langle n|\hat{r}^2 = \langle n|\hat{r}^{\dagger 2}$ yields terms with $\langle n-2|$, $\langle n|$ and $\langle n+2|$. Hence the first order term in Eq. (A.9) vanishes since Eq. (A.17) contains only terms with $|n-3\rangle$, $|n-1\rangle$, $|n+1\rangle$ and $|n+3\rangle$. In the zero order

contribution only the term with $|n\rangle$ survives yielding

$$\begin{aligned}\langle r^2\rangle &= \frac{\sigma_0^2}{Z}\sum_{n=0}^{\infty}(2n+1)z^n \\ &= \sigma_0^2(1-z)\left[\frac{2z}{(1-z)^2}+\frac{1}{(1-z)}\right] \\ &= \sigma_0^2\frac{(1+z)}{(1-z)}\end{aligned} \tag{A.22}$$

where Eq. (A.18) has been used. $\tilde{C}_1^2$ is proportional to k_3^2 (see Eq. (A.21)) and thus corresponds to a second order perturbation term. Considering only terms up to first order, the second cumulant becomes

$$\tilde{C}_2 = \langle r^2\rangle = \sigma_0^2\frac{(1+z)}{(1-z)}. \tag{A.23}$$

The third cumulant is given by $\tilde{C}_3 = \langle r^3\rangle - 3\langle r^2\rangle\tilde{C}_1 + 2\tilde{C}_1^3$ (Eq. (A.2)). Based on Eq. (A.16), the expression $\langle n|\hat{r}^3 = \langle n|\hat{r}^{\dagger 3}$ yields terms with $\langle n-3|$, $\langle n-1|$, $\langle n+1|$ and $\langle n+3|$. Thus, the zero order term in Eq. (A.9) equals zero and $\langle r^3\rangle$ amounts to

$$\begin{aligned}\langle r^3\rangle &= \frac{k_3}{Z}\frac{\sigma_0^6}{\hbar\omega}\sum_{n=0}^{\infty}\Big[\frac{1}{3}n(n-1)(n-2)(z^{n-3}-z^n) + 9n^3(z^{n-1}-z^n) \\ &\qquad + 9(n+1)^3(z^n - z^{n+1}) \\ &\qquad + \frac{1}{3}(n+1)(n+2)(n+3)(z^n - z^{n+3})\Big] \\ &= \frac{k_3}{Z}\frac{\sigma_0^6}{\hbar\omega}\Big[18(\frac{1}{z}-1)\sum_{n=0}^{\infty}n^3z^n \\ &\qquad + \frac{2}{3}(\frac{1}{z}-z^2)\sum_{n=0}^{\infty}(n^3+3n^2+2n)z^n\Big] \\ &= \frac{k_3}{Z}\frac{\sigma_0^6}{\hbar\omega}\left[18\frac{(1-z)}{z}\frac{z(1+4z+z^2)}{(1-z)^4}+\frac{2}{3}\frac{(1-z^3)}{z}\frac{6z}{(1-z)^4}\right] \\ &= \frac{k_3\sigma_0^6}{\hbar\omega}(1-z)\left[\frac{18(1+4z+z^2)}{(1-z)^3}+\frac{4(1+z+z^2)}{(1-z)^3}\right] \\ &= \frac{k_3\sigma_0^6}{\hbar\omega}\frac{(22+76z+22z^2)}{(1-z)^2}.\end{aligned} \tag{A.24}$$

$\tilde{C}_1^3$ is proportional to k_3^3 and thus corresponds to a third order perturbation term. Considering only terms up to first order, the third cumulant becomes

$$\begin{aligned}\tilde{C}_3 &= \langle r^3 \rangle - 3 \langle r^2 \rangle \tilde{C}_1 \\ &= \frac{k_3 \sigma_0^6}{\hbar\omega} \left[\frac{(22 + 76z + 22z^2) - 18(1 + 2z + z^2)}{(1-z)^2} \right] \\ &= \frac{k_3 \sigma_0^6}{\hbar\omega} \frac{4(1 + 10z + z^2)}{(1-z)^2}.\end{aligned} \tag{A.25}$$

If the pair potential (A.1) contains a non-zero fourth order force constant (a term such as $k_4 r^4$) then the first order perturbation terms for Z and $\langle r^2 \rangle$ no longer vanish leading to a first order anharmonic correction. Results including a fourth order force constant and perturbation terms up to the second order are given by Yokoyama for the partition function Z and the first four cumulants $\tilde{C}_1$, $\tilde{C}_2$, $\tilde{C}_3$ and $\tilde{C}_4$ [104].

As discussed above, the EXAFS second and third cumulant correspond to $\tilde{C}_2$ and $\tilde{C}_3$, respectively. Applying the relations $\sigma_0^2 = \hbar/2\mu\omega = \hbar^2/2\mu k_\mathrm{B}\Theta_{\mathrm{E},\parallel}$ and $\beta\hbar\omega = \hbar\omega/k_\mathrm{B}T = \Theta_{\mathrm{E},\parallel}/T$ to Eqs (A.23) and (A.25) thus yields

$$\begin{aligned}\sigma^2_{\mathrm{EXAFS}} = \sigma_0^2 \frac{(1+z)}{(1-z)} &= \frac{\hbar^2}{2\mu k_\mathrm{B}} \frac{1}{\Theta_{\mathrm{E},\parallel}} \frac{1 + \mathrm{e}^{-\Theta_{\mathrm{E},\parallel}/T}}{1 - \mathrm{e}^{-\Theta_{\mathrm{E},\parallel}/T}} \\ &= \frac{\hbar^2}{2\mu k_\mathrm{B}} \frac{1}{\Theta_{\mathrm{E},\parallel}} \coth\left(\frac{\Theta_{\mathrm{E},\parallel}}{2T}\right)\end{aligned} \tag{A.26}$$

and

$$\begin{aligned}C_3 = \frac{k_3 \sigma_0^6}{\hbar\omega} \frac{4(1 + 10z + z^2)}{(1-z)^2} &= \frac{\hbar^6}{\mu^3 k_\mathrm{B}^4} \frac{k_3}{\Theta^4_{\mathrm{E},\parallel}} \frac{3(1+z)^2 - 2(1-z)^2}{2(1-z)^2} \\ &= \frac{\hbar^6}{\mu^3 k_\mathrm{B}^4} \frac{k_3}{\Theta^4_{\mathrm{E},\parallel}} \left[\frac{3}{2} \left(\frac{1+z}{1-z} \right)^2 - 1 \right] \\ &= \frac{\hbar^6}{\mu^3 k_\mathrm{B}^4} \frac{k_3}{\Theta^4_{\mathrm{E},\parallel}} \left[\frac{3}{2} \left(\coth\left(\frac{\Theta_{\mathrm{E},\parallel}}{2T} \right) \right)^2 - 1 \right].\end{aligned} \tag{A.27}$$

Except for the static contributions, these two relations represent Eqs (5.17) and (5.19) given in Section 5.1.3 and describe the temperature dependence of the EXAFS Debye-Waller factor and third cumulant characterized by $\Theta_{\mathrm{E},\parallel}$.

Appendix B

Ternary structure calculations

Section 6.1 introduces a number of models that calculate the first NN distances in $A_{1-x}B_xC$ ternary alloys. In the following, the model by Shih *et al.* [119] is presented to illustrate the basic approach underlying most of the models. The methodology of Balzarotti *et al.* [122] is also discussed in detail since it allows the calculation of the first NN distances over the whole compositional range. The derivation performed in Section B.2 provides all the expressions needed to apply this model to any given ternary alloy. Calculations were then carried out for the $Ga_{1-x}In_xP$ system studied in this work.

B.1 Model by Shih *et al.*

The model by Shih *et al.* [119] is the simplest of all. It considers the case of an impurity atom B embedded in an AC crystal as shown schematically in Fig. B.1 (a). Due to the symmetry of the dilute limit all first NN C atoms will be displaced radially, either towards or away from the impurity depending on the nature of A and B. In contrast, the second NN A atoms are assumed to be fixed at the binary lattice sites. The resulting geometry is depicted schematically in Fig. B.1 (b) for one of the first NN C atoms. The distortion energy U of such a configuration is taken as a simple spring potential (Hooke's Law)

$$U = 3\frac{\alpha_{AC}}{2}\left(d_{AC} - d_{AC}^{bin}\right)^2 + \frac{\alpha_{BC}}{2}\left(d_{BC} - d_{BC}^{bin}\right)^2 \tag{B.1}$$

where α_{AC} and α_{BC} are the force constants for A-C and B-C bonds, respectively. d_{AC} and d_{BC} are the distorted first NN distances whereas the equilibrium dis-

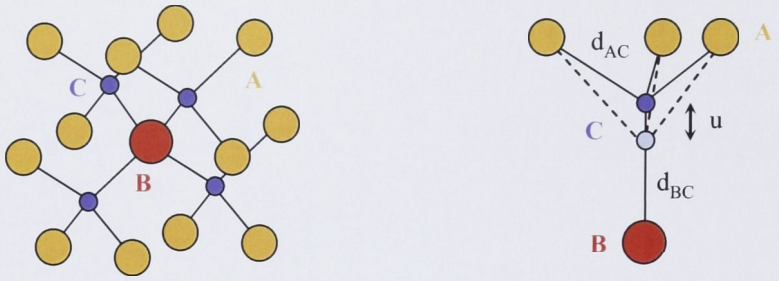

(a) Impurity atom B embedded in an AC crystal

(b) Resulting displacement of a first NN C atom

Figure B.1: Schematic for the dilute limit geometry considered by Shih *et al.* [119].

tances are taken as the corresponding binary bond lengths $d_{\mathrm{AC}}^{\mathrm{bin}}$ and $d_{\mathrm{BC}}^{\mathrm{bin}}$ with $\Delta d^{\mathrm{bin}} = d_{\mathrm{BC}}^{\mathrm{bin}} - d_{\mathrm{AC}}^{\mathrm{bin}}$. If the radial displacement of the C atoms is u as indicated in Fig. B.1 (b), then the B-C distance is simply $d_{\mathrm{BC}} = d_{\mathrm{AC}}^{\mathrm{bin}} + u$. The exact expression for the A-C distance is more complicated but for small displacements u it can be approximated by $d_{\mathrm{AC}} \approx d_{\mathrm{AC}}^{\mathrm{bin}} - \frac{1}{3}u$. With further assuming that $\alpha_{\mathrm{BC}} = \alpha_{\mathrm{AC}} = \alpha$, the distortion energy becomes

$$\begin{aligned} U &= 3\frac{\alpha}{2}\left(-\frac{u}{3}\right)^2 + \frac{\alpha}{2}\left(d_{\mathrm{AC}}^{\mathrm{bin}} + u - d_{\mathrm{BC}}^{\mathrm{bin}}\right)^2 \\ &= \frac{\alpha}{6}u^2 + \frac{\alpha}{2}\left(\Delta d^{\mathrm{bin}} - u\right)^2 \\ &= \frac{2\alpha}{3}u^2 - \alpha\Delta d^{\mathrm{bin}}u + \frac{\alpha}{2}(\Delta d^{\mathrm{bin}})^2. \end{aligned} \tag{B.2}$$

The minimum-energy configuration is achieved for

$$0 = \frac{\mathrm{d}E}{\mathrm{d}u} = \frac{4\alpha}{3}u - \alpha\Delta d^{\mathrm{bin}} = \alpha\left(\frac{4}{3}u - \Delta d^{\mathrm{bin}}\right) \tag{B.3}$$

and hence

$$u = \frac{3}{4}\Delta d^{\mathrm{bin}}. \tag{B.4}$$

The impurity bond lengths $d_{\mathrm{BC}}^{\mathrm{AC:B}}$ thus equals

$$d_{\mathrm{BC}}^{\mathrm{AC:B}} = d_{\mathrm{AC}}^{\mathrm{bin}} + \frac{3}{4}\Delta d^{\mathrm{bin}} = d_{\mathrm{BC}}^{\mathrm{bin}} - \frac{1}{4}\Delta d^{\mathrm{bin}} \tag{B.5}$$

and the relaxation parameter ϵ becomes

$$\epsilon = \frac{d_{\mathrm{BC}}^{\mathrm{AC:B}} - d_{\mathrm{AC}}^{\mathrm{bin}}}{\Delta d^{\mathrm{bin}}} = \frac{3}{4} = 0.75\,. \tag{B.6}$$

This result is independent of the atomic species A, B and C and is determined solely by the geometry of the crystal structure.

B.2 Model by Balzarotti *et al.*

Balzarotti *et al.* calculate the average A-C and B-C distances over the whole compositional range of $Cd_{1-x}Mn_xTe$ and $Ga_{1-x}In_xAs$ alloys [122]. The lattice constant $a(x)$ is calculated using Vegard's Law: $a(x) = a_{AC} + x(a_{BC} - a_{AC}) = (1 - x)a_{AC} + xa_{BC}$. The atoms of the mixed sublattice are fixed to the crystallographic sites determined by the VCA. The C atoms are allowed to relax according to their first NN environment. In the ternary phase, there are five possible first NN arrangements, characterized by the number n of B-type atoms, as shown in Fig. B.2. The edge length of the cube equals $\frac{1}{2}a(x)$ and thus depends on the composition x. For each of the five different tetrahedra, relaxation yields a unique A-C and B-C distance, denoted by $d_{AC}^{(n)}(x)$ and $d_{BC}^{(n)}(x)$. The mean A-C

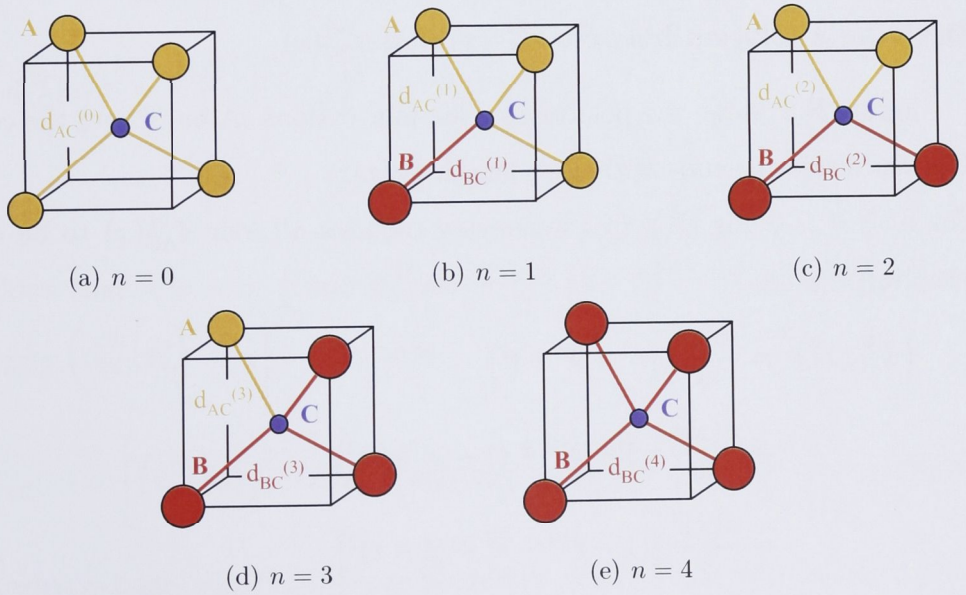

(a) $n = 0$ (b) $n = 1$ (c) $n = 2$

(d) $n = 3$ (e) $n = 4$

Figure B.2: Schematic of the five possible first NN environments around C atoms in $A_{1-x}B_xC$. The different types of tetrahedra are characterized by the number n of B-type atoms. The edge length of the cube equals half the lattice constant.

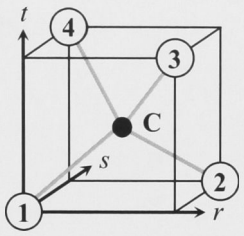

$$1 : \frac{a}{2}(0,0,0) \qquad 3 : \frac{a}{2}(1,0,1) \qquad C : \frac{a}{2}(r,s,t)$$

$$2 : \frac{a}{2}(1,1,0) \qquad 4 : \frac{a}{2}(0,1,1)$$

Figure B.3: Positions of the four cations (A or B) and the central C atom.

and B-C distances at any given x, $d_{\mathrm{AC}}(x)$ and $d_{\mathrm{BC}}(x)$, respectively, are thus the average over the five different $d_{\mathrm{AC}}^{(n)}(x)$ and $d_{\mathrm{BC}}^{(n)}(x)$ weighted with the probabilities of finding the different n-type tetrahedra at this composition x. The calculation can therefore be organized into the following three steps:

(i) deriving a relation between $d_{\mathrm{AC}}^{(n)}(x)$ and $d_{\mathrm{BC}}^{(n)}(x)$ to yield one free parameter that describes the distorted geometry for each n,

(ii) determining this parameter and thus $d_{\mathrm{AC}}^{(n)}(x)$ and $d_{\mathrm{BC}}^{(n)}(x)$ for each n and x by minimizing the distortion energy U and

(iii) performing a weighted average over all $d_{\mathrm{AC}}^{(n)}(x)$ and $d_{\mathrm{BC}}^{(n)}(x)$ to obtain $d_{\mathrm{AC}}(x)$ and $d_{\mathrm{BC}}(x)$ as a function of x.

Deriving a relation between $d_{\mathrm{AC}}^{(n)}(x)$ and $d_{\mathrm{BC}}^{(n)}(x)$

Figure B.3 shows the positions of the four cations (A or B) and the central C atom inside the cube with edge length $\frac{1}{2}a(x)$.

For $n = 0$ (see Fig. B.2 (a)) symmetry requires all four $d_{\mathrm{AC}}^{(0)}(x)$ to be equal, yielding

$$\begin{aligned}
\left(d_{\mathrm{AC}}^{(0)}(x)\right)^2 &= \frac{a(x)^2}{4}\left[r^2+s^2+t^2\right] \\
&= \frac{a(x)^2}{4}\left[(1-r)^2+(1-s)^2+t^2\right] \\
&= \frac{a(x)^2}{4}\left[(1-r)^2+s^2+(1-t)^2\right] \\
&= \frac{a(x)^2}{4}\left[r^2+(1-s)^2+(1-t)^2\right].
\end{aligned} \tag{B.7}$$

It follows that $r = s = t = \frac{1}{2}$ and $d_{\mathrm{AC}}^{(0)}(x) = \frac{\sqrt{3}}{4}a(x)$.

For $n = 1$ (see Fig. B.2 (b)) the $d^{(1)}_{\mathrm{AC}}(x)$ and $d^{(1)}_{\mathrm{BC}}(x)$ distances can be written as

$$\begin{aligned}
\left(d^{(1)}_{\mathrm{BC}}(x)\right)^2 &= \frac{a(x)^2}{4}\left[r^2 + s^2 + t^2\right] \\
\left(d^{(1)}_{\mathrm{AC}}(x)\right)^2 &= \frac{a(x)^2}{4}\left[(1-r)^2 + (1-s)^2 + t^2\right] \\
&= \frac{a(x)^2}{4}\left[(1-r)^2 + s^2 + (1-t)^2\right] \\
&= \frac{a(x)^2}{4}\left[r^2 + (1-s)^2 + (1-t)^2\right].
\end{aligned} \tag{B.8}$$

It follows that $r = s = t$ and $d^{(1)}_{\mathrm{BC}}(x) = \frac{\sqrt{3}}{2}a(x)r$. Solving for r gives $r = \frac{2}{\sqrt{3}a(x)}d^{(1)}_{\mathrm{BC}}(x)$ and thus

$$d^{(1)}_{\mathrm{AC}}(x) = \left[\left(d^{(1)}_{\mathrm{BC}}(x)\right)^2 - \frac{2a(x)}{\sqrt{3}}d^{(1)}_{\mathrm{BC}}(x) + \frac{a(x)^2}{2}\right]^{1/2}. \tag{B.9}$$

For $n = 2$ (see Fig. B.2 (c)), $d^{(2)}_{\mathrm{AC}}(x)$ and $d^{(2)}_{\mathrm{BC}}(x)$ become

$$\begin{aligned}
\left(d^{(2)}_{\mathrm{BC}}(x)\right)^2 &= \frac{a(x)^2}{4}\left[r^2 + s^2 + t^2\right] \\
&= \frac{a(x)^2}{4}\left[(1-r)^2 + (1-s)^2 + t^2\right] \\
\left(d^{(2)}_{\mathrm{AC}}(x)\right)^2 &= \frac{a(x)^2}{4}\left[(1-r)^2 + s^2 + (1-t)^2\right] \\
&= \frac{a(x)^2}{4}\left[r^2 + (1-s)^2 + (1-t)^2\right].
\end{aligned} \tag{B.10}$$

It follows that $r = s = \frac{1}{2}$ and $d^{(2)}_{\mathrm{BC}}(x) = \frac{a(x)}{2}\left[\frac{1}{2} + t^2\right]^{1/2}$. Solving for t gives $t = \left[\frac{4}{a(x)^2}\left(d^{(2)}_{\mathrm{BC}}(x)\right)^2 - \frac{1}{2}\right]^{1/2}$ and thus

$$d^{(2)}_{\mathrm{AC}}(x) = \left[\left(d^{(2)}_{\mathrm{BC}}(x)\right)^2 - a(x)\left[\left(d^{(2)}_{\mathrm{BC}}(x)\right)^2 - \frac{a(x)^2}{8}\right]^{1/2} + \frac{a(x)^2}{4}\right]^{1/2}. \tag{B.11}$$

The case $n = 3$ (see Fig. B.2 (d)) can be treated as $n = 1$ and substituting $d^{(1)}_{\mathrm{BC}}(x)$ with $d^{(3)}_{\mathrm{AC}}(x)$ and $d^{(1)}_{\mathrm{AC}}(x)$ with $d^{(3)}_{\mathrm{BC}}(x)$ in Eq. (B.9). Similarly, $d^{(4)}_{\mathrm{BC}}(x) = \frac{\sqrt{3}}{4}a(x)$ for $n = 4$ (see Fig. B.2 (e)) follows from the result for $n = 0$ and substituting $d^{(0)}_{\mathrm{AC}}(x)$ with $d^{(4)}_{\mathrm{BC}}(x)$.

Minimizing the distortion energy U

For $n = 0$ and $n = 4$ symmetry requires that the C atom stays at the VCA lattice site and $d_{\mathrm{AC}}^{(0)}(x) = d_{\mathrm{BC}}^{(4)}(x) = \frac{\sqrt{3}}{4}a(x) = d^{\mathrm{VCA}}(x)$. For $n = 1, 2$ and 3 the displacement of the C atom from the VCA site is determined by minimizing the corresponding distortion energy U. Balzarotti *et al.* take the VFF potential by Keating (Eq. (6.2)) but include only the bond stretching terms not the bond bending terms [122]. For an n-type tetrahedron U can be written as

$$\begin{aligned} U_n(x) = &\frac{3\alpha_{\mathrm{BC}}}{8\left(d_{\mathrm{BC}}^{\mathrm{bin}}\right)^2} n \left[\left(d_{\mathrm{BC}}^{(n)}(x)\right)^2 - \left(d_{\mathrm{BC}}^{\mathrm{bin}}\right)^2\right]^2 \\ &+ \frac{3\alpha_{\mathrm{AC}}}{8\left(d_{\mathrm{AC}}^{\mathrm{bin}}\right)^2}(4-n) \left[\left(d_{\mathrm{AC}}^{(n)}(x)\right)^2 - \left(d_{\mathrm{AC}}^{\mathrm{bin}}\right)^2\right]^2 \end{aligned} \tag{B.12}$$

where α_{AC} and α_{BC} denote the bond stretching force constants for A-C and B-C, respectively. Using the relations between $d_{\mathrm{AC}}^{(n)}(x)$ and $d_{\mathrm{BC}}^{(n)}(x)$ derived above, $U_n(x)$ becomes a function of $d_{\mathrm{BC}}^{(n)}(x)$ and minimization requires

$$0 = \frac{\mathrm{d}U_n(x)}{\mathrm{d}\left(d_{\mathrm{BC}}^{(n)}(x)\right)} = \frac{\partial U_n(x)}{\partial\left(d_{\mathrm{BC}}^{(n)}(x)\right)} + \frac{\partial U_n(x)}{\partial\left(d_{\mathrm{AC}}^{(n)}(x)\right)} \frac{\mathrm{d}\left(d_{\mathrm{AC}}^{(n)}(x)\right)}{\mathrm{d}\left(d_{\mathrm{BC}}^{(n)}(x)\right)} \tag{B.13}$$

with

$$\frac{\partial U_n(x)}{\partial\left(d_{\mathrm{BC}}^{(n)}(x)\right)} = \frac{3\alpha_{\mathrm{BC}}}{2\left(d_{\mathrm{BC}}^{\mathrm{bin}}\right)^2} n \left[\left(d_{\mathrm{BC}}^{(n)}(x)\right)^2 - \left(d_{\mathrm{BC}}^{\mathrm{bin}}\right)^2\right] d_{\mathrm{BC}}^{(n)}(x) \tag{B.14}$$

$$\frac{\partial U_n(x)}{\partial\left(d_{\mathrm{AC}}^{(n)}(x)\right)} = \frac{3\alpha_{\mathrm{AC}}}{2\left(d_{\mathrm{AC}}^{\mathrm{bin}}\right)^2}(4-n) \left[\left(d_{\mathrm{AC}}^{(n)}(x)\right)^2 - \left(d_{\mathrm{AC}}^{\mathrm{bin}}\right)^2\right] d_{\mathrm{AC}}^{(n)}(x). \tag{B.15}$$

For $n = 1$, Eq. (B.9) yields

$$\frac{\mathrm{d}\left(d_{\mathrm{AC}}^{(1)}(x)\right)}{\mathrm{d}\left(d_{\mathrm{BC}}^{(1)}(x)\right)} = \frac{1}{2d_{\mathrm{AC}}^{(1)}(x)} \left[2\left(d_{\mathrm{BC}}^{(1)}(x)\right) - \frac{2a(x)}{\sqrt{3}}\right]. \tag{B.16}$$

Inserting Eqs (B.14), (B.15) and (B.16) into Eq. (B.13) the following minimization criterion is obtained

$$0 = Aq^3 + Bq^2 + Cq + D \qquad \text{with} \qquad d_{\mathrm{BC}}^{(1)}(x) = q \tag{B.17}$$

and

$$\begin{aligned} A &= \frac{3}{2}\left[3\frac{\alpha_{\mathrm{AC}}}{\left(d_{\mathrm{AC}}^{\mathrm{bin}}\right)^2} + \frac{\alpha_{\mathrm{BC}}}{\left(d_{\mathrm{BC}}^{\mathrm{bin}}\right)^2}\right] \\ B &= -\frac{9\sqrt{3}}{2}\frac{\alpha_{\mathrm{AC}}}{\left(d_{\mathrm{AC}}^{\mathrm{bin}}\right)^2}a(x) \\ C &= \frac{21}{4}\frac{\alpha_{\mathrm{AC}}}{\left(d_{\mathrm{AC}}^{\mathrm{bin}}\right)^2}a(x)^2 - \frac{3}{2}\left[3\alpha_{\mathrm{AC}} + \alpha_{\mathrm{BC}}\right] \\ D &= \frac{3\sqrt{3}}{2}\left[-\frac{1}{2}\frac{\alpha_{\mathrm{AC}}}{\left(d_{\mathrm{AC}}^{\mathrm{bin}}\right)^2}a(x)^3 + \alpha_{\mathrm{AC}}a(x)\right]. \end{aligned} \tag{B.18}$$

For $n = 2$, Eq. (B.11) gives

$$\frac{\mathrm{d}\left(d_{\mathrm{AC}}^{(2)}(x)\right)}{\mathrm{d}\left(d_{\mathrm{BC}}^{(2)}(x)\right)} = \frac{d_{\mathrm{BC}}^{(2)}(x)}{d_{\mathrm{AC}}^{(2)}(x)}\left[1 - \frac{a(x)}{2}\left[\left(d_{\mathrm{BC}}^{(2)}(x)\right)^2 - \frac{a(x)^2}{8}\right]^{-1/2}\right]. \tag{B.19}$$

Inserting Eqs (B.14), (B.15) and (B.19) into Eq. (B.13) the minimization requirement follows to

$$0 = Aq^3 + Bq^2 + Cq + D \qquad \text{with} \qquad d_{\mathrm{BC}}^{(2)}(x) = \left[q^2 + \frac{a(x)^2}{8}\right]^{1/2} \tag{B.20}$$

and

$$\begin{aligned} A &= 3\left[\frac{\alpha_{\mathrm{AC}}}{\left(d_{\mathrm{AC}}^{\mathrm{bin}}\right)^2} + \frac{\alpha_{\mathrm{BC}}}{\left(d_{\mathrm{BC}}^{\mathrm{bin}}\right)^2}\right] \\ B &= -\frac{9}{2}\frac{\alpha_{\mathrm{AC}}}{\left(d_{\mathrm{AC}}^{\mathrm{bin}}\right)^2}a(x) \\ C &= \frac{3}{8}\left[7\frac{\alpha_{\mathrm{AC}}}{\left(d_{\mathrm{AC}}^{\mathrm{bin}}\right)^2} + \frac{\alpha_{\mathrm{BC}}}{\left(d_{\mathrm{BC}}^{\mathrm{bin}}\right)^2}\right]a(x)^2 - 3\left[\alpha_{\mathrm{AC}} + \alpha_{\mathrm{BC}}\right] \\ D &= -\frac{9}{16}\frac{\alpha_{\mathrm{AC}}}{\left(d_{\mathrm{AC}}^{\mathrm{bin}}\right)^2}a(x)^3 + \frac{3}{2}\alpha_{\mathrm{AC}}a(x). \end{aligned} \tag{B.21}$$

As mentioned above, the case $n = 3$ can be treated with the expressions derived for $n = 1$ by substituting "AC" properties with "BC" properties and vice versa. The coefficients A, B, C and D can be calculated at any given x from the lattice constant $a(x)$ and the bond stretching force constants α_{AC} and α_{BC}. Solving for the roots of the third order polynomials then yields q and thus $d_{\mathrm{AC}}^{(n)}(x)$ and $d_{\mathrm{BC}}^{(n)}(x)$ for every composition x.

Performing a weighted average over all $d_{\mathrm{AC}}^{(n)}(x)$ and $d_{\mathrm{BC}}^{(n)}(x)$

The probability $P_n(x)$ of finding an n-type tetrahedron at composition x is given by the binomial Bernoulli distribution

$$P_n(x) = \binom{4}{n} x^n (1-x)^{4-n}. \tag{B.22}$$

The mean A-C and B-C distances at any given x, $d_{\mathrm{AC}}(x)$ and $d_{\mathrm{BC}}(x)$, respectively, follow from the weighted average over all $d_{\mathrm{AC}}^{(n)}(x)$ and $d_{\mathrm{BC}}^{(n)}(x)$ values

$$\begin{aligned} d_{\mathrm{AC}}(x) &= \sum_{n=0}^{4} P_n(x)(4-n) d_{\mathrm{AC}}^{(n)}(x) \times \left[\sum_{n=0}^{4} P_n(x)(4-n) \right]^{-1} \\ d_{\mathrm{BC}}(x) &= \sum_{n=0}^{4} P_n(x) n d_{\mathrm{BC}}^{(n)}(x) \times \left[\sum_{n=0}^{4} P_n(x) n \right]^{-1}. \end{aligned} \tag{B.23}$$

Calculations for $\mathbf{Ga_{1-x}In_xP}$

The experimental values $d_{\mathrm{AC}}^{\mathrm{bin}} = d_{\mathrm{GaP}}^{\mathrm{bin}} = 2.342\,\text{Å}$ and $d_{\mathrm{BC}}^{\mathrm{bin}} = d_{\mathrm{InP}}^{\mathrm{bin}} = 2.531\,\text{Å}$ determined in this work correspond to binary lattice constants $a_{\mathrm{GaP}} = a(x = 0) = 5.409\,\text{Å}$ and $a_{\mathrm{InP}} = a(x = 1) = 5.845\,\text{Å}$, respectively. Table B.1 shows the lattice constant $a(x)$ calculated with Vegard's Law at different compositions x.

x	0.1	0.2	0.3	0.4	0.5	0.6	0.7	0.8	0.9
a (Å)	5.453	5.496	5.540	5.583	5.627	5.671	5.714	5.758	5.801

Table B.1: Lattice constant a as a function of x for $Ga_{1-x}In_xP$.

Following the procedure outlined above, the A-C and B-C distances were calculated for all types of tetrahedra as a function of x using the bond stretching force constants given by Martin, $\alpha_{AC} = \alpha_{GaP} = 47.32\ \mathrm{N\,m^{-1}}$ and $\alpha_{BC} = \alpha_{InP} = 43.04\ \mathrm{N\,m^{-1}}$ [113]. The $d^{(n)}_{GaP}(x)$ and $d^{(n)}_{InP}(x)$ values thus obtained are listed in Tables B.2 and B.3, respectively, together with the average distances $d_{GaP}(x)$ and $d_{InP}(x)$. The results are plotted in Figure B.4.

x	$d^{(0)}_{GaP} = d^{VCA}$ (Å)	$d^{(1)}_{GaP}$ (Å)	$d^{(2)}_{GaP}$ (Å)	$d^{(3)}_{GaP}$ (Å)	d_{GaP} (Å)
0.1	2.361	2.316	2.268	2.216	2.347
0.2	2.380	2.336	2.288	2.236	2.353
0.3	2.399	2.355	2.307	2.256	2.358
0.4	2.418	2.374	2.326	2.276	2.363
0.5	2.437	2.393	2.346	2.296	2.369
0.6	2.455	2.412	2.365	2.315	2.374
0.7	2.474	2.431	2.384	2.335	2.379
0.8	2.493	2.450	2.404	2.354	2.383
0.9	2.512	2.469	2.423	2.374	2.389

Table B.2: Ga-P distances $d^{(n)}_{GaP}$ for the different n-type tetrahedra in $Ga_{1-x}In_xP$ and average distance d_{GaP} as a function of x.

x	$d^{(1)}_{InP}$ (Å)	$d^{(2)}_{InP}$ (Å)	$d^{(3)}_{InP}$ (Å)	$d^{(4)}_{InP} = d^{VCA}$ (Å)	d_{InP} (Å)
0.1	2.508	2.462	2.413	2.361	2.494
0.2	2.525	2.480	2.432	2.380	2.498
0.3	2.543	2.498	2.450	2.399	2.502
0.4	2.560	2.517	2.469	2.418	2.506
0.5	2.578	2.534	2.487	2.437	2.510
0.6	2.596	2.553	2.506	2.455	2.514
0.7	2.614	2.572	2.524	2.474	2.518
0.8	2.633	2.590	2.543	2.493	2.523
0.9	2.651	2.608	2.561	2.512	2.527

Table B.3: In-P distances $d^{(n)}_{InP}$ for the different n-type tetrahedra in $Ga_{1-x}In_xP$ and average distance d_{InP} as a function of x.

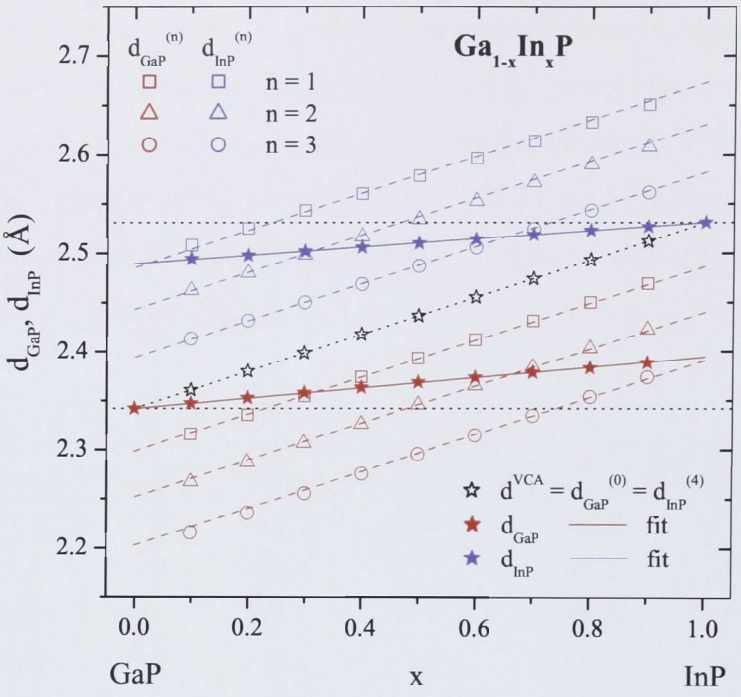

Figure B.4: Ga-P and In-P distances, $d_{\mathrm{GaP}}^{(n)}(x)$ and $d_{\mathrm{InP}}^{(n)}(x)$, respectively, for each of the n-type tetrahedra in $\mathrm{Ga}_{1-x}\mathrm{In}_x\mathrm{P}$ versus composition x. Also plotted are the average distances $d_{\mathrm{GaP}}(x)$ and $d_{\mathrm{InP}}(x)$. The dotted lines represent the VCA and P & H limit. The dashed lines have the same slope as the VCA curve and are a guide to the eye.

B.3 The two approximations A1 and A2

The impurity bond length $d_{\mathrm{BC}}^{\mathrm{AC:B}}$ is the limit of $d_{\mathrm{BC}}(x)$ as $x \to 0$. It follows from Eqs (B.22) and (B.23) that $d_{\mathrm{BC}}^{\mathrm{AC:B}} = d_{\mathrm{BC}}^{(1)}(x = 0)$. Similarly, $d_{\mathrm{AC}}^{\mathrm{BC:A}} = d_{\mathrm{AC}}^{(3)}(x = 1)$. Calculating the polynomial coefficients in Eq. (B.18) for $a(x = 0) = a_{\mathrm{GaP}} = 5.409\,\text{Å}$ and $a(x = 1) = a_{\mathrm{InP}} = 5.845\,\text{Å}$ and solving Eq. (B.17) yields $d_{\mathrm{InP}}^{\mathrm{GaP:In}} = 2.490\,\text{Å}$ and $d_{\mathrm{GaP}}^{\mathrm{InP:Ga}} = 2.393\,\text{Å}$. The corresponding ϵ values are $\epsilon = 0.78$ for GaP:In and $\epsilon = 0.73$ for InP:Ga. The same values are obtained from a linear fit to all $d_{\mathrm{GaP}}(x)$ and $d_{\mathrm{InP}}(x)$ as plotted in Fig. B.4.

The model by Balzarotti *et al.* includes only bond stretching terms in the VFF potential and keeps the second NNs fixed. As discussed in Section 6.1 it therefore resembles Martins & Zunger II except that the two approximations A1 and A2 are not applied. However, the effect of these approximations on

the calculated ϵ is certainly not negligible as the GaP:In and InP:Ga values are effectively "swapped" for the two models. To better evaluate the influence of these approximations, the dilute limit calculations performed above using the model by Balzarotti *et al.* are repeated with applying either A1 or A2 or both.

Harmonic approximation (A1)

The VFF potential by Keating given in Eq. (6.2) contains the bond length difference $u_i' = d_i - d_i^{\text{bin}}$ up to fourth order as can be seen from

$$\begin{aligned}\left[\mathbf{d}_i \cdot \mathbf{d}_i - \mathbf{d}_i^{\text{bin}} \cdot \mathbf{d}_i^{\text{bin}}\right]^2 &= \left[(d_i)^2 - \left(d_i^{\text{bin}}\right)^2\right]^2 \\ &= \left[\left(d_i^{\text{bin}} + u_i'\right)^2 - \left(d_i^{\text{bin}}\right)^2\right]^2 \\ &= \left[2d_i^{\text{bin}} u_i' + (u_i')^2\right]^2 \\ &= 4\left(d_i^{\text{bin}}\right)^2 (u_i')^2 + 4d_i^{\text{bin}} (u_i')^3 + (u_i')^4 .\end{aligned} \tag{B.24}$$

In the harmonic approximation (A1) only the second order term $4\left(d_i^{\text{bin}}\right)^2 (u_i')^2$ is taken. For $n = 1$ the distortion energy $U_n(x)$ in Eq. (B.12) thus becomes

$$U_1(x) = \frac{3}{2}\alpha_{\text{BC}}\left[d_{\text{BC}}^{(1)}(x) - d_{\text{BC}}^{\text{bin}}\right]^2 + \frac{9}{2}\alpha_{\text{AC}}\left[d_{\text{AC}}^{(1)}(x) - d_{\text{AC}}^{\text{bin}}\right]^2 . \tag{B.25}$$

The minimization requirement (B.13) can then be written as

$$0 = 3\alpha_{\text{BC}}\left[d_{\text{BC}}^{(1)}(x) - d_{\text{BC}}^{\text{bin}}\right] + 9\alpha_{\text{AC}}\left[d_{\text{AC}}^{(1)}(x) - d_{\text{AC}}^{\text{bin}}\right]\frac{\mathrm{d}\left(d_{\text{AC}}^{(1)}(x)\right)}{\mathrm{d}\left(d_{\text{BC}}^{(1)}(x)\right)}. \tag{B.26}$$

Inserting Eq. (B.16) as before and solving for $d_{\text{BC}}^{(1)}$ with $a(x = 0) = a_{\text{GaP}} = 5.409\,\text{Å}$ results in $d_{\text{InP}}^{\text{GaP:In}} = 2.490\,\text{Å}$ and $\epsilon = 0.78$. For InP:Ga, $d_{\text{GaP}}^{\text{InP:Ga}} = 2.393\,\text{Å}$ and $\epsilon = 0.73$ are obtained in a similar manner. These values are the same as those determined above without using the harmonic approximation. Applying A1 therefore has no influence on the calculated impurity bond length or the relaxation parameter.

Geometric approximation (A2)

As mentioned in the Section B.1, the relation between $d_{\mathrm{AC}}^{(1)}(x)$ and $d_{\mathrm{BC}}^{(1)}(x)$ can be approximated by

$$\begin{aligned} d_{\mathrm{AC}}^{(1)}(x) = d_{\mathrm{AC}}^{\mathrm{bin}} - \frac{1}{3}u &= d_{\mathrm{AC}}^{\mathrm{bin}} - \frac{1}{3}\left[d_{\mathrm{BC}}^{(1)}(x) - d_{\mathrm{AC}}^{\mathrm{bin}}\right] \\ &= \frac{4}{3}d_{\mathrm{AC}}^{\mathrm{bin}} - \frac{1}{3}d_{\mathrm{BC}}^{(1)}(x). \end{aligned} \tag{B.27}$$

With this Eq. (B.16) becomes

$$\frac{\mathrm{d}\left(d_{\mathrm{AC}}^{(1)}(x)\right)}{\mathrm{d}\left(d_{\mathrm{BC}}^{(1)}(x)\right)} = -\frac{1}{3} \tag{B.28}$$

and solving Eq. (B.13) yields $d_{\mathrm{InP}}^{\mathrm{GaP:In}} = 2.480\,\text{Å}$ and $d_{\mathrm{GaP}}^{\mathrm{InP:Ga}} = 2.386\,\text{Å}$. The corresponding ϵ values are $\epsilon = 0.73$ for GaP:In and $\epsilon = 0.77$ for InP:Ga. Applying the geometric approximation therefore influences the calculated ϵ values and accounts for the different results of Martins & Zunger II and Balzarotti *et al.* observed in Table 6.1.

Harmonic and geometric approximations (A1 & A2)

Applying both approximations is realized by inserting Eq. (B.28) into (B.26) and solving for $d_{\mathrm{BC}}^{(1)}(x)$. The result is

$$d_{\mathrm{BC}}^{\mathrm{AC:B}} = d_{\mathrm{BC}}^{(1)}(x \to 0) = \frac{3\alpha_{\mathrm{BC}} d_{\mathrm{BC}}^{\mathrm{bin}} + \alpha_{\mathrm{AC}} d_{\mathrm{AC}}^{\mathrm{bin}}}{3\alpha_{\mathrm{BC}} + \alpha_{\mathrm{AC}}} \tag{B.29}$$

and

$$\epsilon = \frac{d_{\mathrm{BC}}^{\mathrm{AC:B}} - d_{\mathrm{AC}}^{\mathrm{bin}}}{d_{\mathrm{BC}}^{\mathrm{bin}} - d_{\mathrm{AC}}^{\mathrm{bin}}} = \left[1 + \frac{1}{3}\frac{\alpha_{\mathrm{AC}}}{\alpha_{\mathrm{BC}}}\right]^{-1} \tag{B.30}$$

which is exactly the expression derived for Martins & Zunger II. For $\mathrm{Ga}_{1-x}\mathrm{In}_x\mathrm{P}$ the values amount to $d_{\mathrm{InP}}^{\mathrm{GaP:In}} = 2.480\,\text{Å}$ and $d_{\mathrm{GaP}}^{\mathrm{InP:Ga}} = 2.386\,\text{Å}$ with $\epsilon = 0.73$ and $\epsilon = 0.77$ for GaP:In and InP:Ga, respectively. Comparing these results with those obtained by applying only the geometric approximation shows again that the harmonic approximation does not influence the calculated ϵ values.